Dissertation

submitted to the

Combined Faculty of Natural Sciences and Mathematics

of Heidelberg University, Germany

for the degree of

Doctor of Natural Sciences

Put forward by

Grigorios L. Katsoulakos

born in: Athens, Greece

Oral examination: 04.11.2019

Nonthermal Processes Near Supermassive Black Holes

Referees:	PD Dr. Frank Rieger Prof. Dr. Matthias Bartelmann

dedicated to my wife Efthymia
and to my Son Loukas

Zusammenfassung

In den letzten Jahren hat die Gammastrahlenastronomie einen erstaunlichen Fortschritt bei der Erforschung des extragalaktischen Gammastrahlenhimmels gemacht. Dies gilt insbesondere für aktive Galaxien, bei denen der Jet einen signifikanten Winkel mit der Sichtlinie bildet, und in denen eine bemerkenswerte, variable Gammastrahlenaktivität beobachtet wurde. Die beobachtete schnelle Variabilität der Gammastrahlung, auf einer Zeitskala die mit der Lichtlaufzeit über den Horizont des Schwarzen Lochs vergleichbar ist, legt es nahe, Emissionsprozesse zu testen, die in der Nähe des zentralen supermassiven Schwarzen Lochs ablaufen. In dieser Doktorarbeit untersuchen wir das sogenannte magnetosphärische Szenario. Diesem zufolge können geladene Teilchen in besonderen Bereichen der Magnetosphäre durch (parallele) elektrische Felder beschleunigt werden. Solche elektrische Felder können entweder in der Nähe der sog. *Null*-Oberfläche, an der die Ladungsdichte ihr Vorzeichen wechselt, oder in der Nähe der sog. *Stagnation*-Fläche, die einfallende und ausströmende Materie trennt, auftreten. Die Beschleunigung der Leptonen geht dabei mit einer Erzeugung von Gammastrahlen über die inverse *Compton* Streuung weicher Photonen der Akkretionsscheibe und mittels Krümmungsstrahlung einher. Wir entwickeln und untersuchen in diesem Zusammenhang ein eindimensionales Modell für die Beschleunigung und Emission magnetosphärischer Teilchen und bestimmen die terminalen *Lorentz* -Faktoren der beschleunigten Ladungen und die maximal extrahierbare Leistung aus den Beschleunigungszonen. Ein Vergleich mit Beobachtungen der hochenergetischen Gammastrahlung in der Radiogalaxie M87 zeigt, dass diese durch magnetosphärische Prozesse erzeugt sein könnten.

Summary

In recent years, γ-ray astronomy has made considerable progress in the exploration of the extragalactic γ-ray sky. In particular, active galaxies, whose relativistic jets/outflows are significantly inclined with respect to the *line-of-sight*, have revealed remarkable flaring activity at γ-ray energies. The observed rapid variability of the γ-ray emission, comparable to timescales of the light travel time across the black hole horizon, provides a strong motivation for testing radiative scenarios associated with the vicinity of the central supermassive black hole. In this doctoral study, we explore the so-called black hole magnetospheric scenario. Accordingly, strong particle acceleration may occur within the black hole magnetosphere in regions of unscreened electric fields (gaps). This can happen either at the *null* surface across which the charge density changes sign or at the *stagnation* surface which separates the inwardly from the outwardly moving matter. The acceleration of leptons is accompanied by γ-ray emission via inverse *Compton* scattering of the ambient (disk) soft photons as well as *curvature* radiation. This thesis explores the potential of these processes to account for the observed γ-ray features. By developing and studying an one-dimensional, steady model for magnetospheric particle acceleration and emission, as well as, estimating the terminal *Lorentz* factors of the accelerated charges and the maximum extractable gap power, we find that magnetospheric processes can be responsible for the observed, rapidly variable very-high-energy γ-ray emission in the radio galaxy M87.

Acknowledgements

The author would like to express his deep gratitude to PD Dr. *Frank Rieger* for the scientific guidance, the educational discussions on magnetospheric processes, the useful critiques and, generally, for the supervision of the doctoral research. In addition, the author also would like to thank *Frank Rieger* for the sincere understanding of his student on issues even outside astronomy.

The author also wishes to thank Prof. *Matthias Bartelmann* for his willingness to serve as thesis referee, and all members of the exam committee for their general willingness. In particular, the author wishes to thank PD Dr. *Christian Fendt* for the discussions concerning R-MHD and numerical simulations. The author is grateful to Prof. *Felix Aharonian*, Prof. *John Kirk* and Prof. *Amir Levinson* for discussion, support and encouragement.

Finally, the author acknowledges the International Max Planck Research School in Heidelberg (IMPRS-HD) for the financial support, as well as, the Max-Planck-Institute für Kernphysik (MPIK) and the Institute of Theoretical Astrophysics (ITA) for hospitality.

Contents

Chapter 1

Very-high energy observations of non-*blazar* AGN

The exploration of the sky at γ-ray energies has opened up a new and fascinating window to the universe. Despite their extreme nature, namely the production of unusually high energy radiation, the observed non-thermal phenomena seem to be the result of more than one physical process which take place in many different astrophysical environments of galactic (e.g., *supernova* remnants [SNRs], *microquasars*, *pulsars*, *pulsar* wind nebulae [PWNe], diffuse galactic regions) as well as extragalactic origin (e.g., active galactic nuclei [AGN], γ-ray bursts [GRBs]).

Observations in the γ-ray band involve the detection of extraterrestrial radiation, the energy of which ranges from $\sim$ 0.5 MeV to (and possibly beyond) $\sim$ 100 TeV. For classification purposes, the observed γ-ray emission is further divided into the *high* and *very-high* energy class (hereafter HE: $\sim$ 50 MeV - 50 GeV and VHE: $\gtrsim$ 50 GeV), depending on whether the γ-ray event is recorded at energies below or above $\sim$ 50 GeV, respectively. As we will discuss later on, given that the γ-ray domain covers more than six orders of magnitude in energy, different observational techniques are employed for the detection of the HE and VHE γ-ray emission.

Typically, we characterize the spectrum of the γ-ray photons by the flux of energy, F_ν, per unit area per unit time per unit frequency ν (i.e., in units of $erg\ cm^{-2}\ sec^{-1}\ Hz^{-1}$). Alternatively, a (useful) visualization of the observed γ-ray emission can be done by means of the *spectral energy distribution* (SED) chart (i.e., the quantity νF_ν $[erg\ cm^{-2}\ s^{-1}]$ as a function of the frequency ν). The non-thermal emission often exhibits smooth spectral shapes (e.g., power-laws) which contain critical physical information. In rough lines, γ-rays are emitted by strongly accelerated charged particles which are produced in the astrophysical sources. The range and distribution of the γ-ray photons reflect the radiative processes and the energy distribution of the primary particle population.

In this chapter, we report on HE and VHE observations as obtained from modern γ-ray telescopes/facilities operating during the last ~ 15 years. More specifically, we give a brief introduction to the observational methods and current instruments (e.g., *Fermi-LAT*, *HESS*, *MAGIC*, *VERITAS*, *HAWC*). Subsequently, we review some significant discoveries in the field of extragalactic γ-ray astronomy. We mainly focus on results concerning the VHE detections from misaligned (i.e., non-*blazar*) AGN. The VHE flaring activity observed in the radio galaxies M87, IC310 and others constitutes a starting point of this doctoral study. The rapid variability of the γ-ray emission from those galaxies as well as the substantial inclination of their relativistic jet/outflow with respect to the *line-of-sight* give a strong motivation for studying radiative scenarios which are related to the nearby vicinity of the central supermassive black hole (BH) (i.e., the BH magnetosphere).

1.1 Techniques for γ-ray detections

Given that high energy photons are subjected to strong absorption due to the interaction with the molecules in the upper atmosphere, only two alternatives (of extremely high cost) remain for detecting γ-ray emission. In particular, we can observe γ-rays either directly by means of space detectors orbiting the *Earth* beyond the atmospheric layer or indirectly, by establishing extended infrastructures on the ground where massive detectors are able to record the electromagnetic cascade triggered by the passage of a primary γ-ray photon through the atmosphere. In fact, both methods operate in a complementary mode due to the extensive spectral range and the strong flux decrease of γ-rays at high energies. Accordingly, detectors based on the space technology are suitable for counting γ-rays up to energies about a hundred GeV where the induced cascades in the atmosphere are not strong enough to reach the ground but an (effective) detecting area of $\sim 1\ m^2$ placed in a spacecraft is sufficient to provide the desirable sensitivity. For γ-ray energies more than ~ 100 GeV, on the other hand, the common steep depression in the γ-ray flux requires detecting area of more than $\sim 10^4\ m^2$ making the use of the ground-based technique inevitable.

In the case of space-based instruments, HE γ-ray photons are directly recorded during their encounter with the detector leading to pair production by intersection with some active material. Under real observational conditions, two sub-detectors are needed (i.e., a *tracker* and a *calorimeter*) in order to accurately determine the direction of the incoming photon and its

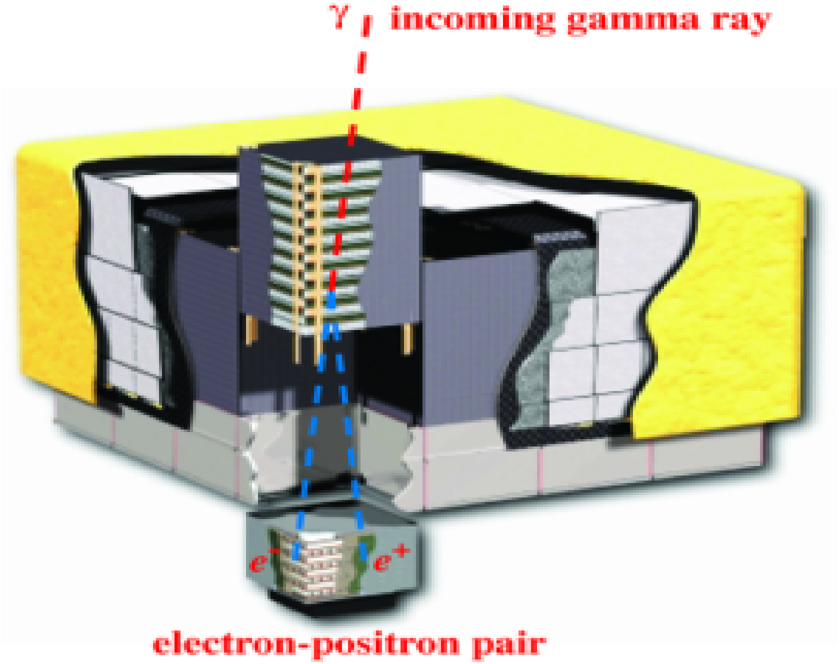

Figure 1.1: Schematic illustration of the detection process in a space-type γ-ray telescope.

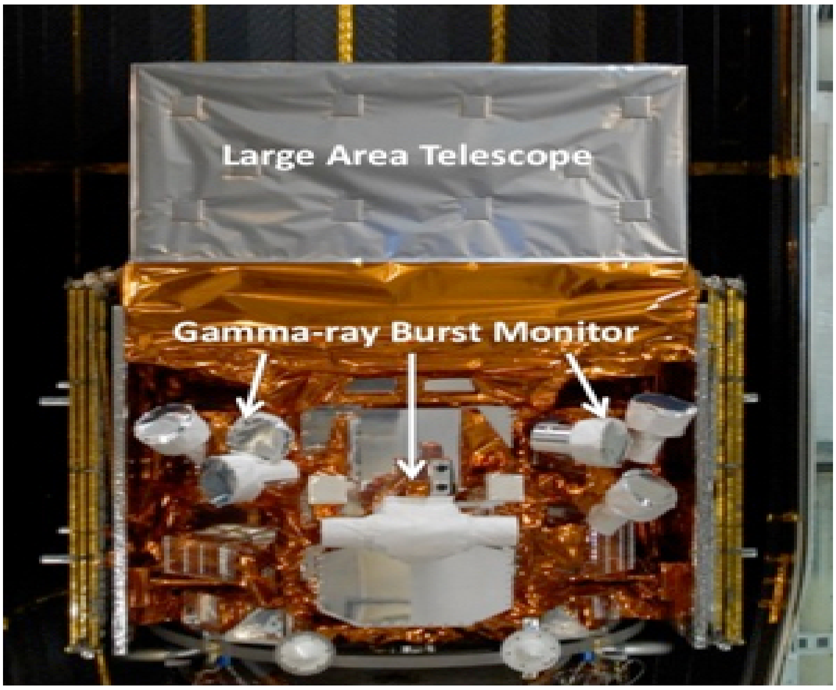

Figure 1.2: The Fermi γ-ray space telescope. The detector mainly consists of two scientific devices: The Large Area Telescope (LAT) and the γ-ray Burst Monitor (GMB).

energy. In figure (1.1) above, a schematic representation of the detection process in a space-based γ-ray telescopes is shown[1]. A very energetic photon entering the detector produces pairs that are tracked through the instrument by some active material (see the consecutive layers in figure 1.1), while the resulting particles are channelled then to the *calorimeter* for the measurement of the energy.

The *Fermi* γ-ray space telescope launched in June 2008 (i.e., a satellite observatory) and currently being in operation corresponds to the aforementioned type of instruments. More specifically, the *Fermi* telescope carries two scientific devices (see figure 1.2), that is the *Large Area Telescope* (LAT) and the *γ-ray Burst Monitor* (GMB), which measure photon counts with energies from 8 keV to over 300 GeV. The angular resolution of the LAT detector is approximately $\sim 0.1^o$. The satellite orbits the *Earth* every 96 minutes allowing a scan of the entire γ-ray sky every two orbits.

On the other hand, the basic concept of the ground-based detectors uses the processing of the pair cascade products in order to extract the relevant information (i.e., the direction and the energy) of the primary γ-ray photons. VHE γ-ray photons directed towards *Earth* interact with the molecules of the upper atmosphere producing electron-positron pairs, which in turn radiate secondary γ-rays mostly through *Bremsstrahlung* emission. The resulting lower energy γ-ray photons again produce leptons an so on. In such a way, a photon-pair cascade initiates and evolves through the atmosphere. Provided that the primary cosmic photons have high energies, the secondary charged particles will move through the atmosphere faster than light. Under these circumstances, the relativistic particles produce *Cherenkov* emission. We note that this *Cherenkov* light is primarily emitted into the *ultraviolet* spectrum in a small cone around the direction of particle's motion. Evidently, γ-ray observations with ground-based instruments are possible either by collecting the *Cherenkov* photons with sensitive *ultraviolet* telescopes called *Imaging Air Cherenkov Telescopes* (IACTs) or by deploying particle counters on the ground and recording the *Cherenkov* light of the *Extensive Air Shower* (EAS) produced in water *Cherenkov* detectors. In figures (1.3) and (1.4) below, we illustrate schematically the IACT and water tank techniques, respectively.

The *High Energy Stereoscopic System* (H.E.S.S.) consisting of 5 IACTS and located in *Namibia* (see figure 1.5), the *Major Atmospheric Gamma Imaging Cherenkov* (MAGIC) composed of 2 IACTS and placed in *Canary* islands (see figure 1.6) and the *Very Energetic Radiation Imaging Telescope*

---

[1] The figures shown in this section have been taken from the public web pages of the corresponding γ-ray telescopes and observatories: https://fermi.gsfc.nasa.gov/, https://www.mpi-hd.mpg.de/hfm/HESS/, http://www.ifae.es/eng/experiments/magic.html, https://veritas.sao.arizona.edu/, https://www.hawc-observatory.org/

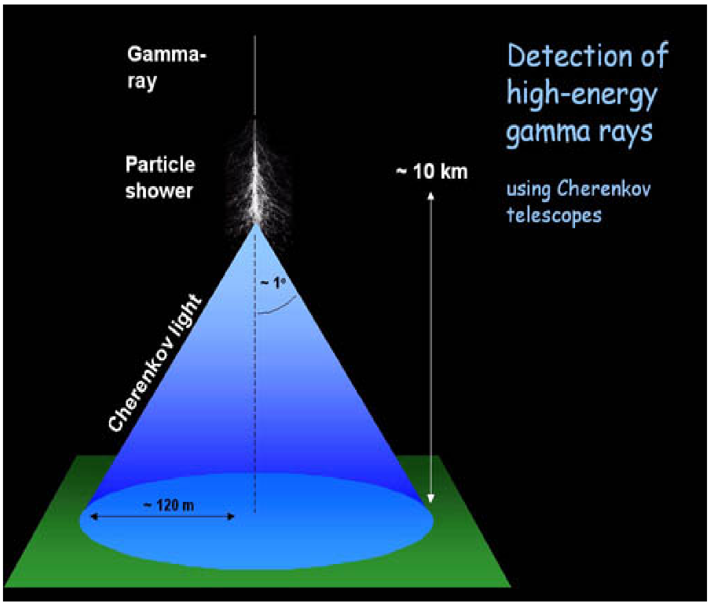

Figure 1.3: Schematic representation of the Imaging Air Cherenkov Technique (IACT) for ground-based observations in the VHE γ-ray domain using an array of UV-sensitive photomultipliers.

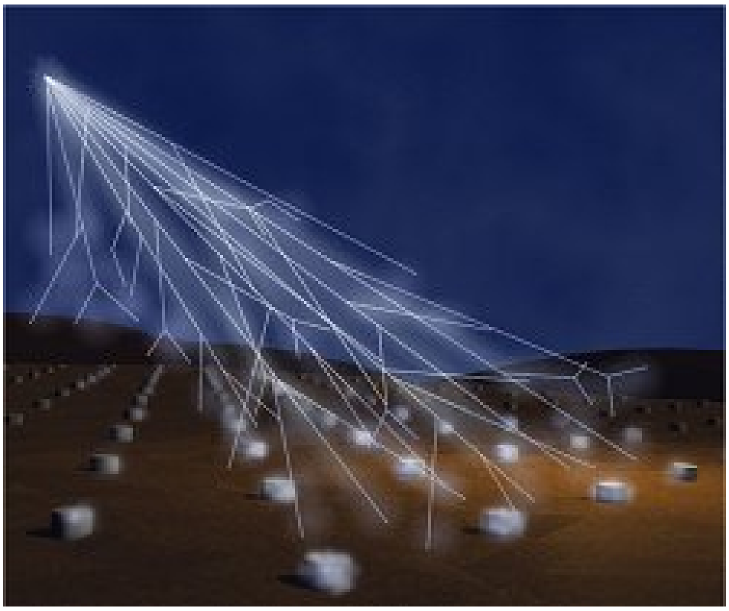

Figure 1.4: Artistic illustration of the observation of Extensive Air Shower (EAS) using particle detectors (e.g., water tanks) on the ground.

Figure 1.5: The High Energy Stereoscopic System (H.E.S.S.) in Namibia at altitude of 1800 meters.

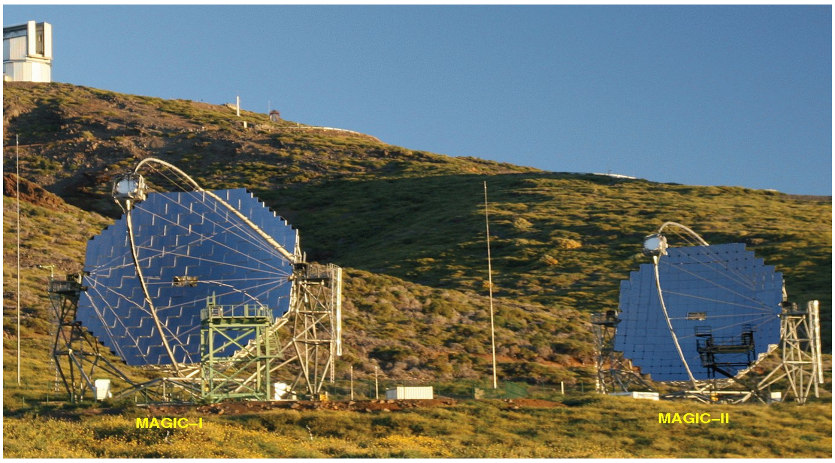

Figure 1.6: The Major Atmospheric Gamma Imaging Cherenkov (MAGIC) telescope in Canary islands at altitude of 2200 meters.

Figure 1.7: The Very Energetic Radiation Imaging Telescope Array System (VERITAS) in Arizona at altitude of 1300 meters.

Figure 1.8: The High Altitude Water Cherenkov (HAWC) γ-ray observatory located in Mexico at 4100 meters.

Array System (VERITAS) in *Arizona* equipped with 4 IACTS (see figure 1.7) demonstrate the current generation of instruments which exploit the air *Cherenkov* technique. These three VHE observatories detect γ-ray radiation in the energy range from $\sim$ 50 GeV up to $\sim$ 50 TeV with an angular resolution slightly below $\sim 0.1^o$. In addition, the *Cherenkov Telescope Array* (CTA) will be the future instrument of ground-based γ-ray astronomy[2]. CTA, an infrastructure with more than 100 telescopes located in the northern and southern hemispheres, will be the world's largest and most sensitive observatory which is going to observe VHE radiation up to $\sim 10^3$ TeV. The *High Altitude Water Cherenkov* (HAWC) observatory (see figure 1.8), on the other hand, is currently taking data using water *Cherenkov* detectors. The HAWC VHE observatory located in *Mexico* at the altitude of 4100 m measures γ-ray photons with energies from $\sim$ 400 GeV up to $\sim$ 100 TeV. As it seen from figure (1.8), a large net with 300 water-*Cherenkov* tanks provide an effective detection area of $\sim 22000\ m^2$.

For more details on instrumentation and techniques the interested reader is referred to the recent reviews by Angelis and Mallamaci (2018); Sciascio (2019).

---

[2] CTA is currently under construction. Its science operation is estimated to start around 2022; https://www.cta-observatory.org/

1.2 The extragalactic γ-ray sky

The light observed from a typical galaxy is mainly emitted by the hosted stars, and secondarily from the available gas and dust contained in it. The dominant spectral component of a normal galaxy thus results from the superposition of billions of stellar spectra. Given that the plasma which composes the stellar atmospheres is considered to be in thermodynamic equilibrium, we can plausibly assume that the produced stellar radiation is of thermal nature. Consequently, the entire spectrum of the galaxy will be thermal too and typically will range from a wavelength of $\lambda_i \sim 4000$ Å up to $\lambda_f \sim 20000$ Å (Sparke and Gallagher, 2007).

There are, nevertheless, some galaxies (i.e., approximately 10% of the total number) whose brightness can be 1000 times greater than the one of a normal galaxy. These peculiar extragalactic sources display a broader spectral energy distribution ranging from *radio* wavelengths up to the γ-ray band. The non-thermal radiation is believed to emanate from a small central region (comparable to the solar system) referred to as *active galactic nucleus* (AGN), while the galaxy hosting this region is usually called *active galaxy.* The physical interpretation of the AGN-phenomenon involves the violent energy extraction from the system, at first, via radiation due to gas falling onto a central supermassive black hole and, secondly, through the emergence of twin collimated relativistic jets from the nucleus. A schematic illustration of an AGN, for example, is shown in figure (3.1) in the third chapter. From the observational point of view AGN have been classified into several types (e.g., BL Lac objects, FSRQs, Quasars, radio galaxies, *Seyfert* I, *Seyfert* II galaxies and subclasses) depending on their brightness and spectral properties (e.g., the presence or absence of emission lines). In unification schemes, however, the different AGN classes are associated with different viewing angles onto the central engine (Urry and Padovani, 1995).

Over the last ten years, the HE instrument *Fermi*-LAT has revealed a considerably active γ-ray sky by detecting more than 5000 sources in the γ-ray domain[3]. Out of this number, more than half are extragalactic and especially are associated with active galaxies. In particular, in the *Fermi*-LAT fourth catalogue (4FGL), which includes γ-ray objects between 50 MeV and 1 TeV, about 3130 AGN are reported. The overwhelming majority of the 4FGL sources consists of *blazars* (i.e., 686 *Flat Spectrum Radio Quasars* [FSRQs], 1116 BL Lacs and 1330 *Blazars* of uncertain type), while only 77 sources have been classified as non-*blazar* AGN (e.g., radio galaxies). In the

---

[3] For detailed presentation of the detected sources we refer to the link:
https://fermi.gsfc.nasa.gov/ssc/data/access/lat/8yr_catalog/4FGL_Catalo$g$_v11.pdf

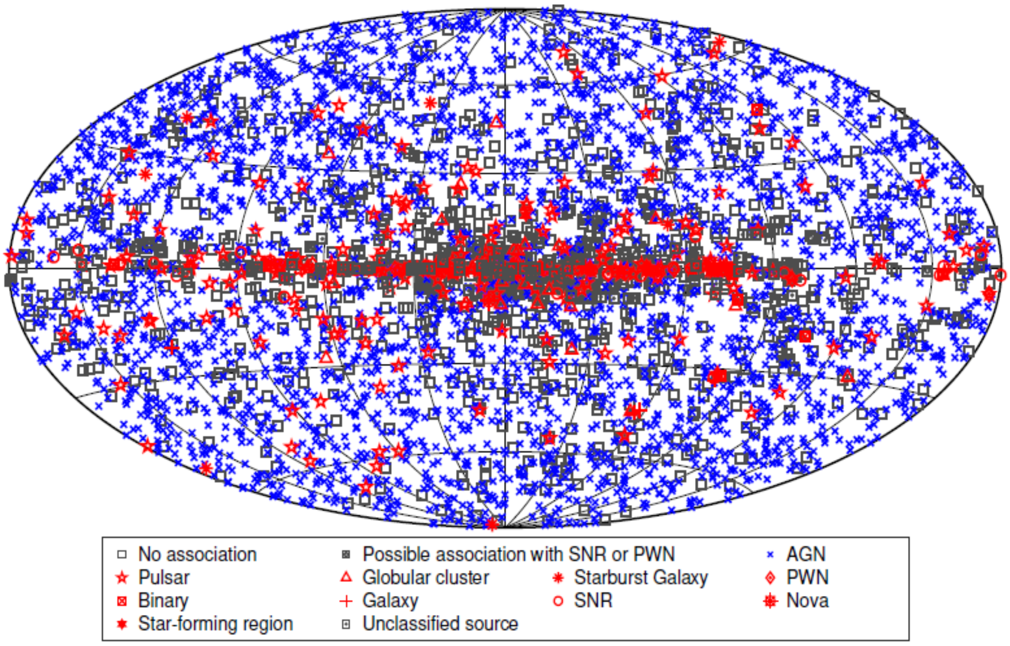

Figure 1.9: The HE γ-ray sky shown in galactic coordinates. Evidently, the vast majority of the detected objects are associated with AGN (blue x mark). The figure was taken from: https://fermi.gsfc.nasa.gov/ssc/data/access/lat/8yr_catalog/4FGL_Catalog_v11.pdf

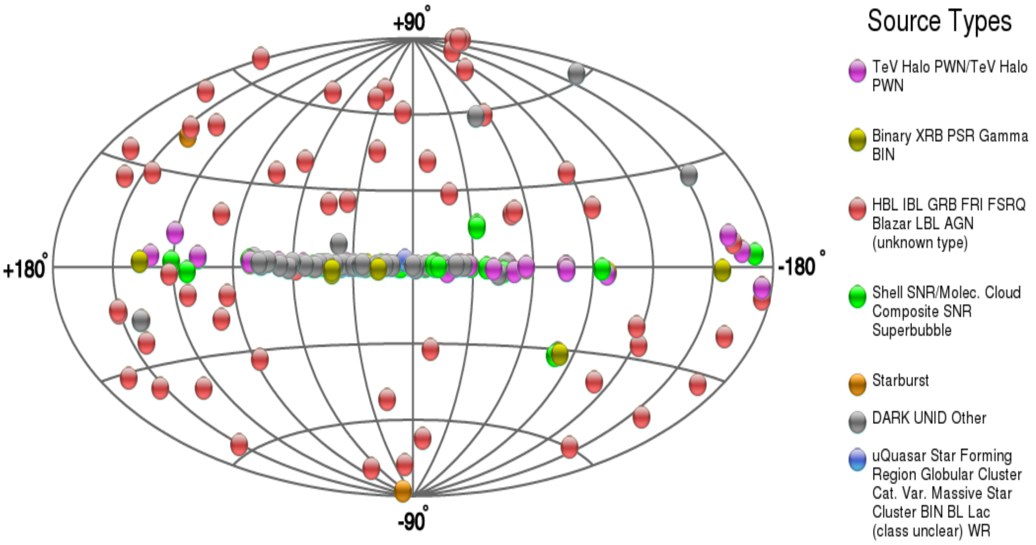

Figure 1.10: The VHE γ-ray sky illustrated in galactic coordinates. Obviously, the majority of the observed sources are related to some type of AGN (red circles). The figure was provided by: http://tevcat.uchicago.edu

VHE regime, on the other hand, about 70 AGN are currently reported in the *TeVcat*[4] catalogue and six of them (i.e., the radio galaxies M87, IC310, Cen A, 3C 264, NGC 1275 and PKS0625-35) belong simultaneously to the 4FGL detected group of non-*blazar* AGN. In particular, the radio galaxies M87 and IC310 are of great interest due to their highly variable TeV flaring activity that has been so far observed. In figures (1.9) and (1.10) above, the HE and the VHE γ-ray sky maps are shown in galactic coordinates.

A *blazar*-type active galaxy (e.g., a FSRQ or BL Lac) is a radio loud galaxy in which the relativistic jet is considered to be inclined at small viewing angles θ_{los} to the *line of sight*. The relativistic motion of the jet bulk as well as the small angles θ_{los} trigger the *Doppler-boosting* of the intrinsic jet emission, that is $S(\nu) = \delta^{\alpha} S'(\nu')$, where $\delta = 1/[\Gamma_j(1 - \beta_j \cos\theta_{los})]$ is the *Doppler* factor, $\Gamma_j = 1/\sqrt{1-\beta_j^2}$ is the jet bulk *Lorentz* factor and $\alpha \geq 2$. The *Doppler-boosting* effect biases HE and VHE γ-ray catalogues, since it favours the detection of *blazar*-type objects and disfavours that of *misaligned AGN* (MAGN) (e.g., radio galaxies). This is one reason why non-*blazar* AGN are under-represented in such γ-ray catalogues. Nevertheless, MAGN currently represent an interesting class of objects, because they offer unique insights (due to the mild *Doppler-boosting* of their intrinsic radiation) into the physics of accreting supermassive black hole systems and sub-pc AGN jets.

1.3 VHE activity from misaligned AGN

In the following, we highlight some HE and VHE observational results of prominent misaligned AGN. The operation of instruments surveying at γ-ray energies has revealed that radio galaxies can be significant VHE emitters. In some cases, they show VHE flaring activity on considerable short variability time-scale. The significant inclination (i.e., $\theta_{los} > 10^o - 15^o$) of the *line of sight* with the axis of the radio jet makes it possible to investigate if the VHE behaviour originates from deeper regions, namely close to the central engine of the AGN (e.g., the black hole magnetosphere).

1.3.1 The radio galaxy M87

The first extragalactic source (see figure 1.11) observed in VHE γ-rays has been the *Virgo Cluster* radio galaxy M87 (Aharonian et al., 2003). M87 is located at a distance of $\sim$ 16.4 Mpc (Bird et al., 2010) and has been classified

---

[4] For a summary of the observed VHE sources we refer to: http://tevcat.uchicago.edu

as a low-excitation, weak-power source of type FR I. The center of M87 hosts one of the most massive black holes with mass $M = (6.5 \pm 0.7) \times 10^9 M_\odot$ (Akiyama et al., 2019a). In figure (1.12) below, the shadow of the black hole (M87*) observed for first time at radio wavelength of 1.2 mm (230 Hz) is depicted. The compact radio source appears as an asymmetric bright ring with a diameter of (42 ± 3) μas, which surrounds a central decay in brightness (i.e., the shadow of the black hole). The disk material is thought to be accreted in a radiatively inefficient (RIAF) mode (Reynolds et al., 1996; Akiyama et al., 2019b). Given its proximity galaxy M87 has become a prominent target to probe scenarios of jet formation with high-resolution radio observations down to scales of the gravitational radius (e.g., Doeleman et al., 2012; Kino et al., 2015; Akiyama et al., 2015; Hada et al., 2016; Mertens et al., 2016; Akiyama et al., 2019b). The sub-parsec scale of M87 radio jet appears to be inclined with respect to the *line of sight* by an angle $\theta_{los} \sim 15^o$–25^o. Accordingly, we expect modest *Doppler* factors and thus no strong enhancement of the intrinsic jet emission. On this scale-length the jet has a complex structure seemingly compatible with an outer, slower, mildly relati-

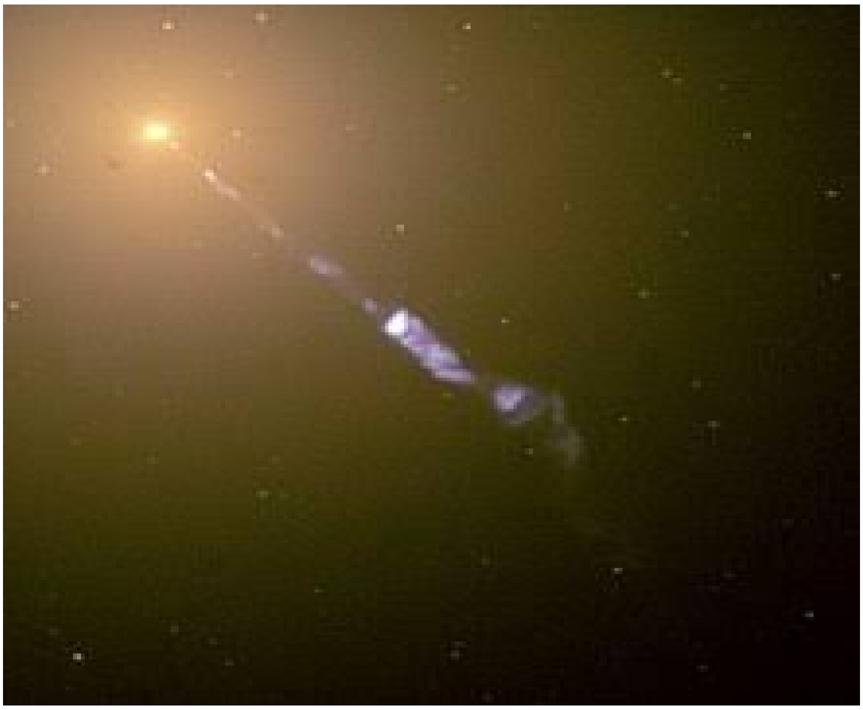

Figure 1.11: The radio galaxy M87 in the Virgo Cluster in the optical spectrum. The picture shows a strongly collimated kpc-scale jet structure emerging from the nucleus of the galaxy. The picture was taken by the Hubble Space Telescope (HST).

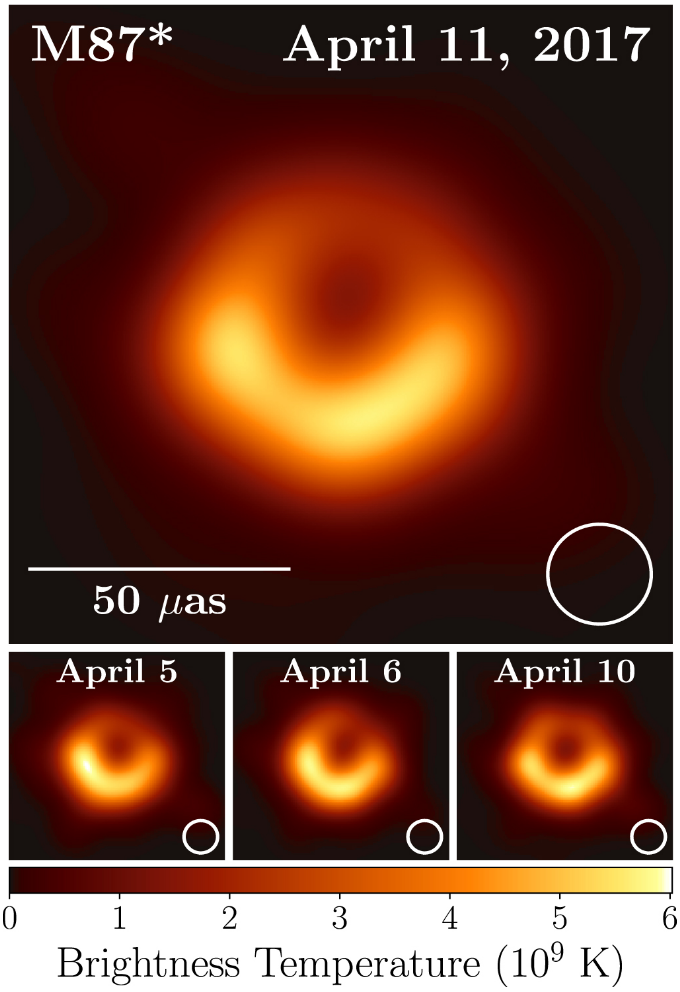

Figure 1.12: The shadow/ring radio structure of the central black hole in the galaxy M87 (M87*) imaged at radio wavelength of 1.2 mm (230 Hz). The observations were conducted by the Event Horizon Telescope (EHT) (Akiyama et al., 2019a).

vistic layer ($\beta_{app} \sim 0.5c$) and an inner, faster moving ($\Gamma_{bulk} \sim 2.5$) (see Mertens et al., 2016, for details).

In the VHE domain, observations of M87 show three[5] VHE γ-ray flaring events during which rapid day-scale variability (i.e., $\Delta\tau_{obs} \approx 1$ day) has been detected (Aharonian et al., 2006; Albert et al., 2008; Acciari et al., 2009). In figure (1.13) below, light curves of the VHE episodes as recorded from ground-based instruments (i.e., H.E.S.S., MAGIC and VERITAS) are shown (Abramowski et al., 2012). During these active states the VHE spectrum of

---

[5] A fourth elevated VHE state was also detected (i.e., flux levels 2-3 times higher than average) in 2012 with flux variability on time scale of weeks (Beilicke and Collaboration, 2012).

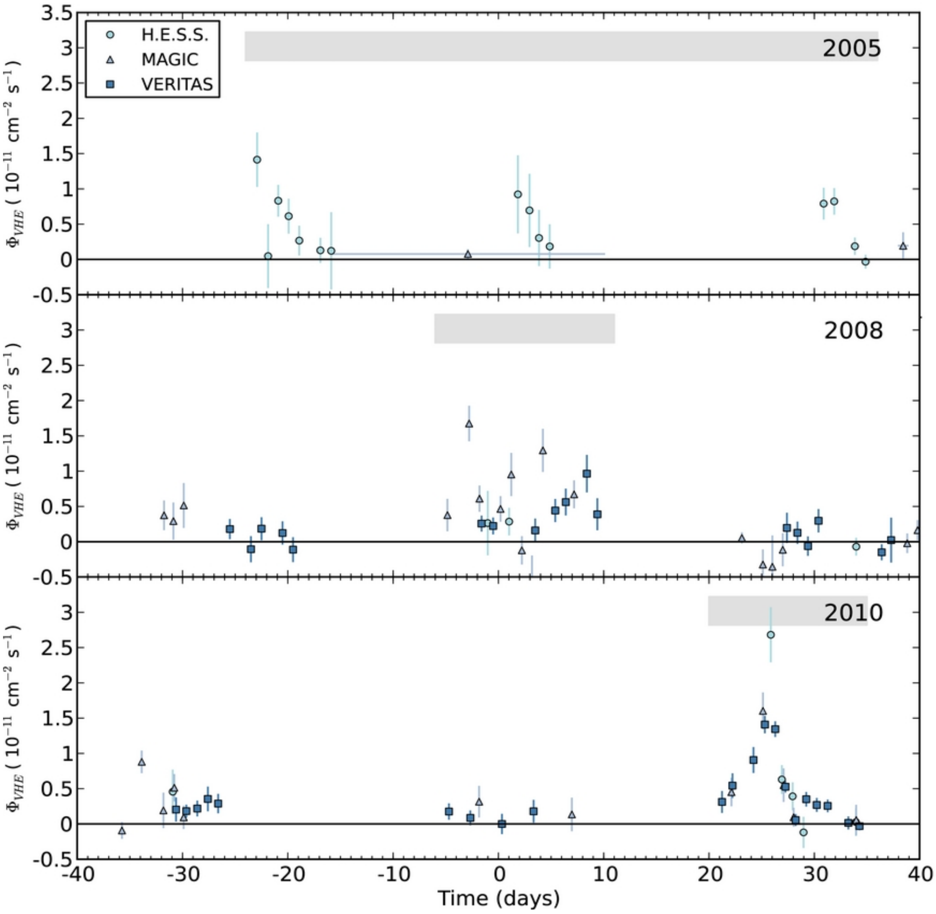

Figure 1.13: Light curves of the VHE γ-ray emission in M87 during flaring events in 2005 (upper panel), 2008 (middle panel), and 2010 (lower panel). Integral fluxes are shown for energies above 350 GeV (Abramowski et al., 2012).

the source ranged from $\sim$ 300 GeV up to $\sim$ 10 TeV with a hard spectral index compatible with a single power law (i.e., $\Gamma_\gamma = -2.2 \pm 0.2$ in the high states and somewhat steeper $\Gamma_\gamma \approx -2.6$ in the low ones). It is worth noting that both the detected rapid VHE variability and the hard VHE spectrum are remarkable features for a misaligned AGN.

Using the first 10 months of *Fermi*-LAT data, HE γ-ray emission from galaxy M87 has been detected up to energies of $\sim$ 30 GeV (Abdo et al., 2009). A single power-law with exponent comparable to the indices in the VHE high states (i.e., $\Gamma_\gamma = -2.26 \pm 0.13$) could describe the HE spectrum. However, a simple extrapolation of the HE power-law to the VHE regime appeared insufficient to match the photon fluxes detected during the VHE episodes (i.e., flux level equivalent to $l_{TeV} \sim 5 \times 10^{41}\ erg^{-1}\, s$) (Aliu et al., 2012).

This fact suggests that the HE radiation and the VHE states may result from distinct physical processes (e.g., different primary particle distributions or sites of emission). In addition, these early HE γ-ray observations did not indicate any significant variation in the photon flux (down to time-scales of 10 days).

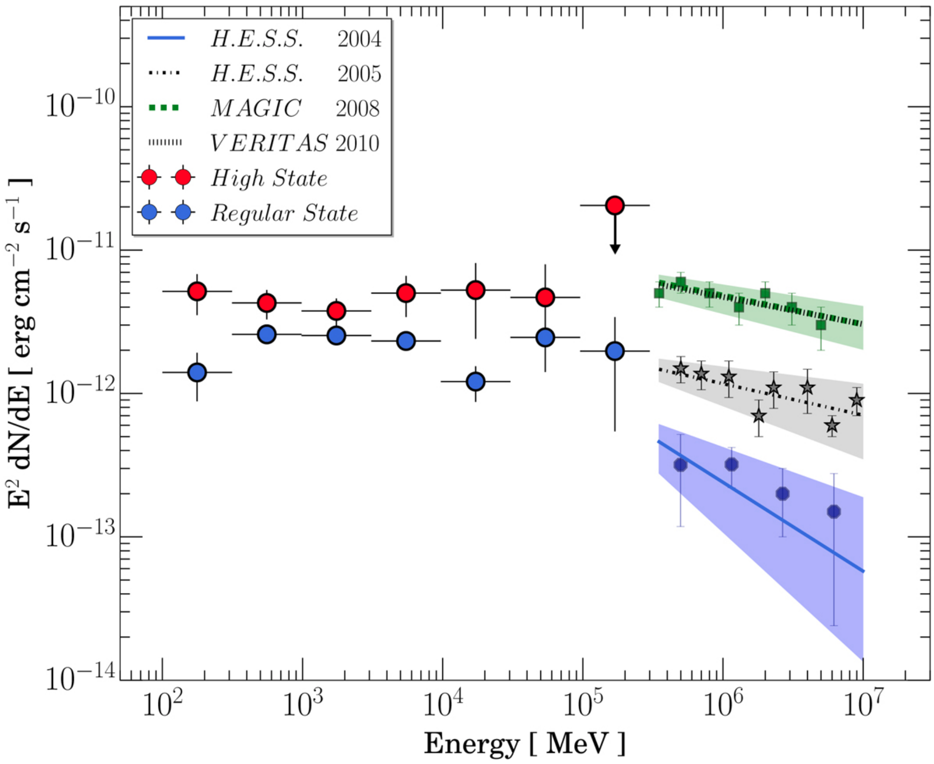

Figure 1.14: Spectral energy distribution (SED) in HE and VHE γ-rays for the active galaxy M87. The data points are based on Fermi-LAT and IACT observations. The average (regular) spectrum shows a break in the SED around $\sim$ 10 GeV (Benkhali et al., 2019).

Similar spectral characteristics have also been reported in the 3FGL catalogue (4 yr of data). More precisely, the HE γ-ray spectrum seems compatible with a single power-law (i.e., $\Gamma_\gamma = -2.04 \pm 0.07$) for energies below $\sim$10 GeV (Acero et al., 2015). Finally, the most recent analysis based on $\sim$ 8 yr of Fermi-LAT observations provides evidence for month-type HE variability and indications for a photon flux excess over the standard HE power-law model beyond $\sim$ 10 GeV (Benkhali et al., 2019). In figure (1.14) above, data of M87 throughout the whole γ-ray domain (i.e., HE and VHE) are shown. Accordingly, the change in the SED above $\sim$ 10 GeV suggests an additional emission component that dominates the VHE regime and allows for a smooth HE-VHE spectral connection (Benkhali et al., 2019). Since the HE spectrum extends up to $\sim$100 GeV without indications for a cut-off, while the VHE

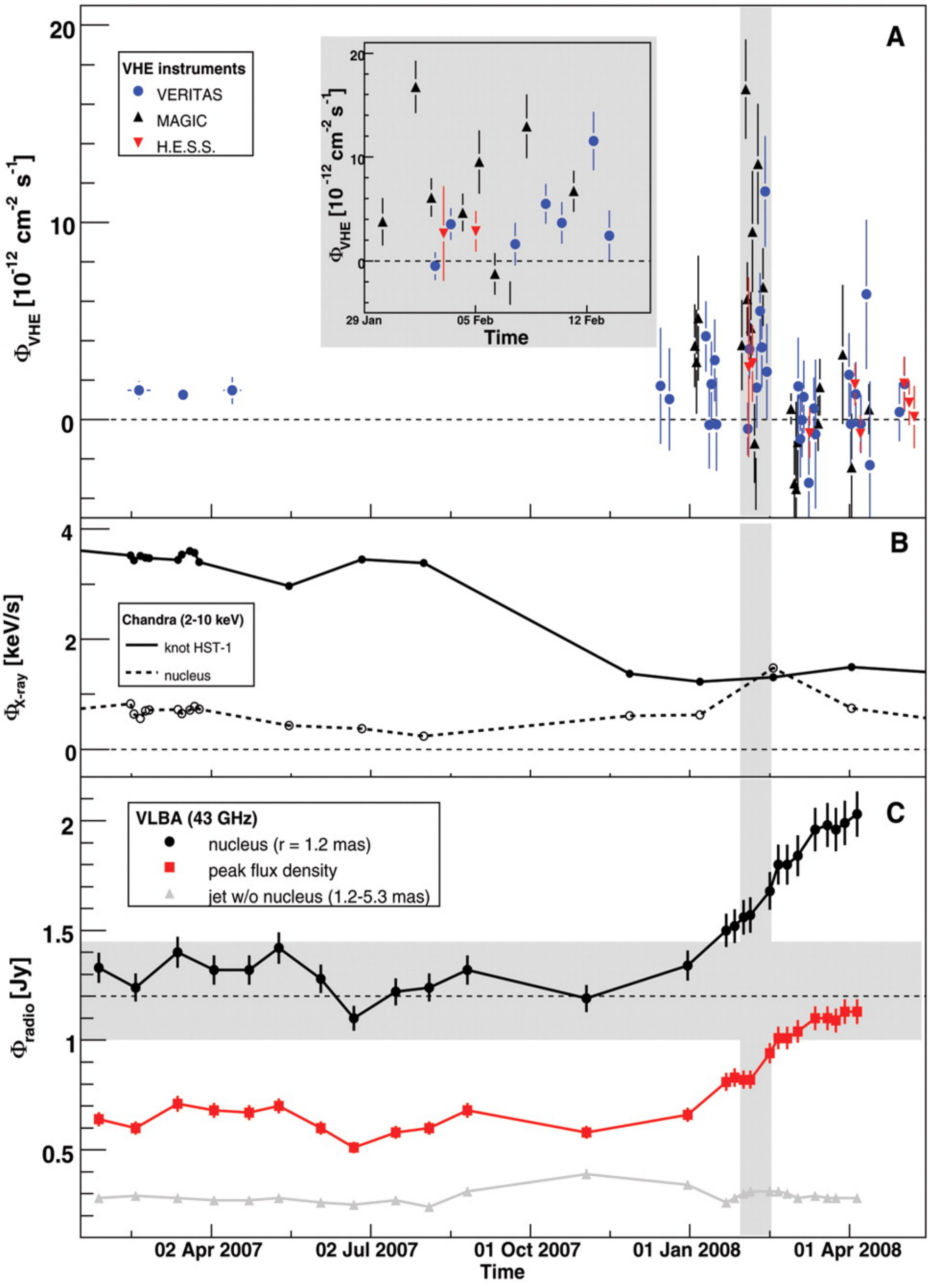

Figure 1.15: Light curves of the radio galaxy M87 in different spectral domains during 2007-2008. The VHE γ-ray fluxes as measured by ground-based observatories (upper panel), the Chandra X-ray emission (middle panel) as well as the 43-GHz VLBA observations (lower panel) of the nucleus and the bright knot HST-1, respectively, indicate a radio-VHE correlation of the nucleus. The VHE outburst in February 2008 is followed by an increase in radio activity of the nucleus (Acciari et al., 2009).

thresholds reach down to ∼200 GeV, flux variability observed by means of high statistics at VHE can be used to constrain the nature of this additional component.

In order to overcome the observational limitations (i.e, low quality angular resolution) and explore the size and the location of the emitting region, variability studies or/and multi-wavelength campaigns can be employed. As it has been mentioned above, the VHE γ-ray emission produced in M87 is highly variable, namely day-scale flux variations have been recorded. Using light travel time arguments one can derive that the corresponding size h of the VHE emitting region is comparable to the gravitational radius (i.e., $r_g = GM/c^2$) of the central black hole (e.g., in the case of M87, $h = \delta c \Delta\tau_{obs} \sim r_g$). This fact indicates a very compact VHE emission zone.

In addition, Very Long Baseline Interferometry (VLBI)[6] radio observations of M87 performed during the VHE flaring events in 2008, 2010, and 2012, imply that the VHE γ-ray emission is correlated with radio core flux enhancements (e.g., see figure 1.15) and not with the others bright knots of the spatially resolved radio-jet (Acciari et al., 2009; Hada et al., 2012, 2014; Akiyama et al., 2015). The inferred compactness of the emitting region as well as the multi-wavelength correlations of the TeV emission with radio core flux amplifications suggest that the VHE γ-ray radiation may originate at the jet base very close to the black hole.

1.3.2 The radio galaxy IC310

The extragalactic radio galaxy IC 310, member of *Perseus* Cluster and located at distance of 80 Mpc, has been recently identified (see figure 1.16) as strong VHE γ-ray emitter (Aleksić et al., 2010). IC310 is commonly considered to host a supermassive black hole of mass, $M = 3 \times 10^8 M_\odot$, in its central galactic region (Berton et al., 2015). The apparent lack of jet bending (e.g., see the radio contours in the insets of figure 1.16) along with recent indications for an inclined (i.e., $\theta_{los} \leq 38^o$), pc-scale, one-sided, radio jet suggest that IC 310 is possibly found in the transitional zone between the low luminosity radio galaxies and BL Lacs objects(Kadler et al., 2012).

In the VHE regime, the source was originally detected by MAGIC during a campaign in 2009 (Aleksić et al., 2010). In *November* 2012 IC 310 showed a strong, VHE flaring state during which extreme flux variability was revealed (Aleksic et al., 2014a). More specifically, during a high γ-ray state of $\sim$ 25 min intensive, VHE flux variations were recorded on timescales as short as

---

[6] For comparison, the VLBI angular resolution ($\sim$ 1 *mas* or 0.08 pc projected distance) is much better than the VHE resolution ($\sim 0.1^o$ or 30 kpc projected distance).

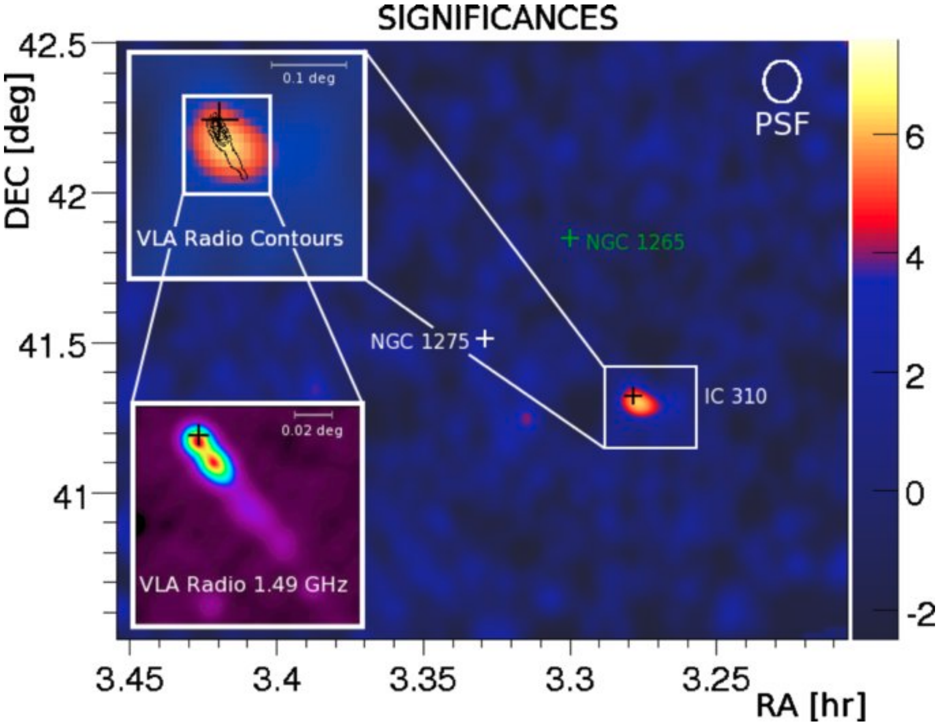

Figure 1.16: Significance skymap of the radio galaxy IC 310 at VHE γ-rays (i.e, here above 400 GeV). In addition, radio maps included in the figure show the emerging jet/outflow from the radio core of IC310. The VHE observations were conducted by the MAGIC telescopes (Aleksić et al., 2010).

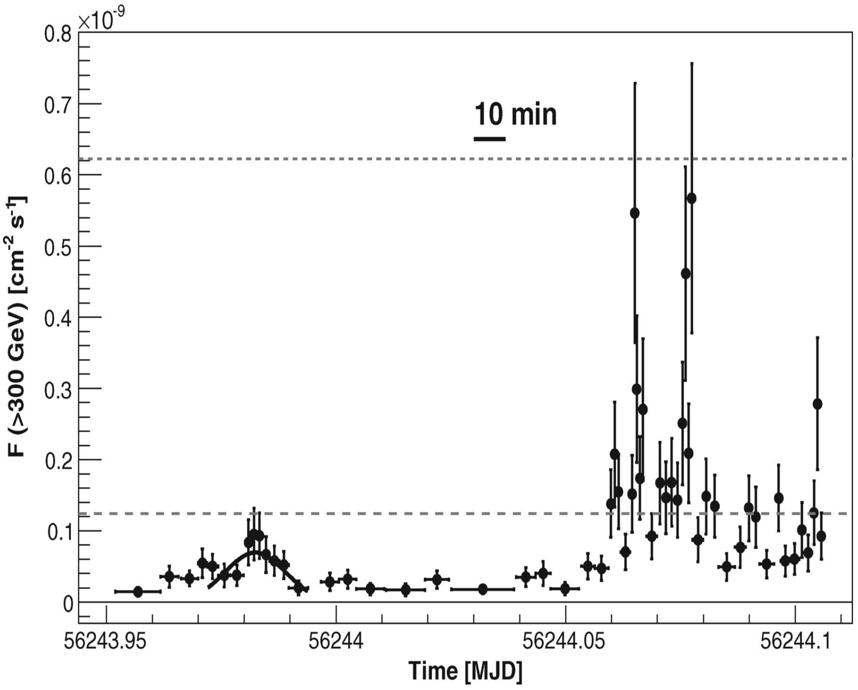

Figure 1.17: Light curve of the active galaxy IC 310 as detected by the MAGIC telescopes on the night of 12/13 November 2012 (Aleksic et al., 2014a). Rapid flaring activity down to a few minutes can be seen.

$\Delta\tau_{obs} \sim 5$ min (see the light curve in figure 1.17). No obvious correlation was detected between the VHE event and the flux level in other spectral wavelengths. The spectrum of the VHE flare as shown in figure (1.18) ranges from 70 GeV up to 8.3 TeV and appears compatible with a single, hard power law (i.e., $\Gamma_\gamma = -1.9 \pm 0.2$ or even lower, $\Gamma_\gamma = -1.5$, during the minute-scale variability) (Aleksic et al., 2014a; Ahnen et al., 2017). As it can be seen in figure (1.18) below, there is no indication of internal absorption. The source reached high photon fluxes which correspond to an isotropic-equivalent luminosity of, $l_{TeV} \sim 2 \times 10^{44}\ erg^{-1}\, s$.

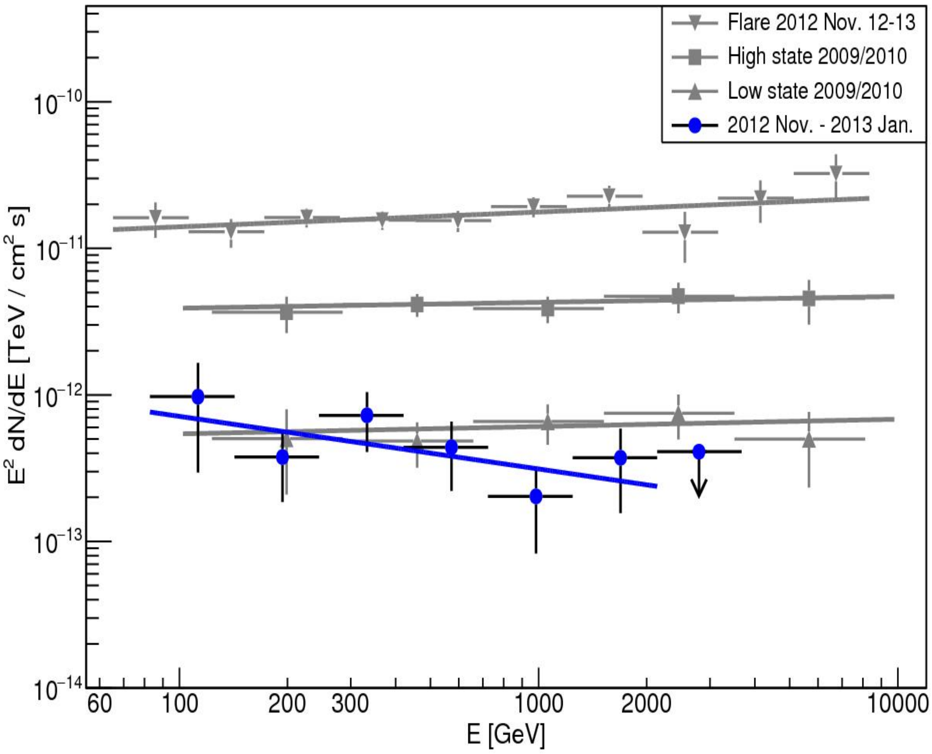

Figure 1.18: VHE spectra of IC310 for different flux states obtained by the MAGIC telescopes. For more details see (Aleksic et al., 2014a; Ahnen et al., 2017).

The extreme VHE variability combined with the high VHE fluxes and the hard γ-ray spectrum are surprising findings for a misaligned active galaxy, since negligible *Doppler-boosting* is expected for the intrinsic emission. Based on a variety of considerations (Aleksic et al., 2014a), including the jet orientation of IC310 (probably $\theta_{los} \sim 10^o - 20^0$) as well as the kinetic jet power and timing constraints, several alternative models for rapid VHE variability have been disfavoured (e.g., jet-cloud/star interaction or magnetic reconnection, Barkov et al., 2012; Giannios, 2013). The fact that the observed VHE flux varied on timescales much shorter than the time of the light travel across the black hole horizon (i.e., $\Delta\tau_{obs} < r_g/c = 25\,min$) has been interpreted as evidence for the occurrence of gap-type particle acceleration on sub-horizon scales (i.e., in unscreened electric field regions or "gaps", of height $h \lesssim 0.2r_g$, Aleksic et al., 2014a; Hirotani et al., 2016).

1.3.3 Other misaligned AGN as VHE emitters

Only a small number of galaxies which have been classified as misaligned AGN appear in the VHE *TeVcat* catalogue. This includes, the radio sources *Centaurus* A, PKS 0625-354, 3C 264 and NGC 1275, whose VHE γ-ray emission ranges (on average) from $\sim$ few hundreds GeV up to $\sim$ few TeV. The VHE spectrum varies for each galaxy, but they are all compatible with a hard power-law (i.e., $\Gamma_\gamma > -2.0$).

Since no substantial VHE flux variability has been observed from those galaxies, we will not further discuss them here. For more details (and references) on those objects the interested reader is referred to the recent review by Rieger and Levinson (2018).

1.4 Modelling the VHE flares of MAGN

Despite the progress over the last few years in γ-ray astronomy, γ-ray instruments (e.g., *Fermi*-LAT for the HE and H.E.S.S., MAGIC, VERITAS for the VHE band) have also weaknesses. For instance, they do not offer satisfactory angular resolution (i.e., $\sim 0.1^o$), such that extragalactic γ-ray sources can be spatially resolved or easily identified with the counterparts in the other wavelengths. Due to this fact, a plethora of possible scenarios have been proposed towards the interpretation of the nature of the non-thermal processes that take place in these sources and the possible sites of the variable GeV/TeV radiation.

One of the possibilities involves flow inhomogeneities in the velocity profile within the sub-pc jet (i.e., different jet layers moving with different bulk flow speeds). One can assume either longitudinal or radial jet stratification in order to model the source (e.g., see Georganopoulos et al., 2005; Tavecchio and Ghisellini, 2008, 2014). In the simplest bulk flow realization a slower (i.e, $\Gamma_B^{(sh)} \sim 1$) sheath surrounds a fast-moving (i.e., $\Gamma_B^{(sh)} \ll \Gamma_B^{(sp)}$) spine (Ghisellini et al., 2005; Tavecchio and Ghisellini, 2008). According to these models, the non-homogeneous velocity profile results in an enhancement of the inverse *Compton* (IC) emission in the TeV regime. Difficulties, however, arise due to internal absorption in the modelling of hard TeV spectra (Ansoldi et al., 2018).

Alternatively, one can assume that the sub-pc jet consists of blobs able to move along different paths within the jet (Giannios et al., 2009, 2010). These blobs could be localised, magnetic reconnection sites (i.e., *"mini-jets"*) within the jet (Nalewajko et al., 2011; Giannios, 2013; Sironi et al., 2015). Accordingly, electrons accelerated in the reconnected regions produce VHE γ-ray photons via inverse *Compton* scattering. In the so-called *jet-in-jet* model strong differential *Doppler*-boosting effects could become possible even for misaligned AGN, providing in such a way a simple explanation of the observed flux variability. In order to match, however, the model predictions with the detected γ-ray flux levels, a strong magnetization, which is usually not expected in electron-proton (disk-driven) outflows, is required.

A third idea suggests that the observed VHE γ-ray radiation and flux variability can be related to the interaction of the AGN jet/outflow with red giant stars or clouds (Barkov et al., 2010, 2012; Bosch-Ramon et al., 2012). According to this scenario, protons originating from the star/cloud material spread within the relativistic jet. In the following, protons may experience strong acceleration at the shock formed due to the jet-star/cloud collision/interaction. The VHE component of the spectrum is generated via inelastic proton-proton (pp) collisions. Although the ubiquity of stars and gas in the central galactic region can lead to frequent jet-star/cloud interplays, extreme jet power is usually required (i.e., in excess of current estimates) to account for the observed VHE emission.

In this doctoral study, the so-called magnetospheric scenario is adopted. We aim to explore the observational consequences implied by this assumption, motivated by the highly variable VHE activity of prominent misaligned AGN. In this model, lepton acceleration accompanied by radiative processes occurring in the vicinity of the central supermassive black hole (i.e., the black hole magnetosphere) can be responsible for the observed VHE radiation (Levinson and Rieger, 2011). Particles injected within the black hole magnetosphere are accelerated in regions of unscreened electric fields (i.e., "gap-type" acceleration) and emit VHE γ-ray photons via inverse *Compton* scattering and *curvature* radiation (Neronov and Aharonian, 2007; Levinson and Rieger, 2011; Ptitsyna and Neronov, 2016; Hirotani et al., 2016; Katsoulakos and Rieger, 2018).

1.5 Concluding remarks

The observation of the sky at high energies has opened up a fascinating window to the universe. Detections of astrophysical sources in γ-rays can be done either directly by means of space detectors orbiting the *Earth* or indirectly, via ground-based, massive detectors able to record the passage of γ-ray photons through the atmosphere. In this chapter, we highlighted γ-ray observations of misaligned (i.e., non-blazar) AGN. More specifically, the VHE flaring activity observed in the radio galaxies M87 and IC310 represents the starting point of this doctoral study. The observed rapid γ-ray variability, the substantial inclination of their relativistic jet/outflow with respect to the *line-of-sight* as well as the radio-VHE correlation in M87 nucleus give a strong motivation for testing physical scenarios associated with the vicinity of the central supermassive black hole.

The doctoral study is organized into the following structure. In chapter (2), we present the basic features of the considered AGN topology (i.e., the BH magnetosphere, the jet and the accretion disk). We then, in chapter (3), use a phenomenological description to obtain first insights into the magnetospheric processes. Finally, in chapter (4) we develop an one-dimensional (1D), steady, gap particle accelerator in the context of a *Kerr* black hole magnetosphere. The results are compared with observations and the consequences discussed.

Chapter 2

Magnetospheres of fast rotating black holes and accretion

In the first chapter, we reviewed HE and VHE γ-ray observations of prominent extragalactic sources. In particular, we focused on the highly variable (i.e., on timescales comparable to $\sim r_g/c$), VHE γ-ray emission detected in the radio galaxies M87 and IC310. As already mentioned, the observed variability implies very compact emitting regions and motivates an exploration of magnetospheric particle acceleration and emission scenarios.

Before studying the radiative processes occurring in the magnetosphere of a rapidly rotating black hole (i.e., chapter three and four), it is necessary to introduce the basic physics and topology of an AGN. This will help us to understand better the electrodynamic structure outside the central supermassive black hole and implement the appropriate processes for particle acceleration and VHE radiation.

Nuclear activity is triggered, when adjacent material usually concentrated on a disk-like shape accretes onto the central black hole (Shakura and Sunyaev, 1973). During accretion, a fraction of the gravitational energy is released via radiation, while some other amount is advected through the black hole event horizon. In addition, the falling material is thought to carry a large scale magnetic field whose field lines possibly thread the horizon at the inner edge of the accretion disk. The rapid rotation of the black hole along with the presence of magnetic field result in the formation of collimated, current-driven, relativistic jets extending to very large distances from the nucleus. In such a way, energy and angular momentum are efficiently extracted from the system (Blandford and Znajek, 1977). In figure (2.1) below, an artistic illustration of the AGN-phenomenon is shown.

In this chapter, we summarize the physics of the *disc-BH-jet* system. More specifically, we give a description (i.e., the electrodynamic structure)

Figure 2.1: Artistic illustration of a central supermassive black hole surrounded by the falling gas (i.e., the accretion disk). A relativistic jet is formed due to the rotation of the black hole and the presence of large scale magnetic field (NASA/JPL-Caltech).

of the *steady*, *axisymmetric*, *degenerate* and *force-free* magnetosphere of a fast rotating black hole. Black hole magnetospheres of *force-free* type are considered to extract efficiently the rotational energy of the black hole, namely they lead to outflow/jet formation. As we will show later on, however, surfaces/sites for efficient particle acceleration (i.e., unscreened electric fields) are possible even in a *force-free* magnetosphere. Finally, we discuss accretion and provide a brief overview about *advection dominated accretion flows* (ADAF). The ADAF (or *radiatively inefficient accretion flow* [RIAF]) plays a key role in the production of detectable VHE magnetospheric radiation. The aim of this chapter is, firstly, to highlight the basic operation and topology of AGN and, secondly, to provide the theoretical background needed in the next chapters.

2.1 Black hole magnetospheres and jets

In this section, we study the spacetime and the electrodynamics as realized outside a rapidly rotating (i.e., *Kerr*) black hole (Thorne et al., 1986). Furthermore, we discuss the critical surfaces/sites within the magnetospheric structure, where efficient particle acceleration may occur. We then discuss an explanation for the formation of jets (Blandford and Znajek, 1977). For all these, we will develop our considerations in the frame of the "3 + 1" formalism (Thorne and Macdonald, 1982).

2.1.1 The *Kerr* metric

Let us consider a black hole of mass M rotating rapidly in spacetime with angular momentum $J = GM^2/c$, where G and c are the gravitational constant and the speed of light respectively. The *absolute space*[1] around the black hole is described, using a *Boyer-Lindquist* spatial coordinate system (r,θ,ϕ), by the metric (Thorne et al., 1986):

$$ds^2 = \gamma_{rr} dr^2 + \gamma_{\theta\theta} d\theta^2 + \gamma_{\phi\phi} d\phi^2, \tag{2.1}$$

where γ_{ij} are the matrix elements of the space-metric tensor[2]:

$$\gamma_{ij} = \begin{pmatrix} \rho^2/\Delta & 0 & 0 \\ 0 & \rho^2 & 0 \\ 0 & 0 & \widetilde{\omega}^2 \end{pmatrix}, \tag{2.2}$$

with ρ, Δ and $\widetilde{\omega}$ given by the expressions:

$$\rho^2 = r^2 + \alpha_s^2 \cos^2\theta, \tag{2.3}$$

$$\Delta = r^2 - 2r_g r + \alpha_s^2, \tag{2.4}$$

$$\widetilde{\omega} = \frac{\Sigma}{\rho} \sin\theta, \tag{2.5}$$

---

[1] In the frame of "3 + 1" formulation the 4-dimensional spacetime splits into a 3-dimensional space, i.e., *absolute space*, and 1-dimensional time, i.e, the global time t, (For details see, Thorne et al., 1986).

[2] The *inverse* matrix of the metric tensor is:

$$\gamma^{ij} = \begin{pmatrix} \Delta/\rho^2 & 0 & 0 \\ 0 & 1/\rho^2 & 0 \\ 0 & 0 & 1/\widetilde{\omega}^2 \end{pmatrix}.$$

and the function Σ given by:

$$\Sigma^2 = (r^2 + \alpha_s^2)^2 - \alpha_s^2 \Delta \sin^2\theta. \tag{2.6}$$

In addition, we have defined the gravitational radius, $r_g = GM/c^2$, and the spin parameter of the black hole, $\alpha_s = J/Mc$.

In the "3+1" formalism all the laws and physical quantities are measured by *fiducial observers* (FIDOs)[3] carrying their own clocks and located in each point of *absolute* space. Given that the black hole rotates and drags all the physical objects near it, FIDOs must also have a radius-dependent, finite, angular velocity relative to *absolute* space:

$$\left.\frac{d\phi}{dt}\right|_{FIDO} = -\beta^{\phi} = \omega. \tag{2.7}$$

Furthermore, the gravity of the black hole causes a gravitational *redshift* to their clocks. Their lapse of proper time $d\tau$ is related to the lapse of the global time dt via the function:

$$\left.\frac{d\tau}{dt}\right|_{FIDO} = \alpha_l. \tag{2.8}$$

Evidently, in "3+1" splitting *general relativistic* effects become apparent via the so called *Lapse* function and *Lense-Thirring* angular velocity:

$$\alpha_l = \frac{\rho\sqrt{\Delta}}{\Sigma}, \qquad \omega = \frac{2c\alpha_s r_g r}{\Sigma^2}. \tag{2.9}$$

Finally, imposing $\Delta = 0$, we find the event horizon radius:

---

[3] In the case of *Kerr* black holes, the fiducial observers are also called *zero angular momentum observers* (ZAMOs).

$$r_H = r_g + \sqrt{r_g^2 - \alpha_s^2}, \tag{2.10}$$

and the event horizon angular velocity (thereafter, the angular velocity of the black hole):

$$\Omega^H = \frac{c\alpha_s}{2r_g r_H}. \tag{2.11}$$

2.1.2 Black hole electrodynamics

As already mentioned, the (neutral) gas, which surrounds the central black hole, carries inwards its own magnetic field. At the innermost part, magnetic field lines are thought to thread the event horizon. A large scale electric field, on the other hand, is induced in the vicinity of the black hole either due to the presence of some charge density in the region (*Gauss's* law) or due to the rapid rotation of the black hole causing changes in the magnetic flux (*Faraday's* law) (Thorne et al., 1986).

Let us now assume a *steady*, *axisymmetric*, *degenerate* and *force-free* magnetosphere (i.e., $\partial/\partial t = 0$; $\partial/\partial\phi = 0$; $\mathbf{E}\cdot\mathbf{B} = 0$; $\rho_e\mathbf{E} + \mathbf{j}/c \times \mathbf{B} = 0$)[4], as realized in the presence of a rapidly rotating black hole. Under these assumptions, *Maxwell's* equations are given by (Macdonald and Thorne, 1982):

$$\nabla \cdot \mathbf{E} = 4\pi\rho_e, \tag{2.12}$$

$$\nabla \cdot \mathbf{B} = 0, \tag{2.13}$$

$$\nabla \times (\alpha_l\,\mathbf{B}) = \frac{4\pi}{c}\alpha_l\,\mathbf{j}, \tag{2.14}$$

$$\nabla \times (\alpha_l\,\mathbf{E}) = 0, \tag{2.15}$$

---

[4] Though these assumptions simplify the problem significantly, the basic concept of black hole electrodynamics is still captured. In addition, *force-free* condition is usually associated with efficient energy extraction and jet launching.

where ρ_e, $\mathbf{E}$, $\mathbf{B}$ and $\mathbf{j}$ represent the charge density, the electric field, the magnetic field and the current density, respectively.

We note, that these quantities are measured by the fiducial observers, since they describe physical laws in *absolute* space. Therefore, all computations are performed in the three-dimensional space metric of equation (2.2), namely:

$$\nabla \cdot \mathbf{E} = \frac{1}{|\sqrt{\gamma}|} \frac{\partial}{\partial x^i} \left(\sqrt{|\gamma|}\, E^i \right), \tag{2.16}$$

and:

$$\nabla \times (\alpha_l\, E) = \frac{\alpha_l}{\sqrt{|\gamma|}} \begin{pmatrix} \sqrt{\gamma_{rr}}\, \mathbf{e}_{\hat{r}} & \sqrt{\gamma_{\theta\theta}}\, \mathbf{e}_{\hat{\theta}} & \sqrt{\gamma_{\phi\phi}}\, \mathbf{e}_{\hat{\phi}} \\ \partial/\partial r & \partial/\partial\theta & \partial/\partial\phi \\ \sqrt{\gamma_{rr}}\, E_{\hat{r}} & \sqrt{\gamma_{\theta\theta}}\, E_{\hat{\theta}} & \sqrt{\gamma_{\phi\phi}}\, E_{\hat{\phi}} \end{pmatrix}, \tag{2.17}$$

where $(\mathbf{e}_{\hat{r}}, \mathbf{e}_{\hat{\theta}}, \mathbf{e}_{\hat{\phi}})$ are the physical unit vectors, i.e., the orthonormal basis, $\sqrt{|\gamma|} = \sqrt{det|\gamma_{ij}|} = \rho^2 \widetilde{\omega}/\sqrt{\Delta}$ is the determinant of the metric and $i = r, \theta, \phi$. We denote the *contravariant* and *covariant* components of the electric field with E^i and E_i, respectively.

In *General Relativity*, vectors can be decomposed into the physical components $(\mathbf{e}_{\hat{r}}, \mathbf{e}_{\hat{\theta}}, \mathbf{e}_{\hat{\phi}})$, into *contravariant* components by means of the coordinate basis $(\mathbf{e}_r, \mathbf{e}_\theta, \mathbf{e}_\phi)$ or into *covariant* ones by means of the *1-form* $(\mathbf{e}^r, \mathbf{e}^\theta, \mathbf{e}^\phi)$. The coordinate basis and the *1-form* in terms of physical components are given by $\mathbf{e}_i = \sqrt{\gamma_{ii}} \mathbf{e}_{\hat{i}}$ and $\mathbf{e}^j = \frac{1}{\sqrt{\gamma_{jj}}} \mathbf{e}_{\hat{j}}$ (Thorne and Macdonald, 1982; Beskin, 2010).

Alternatively, we can express the above laws (equations 2.12-2.15) in integral form (Thorne et al., 1986)[5]:

$$\int_{\mathcal{S}} \mathbf{E} \cdot d\mathbf{S} = 4\pi \int_{\mathcal{V}} \rho_e\, dV, \tag{2.18}$$

$$\int_{\mathcal{S}} \mathbf{B} \cdot d\mathbf{S} = 0, \tag{2.19}$$

---

[5] Given that we investigate the steady state problem, we have set $\mathbf{v} = 0$ in the corresponding relations of Thorne et al. (1986).

$$\oint_{\mathcal{I}} \alpha_l \mathbf{E} \cdot d\mathbf{l} = 0, \tag{2.20}$$

$$\oint_{\mathcal{I}} \alpha_l \mathbf{B} \cdot d\mathbf{l} = \frac{4\pi}{c} \int_{\mathcal{S}} \alpha_l \, \mathbf{j} \cdot d\mathbf{S}, \tag{2.21}$$

where $\mathcal{V}$ represents a (steady) half sphere volume in *absolute* space attached as a dome to the accretion disk and covering the space outside the black hole (see figure 1 in Macdonald and Thorne, 1982). Furthermore, $\mathcal{S}$ denotes the surface boundary of volume $\mathcal{V}$ and $\mathcal{I}$ the closed-curved boundary along the equator (i.e, the base) of the half sphere.

In order to facilitate the operations, we define the following quantities (see equations 2.18-2.21):

$$I = -\int_{\mathcal{S}} \alpha_l \, \mathbf{j} \cdot d\mathbf{S}, \tag{2.22}$$

and:

$$\Psi = \int_{\mathcal{S}} \mathbf{B} \cdot d\mathbf{S}, \tag{2.23}$$

where I and Ψ represent the total current passing downwards through loop $\mathcal{I}$ and the total magnetic flux passing through the surface boundary $\mathcal{S}$, respectively. In the following, we seek to express ρ_e, $\mathbf{E}$, $\mathbf{B}$ and $\mathbf{j}$ in terms of the freely-specifiable scalar potentials, that is Ψ, I and the electric potential ϕ_E. For easier manipulation of the equations, it is convenient to separate $\mathbf{E}$, $\mathbf{B}$ and $\mathbf{j}$ into poloidal (i.e., in the plane $[r, \theta]$) and toroidal (i.e., along ϕ-direction) components. Hence, we write:

$$\mathbf{E} = \mathbf{E}^P + \mathbf{E}^T, \tag{2.24}$$

$$\mathbf{B} = \mathbf{B}^P + \mathbf{B}^T. \tag{2.25}$$

From equation (2.20) (*Faraday's* law) and using relation (2.24), one obtains:

$$\oint_{\mathcal{I}} \alpha_l \, \mathbf{E} \cdot d\mathbf{l} = \oint_{\mathcal{I}} \alpha_l \, \mathbf{E}^P \cdot d\mathbf{l} + \oint_{\mathcal{I}} \alpha_l \, \mathbf{E}^T \cdot d\mathbf{l} = 0, \tag{2.26}$$

which directly implies that $\mathbf{E}^T = 0$ given that the vector $d\mathbf{l}$ is taken along ϕ-direction. Therefore, the electric field, $\mathbf{E}$, is lying in the poloidal plane. In addition, from equation (2.13) we have:

$$\nabla \cdot \mathbf{B} = 0 \Rightarrow \mathbf{B} = \nabla \times \mathbf{A}, \tag{2.27}$$

where $\mathbf{A}$ is the 3-vector potential[6]. Following the classical definition, the electric field in terms of potentials can be written as (Thorne and Macdonald, 1982):

$$\mathbf{E} = \frac{1}{\alpha_l} \left(\nabla \phi_E + \frac{\omega}{c} \nabla A_\phi \right). \tag{2.28}$$

We can now associate A_ϕ with the magnetic flux Ψ using equations (2.23) and (2.27). We find that:

$$\Psi = \int_{\mathcal{S}} \mathbf{B} \cdot d\mathbf{S} = \int_{\mathcal{S}} (\nabla \times \mathbf{A}) \cdot d\mathbf{S} = \oint_{\mathcal{I}} \mathbf{A} \cdot d\mathbf{l} = 2\pi A_\phi. \tag{2.29}$$

Hence, we can rewrite the (poloidal) electric field of equation (2.28) as:

$$\mathbf{E}^P = \frac{1}{\alpha_l} \left(\nabla \phi_E + \frac{\omega}{2\pi c} \nabla \Psi \right). \tag{2.30}$$

---

[6] In *General Relativity*, the 4-vector potential, A^κ, consists of the scalar electric potential ϕ_E and the 3-vector potential $\mathbf{A} = (A^r, A^\theta, A^\phi)$, i.e., $A^\kappa = (\phi_E/c, \mathbf{A})$.

Exploiting, on the other hand, the assumption of *axisymmetry*, equation (2.13) yields:

$$\nabla \cdot \mathbf{B} = \nabla \cdot \left(\mathbf{B}^P + \mathbf{B}^T\right) = \nabla \cdot \mathbf{B}^P = 0, \tag{2.31}$$

that is the poloidal and toroidal magnetic field components are characterized separately by field lines that never end. Using then formula (2.21) (*Ampere's* law) and the definition of the total current in relation (2.22), we can determine the toroidal magnetic field component:

$$\alpha_l \, |\mathbf{B}^T| \, \widetilde{\omega} \, \mathbf{e}_{\hat{\phi}} \;\; 2\pi \, \widetilde{\omega} \, \mathbf{e}_{\hat{\phi}} = -\frac{4\pi I}{c}, \tag{2.32}$$

that is:

$$\mathbf{B}^T = -\frac{2I}{\alpha_l \, \widetilde{\omega} \, c} \mathbf{e}_{\hat{\phi}}. \tag{2.33}$$

In order to estimate the poloidal component of the magnetic field, we need to move the loop $\mathcal{I}$ from a point $\mathbf{r}$ by $d\mathbf{r}$ (see, for example, figure 3 in Macdonald and Thorne, 1982). Accordingly, the magnetic flux changes by an amount of $d\Psi = \nabla\Psi \cdot d\mathbf{r}$. This change can be also written using the definition of magnetic flux in formula (2.23):

$$d\Psi = \mathbf{B} \cdot d\mathbf{S} = \left(d\mathbf{r} \times 2\pi \, \widetilde{\omega} \, \mathbf{e}_{\hat{\phi}}\right) \cdot \mathbf{B} = \left(2\pi \, \widetilde{\omega} \, \mathbf{e}_{\hat{\phi}} \times \mathbf{B}\right) \cdot d\mathbf{r}. \tag{2.34}$$

Comparing the above expressions we find:

$$\nabla\Psi = 2\pi\widetilde{\omega} \, \mathbf{e}_{\hat{\phi}} \times \mathbf{B} \Rightarrow \mathbf{B}^P = -\frac{\mathbf{e}_{\hat{\phi}} \times \nabla\Psi}{2\pi\widetilde{\omega}}, \tag{2.35}$$

since the contribution of $\mathbf{e}_{\hat{\phi}}$ in the outer product results in a poloidal vector.

Following the same line of reasoning as above (but now see equation 2.22), we can write the poloidal component of the current density as follows:

$$\nabla I = -2\pi\widetilde{\omega}\, \mathbf{e}_{\hat{\phi}} \times (\alpha_l \mathbf{j}^P) \Rightarrow \mathbf{j}^P = \frac{\mathbf{e}_{\hat{\phi}} \times \nabla I}{2\pi\, \alpha_l\, \widetilde{\omega}}, \tag{2.36}$$

while the ϕ-component of the current density can be estimated by equations (2.14), (2.33) and (2.35). Hence, after some manipulation we find (Macdonald and Thorne, 1982):

$$\mathbf{j}^T \cdot \mathbf{e}_{\hat{\phi}} = -\frac{c\,\widetilde{\omega}}{4\pi\alpha_l}\nabla \cdot \left(\frac{\alpha_l \nabla\Psi}{2\pi\widetilde{\omega}^2}\right) + \frac{\widetilde{\omega}}{4\pi\alpha_l^2}\nabla\omega \cdot \left(\nabla\phi_E + \frac{\omega\nabla\Psi}{2\pi c}\right). \tag{2.37}$$

Given that the electric field vanishes in the toroidal direction and considering *degeneracy* (i.e., $\mathbf{E}\cdot\mathbf{B} = 0$) in the magnetospheric regions, one can define the toroidal vector:

$$\mathbf{v}^F = \frac{1}{\alpha_l}\left(\Omega^F - \omega\right)\widetilde{\omega}\, \mathbf{e}_{\hat{\phi}}, \tag{2.38}$$

which can be interpreted as the physical velocity of the magnetic field lines relative to fiducial observers. Accordingly, $\Omega^F = d\phi/dt$ in equation (2.38) represents the angular velocity of the field lines relative to *absolute* space. The assumption of *degeneracy* can be justified in many astrophysical environments, where plasma with extremely high conductivity is present (Goldreich and Julian, 1969). Under these circumstances, the electric field is simply given by the following expression:

$$\mathbf{E}^p = -\frac{\mathbf{v}^F}{c} \times \mathbf{B}^P, \tag{2.39}$$

and via equation (2.38) we find:

$$\mathbf{E}^p = -\frac{\left(\Omega^F - \omega\right)}{2\pi c\, \alpha_l}\nabla\Psi. \tag{2.40}$$

Comparing now relations (2.30) and (2.40), one obtains:

$$\frac{d\phi_E}{d\Psi} = -\frac{\Omega^F}{2\pi c}, \tag{2.41}$$

namely, in *degenerate* magnetospheric regions the scalar electric potential ϕ_E is a function of the total magnetic flux Ψ. It is then possible to reformulate the toroidal component of the current in equation (2.37) using formula (2.41). Therefore, we can write:

$$\begin{split} 8\pi^2 j^T = -\frac{c\,\widetilde{\omega}}{\alpha_l}\nabla\cdot\left(\frac{\alpha_l}{\widetilde{\omega}^2}\nabla\Psi\right) + \\ \frac{\widetilde{\omega}}{\alpha_l^2\,c}\left(\Omega^F-\omega\right)\nabla\Psi\cdot\nabla\left(\Omega^F-\omega\right) - \frac{\widetilde{\omega}}{\alpha_l^2\,c}\left(\Omega^F-\omega\right)\frac{d\Omega^F}{d\Psi}\left(\nabla\Psi\right)^2. \end{split} \tag{2.42}$$

In addition, putting the expression for the electric field (formula 2.40) into equation (2.15), we obtain that:

$$\nabla\Omega^F \times \nabla\Psi + \nabla\Psi \times \nabla\omega = 0, \tag{2.43}$$

and, subsequently, via the poloidal component of the magnetic field (equation 2.35) we find:

$$\mathbf{B}^P \cdot \nabla\Omega^F = 0. \tag{2.44}$$

It turns out from the above equation that Ω^F is constant along field lines, that is each magnetic field line rotates with constant angular velocity, i.e., $\Omega^F = \Omega^F(\Psi)$. If we further assume *force-freeness* in the magnetosphere, also the scalar I is not independent of the magnetic flux Ψ. More precisely, using the *force-free* condition (i.e., $\rho_e \mathbf{E} + \mathbf{j}/c \times \mathbf{B} = 0$) and exploiting the fact that the electric field has vanishing ϕ-component we obtain:

$$(\mathbf{j} \times \mathbf{B})^T = 0 \Rightarrow \mathbf{j}^P \times \mathbf{B}^P = 0 \Rightarrow \mathbf{j}^P \parallel \mathbf{B}^P \Rightarrow \nabla\Psi \parallel \nabla I, \tag{2.45}$$

that is the total current I is also a function of the magnetic flux, i.e., $I = I(\Psi)$. Therefore, the poloidal component of the current (equation 2.26) now becomes:

$$\mathbf{j}^P = -\frac{1}{\alpha_l}\frac{dI}{d\Psi}\mathbf{B}^P, \tag{2.46}$$

while the total vector of the current density is given:

$$\mathbf{j} = -\frac{1}{\alpha_l}\frac{dI}{d\Psi}\mathbf{B}^P + \rho_e \mathbf{v}^F. \tag{2.47}$$

We can, eventually, estimate the amount of charges within the magnetosphere, substituting formula (2.40) into *Gauss's* law (i.e., in equation 2.12). Hence, the charge density is given:

$$\rho_e = -\frac{1}{8\pi^2 c}\nabla \cdot \left[\frac{(\Omega^F - \omega)}{\alpha_l}\nabla\Psi\right]. \tag{2.48}$$

We note that equation (2.48) constitutes the *general relativistic* version of the *Goldreich-Julian* charge density defined in the case of *pulsars* (Goldreich and Julian, 1969). It is worth emphasizing that the *Goldreich-Julian* charge density ensures *degeneracy* in space and no particle acceleration is possible to take place.

In the frame of "3 + 1" formalism, the *redshifted* total energy flux and angular momentum of the electromagnetic field as measured by fiducial observers are described by the following expressions (Macdonald and Thorne, 1982):

$$\mathbf{P} = \frac{1}{4\pi}\Big[\alpha_l\, c\, \mathbf{E}\times\mathbf{B} - \omega\,(\mathbf{E}\cdot\widetilde{\omega}\,\mathbf{e}_{\hat{\phi}})\,\mathbf{E} - \omega(\mathbf{B}\cdot\widetilde{\omega}\,\mathbf{e}_{\hat{\phi}})\,\mathbf{B} + \frac{1}{2}\omega\left(|\mathbf{E}|^2+|\mathbf{B}|^2\right)\widetilde{\omega}\,\mathbf{e}_{\hat{\phi}}\Big], \tag{2.49}$$

$$\mathbf{L} = \frac{1}{4\pi}\left[-(\mathbf{E}\cdot\widetilde{\omega}\,\mathbf{e}_{\hat{\phi}})\,\mathbf{E} - (\mathbf{B}\cdot\widetilde{\omega}\,\mathbf{e}_{\hat{\phi}})\,\mathbf{B} + \frac{1}{2}\left(|\mathbf{E}|^2+|\mathbf{B}|^2\right)\widetilde{\omega}\,\mathbf{e}_{\hat{\phi}}\right]. \tag{2.50}$$

Imposing that $\mathbf{E}^T = 0$ and keeping only the poloidal components of equations (2.49) and (2.50), we find the expressions of the energy and the angular momentum flowing along the poloidal plane, respectively:

$$\mathbf{P}^P = \frac{I}{2\pi}\left(\frac{\omega}{\alpha_l\, c}\mathbf{B}^P - \frac{\mathbf{E}\times\mathbf{e}_{\hat{\phi}}}{\widetilde{\omega}}\right), \tag{2.51}$$

namely the poloidal flow of the *redshifted* energy is partly orthogonal to $\mathbf{E}$ and partly along $\mathbf{B}^P$, while:

$$\mathbf{L}^P = \frac{I}{2\pi\,\alpha_l\, c}\mathbf{B}^P. \tag{2.52}$$

Substituting the poloidal electric field (formula 2.40) in equation (2.51), the flow of energy simply becomes:

$$\mathbf{P}^P = \frac{\Omega^F I}{2\pi\,\alpha_l\, c}\mathbf{B}^P. \tag{2.53}$$

Equations (2.52) and (2.53) reveal the importance of the global current I that flows through the black hole magnetosphere (i.e., downwards through $\mathcal{I}$-loop). Unless the total current is active, there is no energy and angular momentum flowing outwards. Hence, the observation of large-scale relativistic jets launched from the nucleus of AGN suggests that strong global currents may flow within the black hole magnetospheres.

To summarize this subsection, we highlight that the electrodynamic structure of a *stationary*, *axisymmetric*, *degenerate* and *force-free* magnetosphere of a fast rotating black hole is regulated by equation (2.40) and $\mathbf{E}^T = 0$ for the global electric field $\mathbf{E}$, equations (2.33) and (2.35) for the global magnetic configuration $\mathbf{B}$, equations (2.36) and (2.37) for the total current density $\mathbf{j}$ and, finally, equation (2.48) for the charge density ρ_e. As already mentioned, these physical quantities are determined from three freely specifiable scalar fields, that is the total magnetic flux Ψ, the total current I and electric potential ϕ_E (or Ω^F in *degenerate* regions). We have shown that Ω^F and I are both functions of Ψ, i.e., $\Omega^F = \Omega^F(\Psi)$ and $I = I(\Psi)$, in case of *degeneracy* and *force-freeness*. Consequently, assuming a magnetic topology via the total magnetic flux, Ψ, and knowing the relation of Ψ with the current I and the field line angular velocity Ω^F, we can determine the structure of the black hole magnetosphere. In order to find I and Ω^F, however, as function of Ψ, one must solve numerically the *force-free* condition (i.e., $\rho_e \mathbf{E} + \mathbf{j}/c \times \mathbf{B} = 0$) which substituting all the quantities becomes:

$$\nabla \cdot \left\{ \frac{\alpha_l}{\widetilde{\omega}^2} \left[1 - \frac{\left(\Omega^F - \omega\right)^2 \widetilde{\omega}^2}{\alpha_l^2\, c^2} \right] \nabla\Psi \right\} + \frac{\left(\Omega^F - \omega\right)}{\alpha_l\, c^2} \frac{d\Omega^F}{d\Psi} \left(\nabla\Psi\right)^2 + \frac{16\pi^2}{\alpha_l\, \widetilde{\omega}^2\, c^2} I \frac{dI}{d\Psi} = 0 \tag{2.54}$$

Formula (2.54) is the so called *transfield* equation. For general *force-free* solutions of *Maxwell's* equations (i.e., solutions that satisfy relation 2.54), we refer the interested reader to Fendt (1997); Contopoulos et al. (1999); Fendt and Memola (2001); Uzdensky (2004); Komissarov (2004); Uzdensky (2005); Nathanail and Contopoulos (2014). We note that the examples of magnetospheres presented in this chapter below are not full solutions and, therefore, do not necessarily satisfy equation (2.54).

2.1.3 Critical surfaces and particle acceleration

The *transfield* equation is a non-linear, second order, elliptic PDE[7]. As can be seen, there are some critical surfaces where equation (2.54) becomes singular

---

[7] We use PDE as abbreviation of the term *"partial differential equation"*.

and, furthermore, reduces to a non-linear, first order PDE. Accordingly, two types of singular surfaces are included in the *transfield* equation:

- The black hole event horizon given by the condition that the *Lapse* function vanishes, $\alpha_l = 0$. Indeed, we have:

$$\alpha_l = \Delta = 0 \Rightarrow r_H = r_g + \sqrt{r_g^2 - \alpha_s^2}. \tag{2.55}$$

- The light cylinders given by the condition:

$$1 - \frac{\left(\Omega^F - \omega\right)^2 \widetilde{\omega}^2}{\alpha_l\, c^2} = 0, \tag{2.56}$$

where we obtain an inner and outer light surface, respectively:

$$\widetilde{\omega}_{LC}^{inner} = \frac{\alpha_l\, c}{\omega - \Omega^F}, \qquad \widetilde{\omega}_{LC}^{outer} = \frac{\alpha_l\, c}{\Omega^F - \omega}. \tag{2.57}$$

The inner light surface lies between the horizon and the static limit (i.e., the boundary of the ergosphere). Outside the outer light surface (OLS) and inside the inner light surface (ILS) magnetic field lines rotate faster than the speed of light with respect to fiducial observers. Between the two light surfaces, an other surface where $\Omega^F = \omega$ exists (see equation 2.54). According to equation (2.40), the electric field, which is perpendicular to the magnetic field in a *degenerate* and force-free magnetosphere, seems to vanish within this surface. Since the electric field is a continuous physical quantity, we can plausibly assume that it becomes parallel with the magnetic field lines. Therefore, particles injected somehow into this thin layer and moving along the magnetic field lines are subjected to strong acceleration in these parallel electric field components. We note, furthermore, that the charge density changes sign (see equation 2.48) across this surface (thereafter *null* surface), implying that *degeneracy* breaks down (i.e., $\mathbf{E} \cdot \mathbf{B} \neq 0$), unless continuous charge replenishment occurs. In chapter (4), we develop an analytical model (i.e, the [1D] steady "gap accelerator"), trying to explore the distribution of the parallel electric field and the charges within this layer.

In addition to the aforementioned discussion about the *null* surface, the *stagnation* surface is also considered to be a plausible candidate for particle acceleration. The *stagnation* layer in magnetohydrodynamics (MHD) is the boundary among neutral inflows and outflows. The low plasma density in these regions is thought to lead to non-vanishing, parallel, electric field components. In a *stationary* and *axisymmetric* black hole magnetosphere, stagnation surface is defined by the condition (Takahashi et al., 1990):

$$\kappa_o' = 0, \tag{2.58}$$

where the prime denotes the derivative along the field lines and:

$$\kappa_o = -g_{tt} - 2g_{t\phi}\Omega^F - g_{\phi\phi}{\Omega^F}^2. \tag{2.59}$$

The elements g_{ij} are the metric elements of the spacetime. Particle acceleration in the stagnation layer has been recently studied by Broderick and Tchekhovskoy (2015); Hirotani and Pu (2016).

In figures (2.2) and (2.3) below, stationary, axisymmetric, *degenerate*, *force-free* black hole magnetospheres are illustrated for two different magnetic configurations (i.e, $\Psi \sim r^2 \sin^2\theta$; vertical lines threading the equator and $\Psi \sim (1 - \cos\theta)$; split monopole, respectively). All the relevant surfaces have also been included, indicating the possible sites for efficient particle acceleration (i.e., see the *null* surfaces [red lines] and the *stagnation* ones [green lines]). For the derivation, we assumed a rapidly rotating black hole with spin parameter close to unity, $\alpha_s = 0.998$, and a typical value for Ω^F, i.e., $\Omega^F = \Omega^H/2$. Contour levels of the charge density have also been drawn. In figure (2.4) below, we present a map of the ratio $|\mathbf{E}|/|\mathbf{B}|$. The vanishing (perpendicular) electric field in the poloidal plane reveals the exact location of the *null* surface.

For comparison, in figure (2.5), we depict a vacuum black hole magnetosphere (Wald, 1974; Thorne et al., 1986). The red arrows in the figure

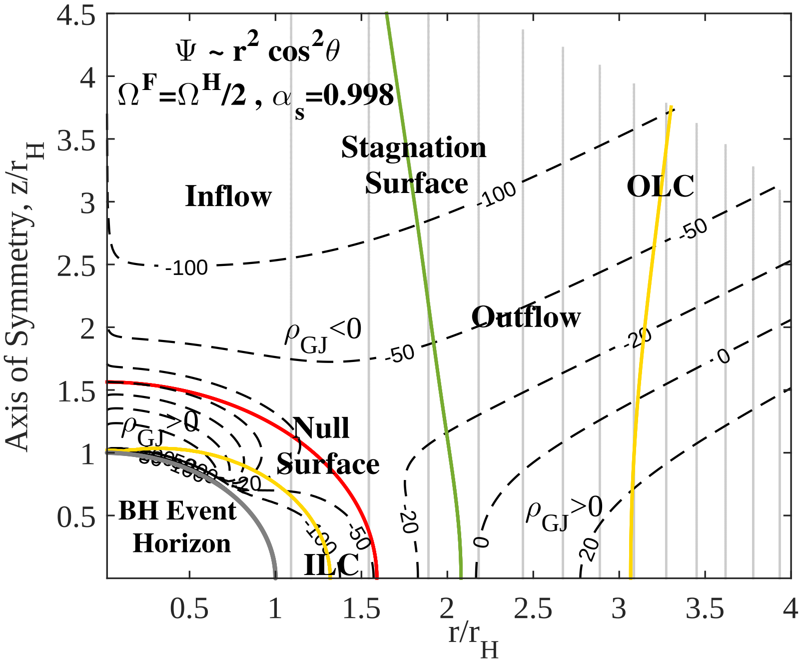

Figure 2.2: Poloidal representation of a black hole magnetosphere with assumed magnetic flux function of $\Psi \sim r^2 \sin^2\theta$, i.e., vertical magnetic field lines which thread the equator (grey lines). Potential sites for particle acceleration, i.e., the null surface (red line) and the stagnation surface (green line), are located between the two light cylinders (yellow lines). Contour levels of the charge density (dashed lines) have also been included.

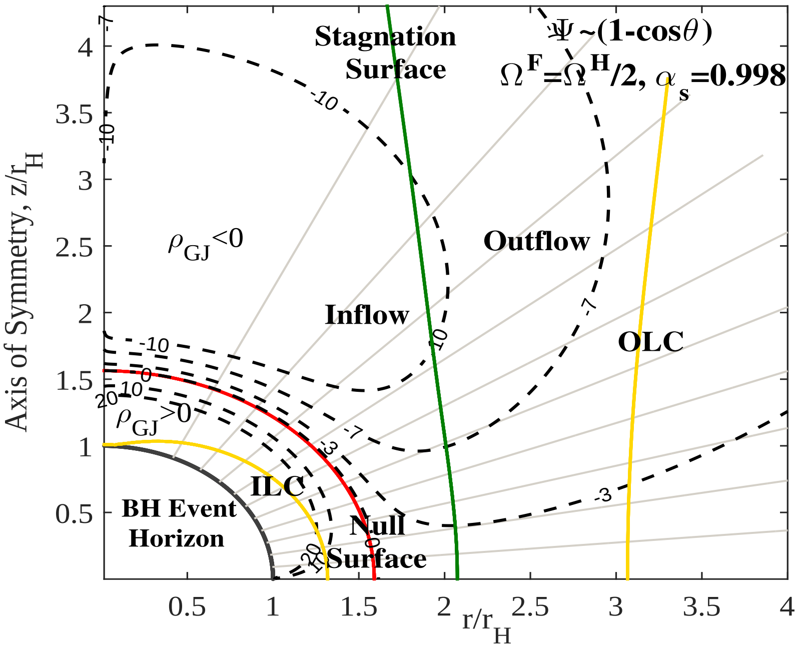

Figure 2.3: Poloidal illustration of a black hole magnetosphere with assumed magnetic configuration of a split monopole, i.e., $\Psi \sim (1 - \cos\theta)$ (grey lines). Potential sites for particle acceleration, i.e., the null surface (red line) and the stagnation surface (green line), are located between the two light cylinders (yellow lines). Contour levels of the charge density (dashed lines) have also been drawn.

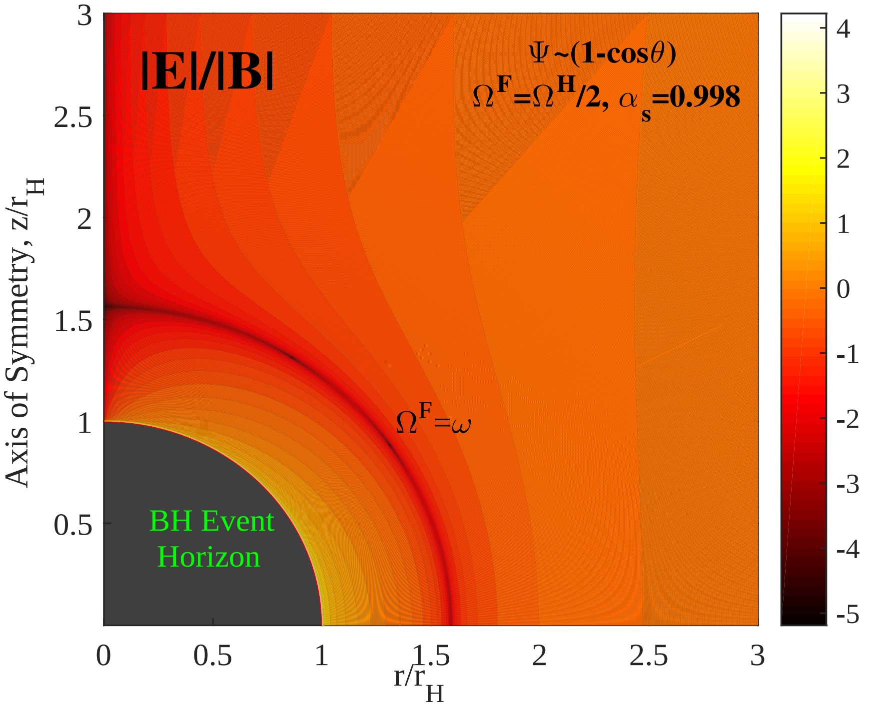

Figure 2.4: Map of the ratio $|\mathbf{E}|/|\mathbf{B}|$ outside the black hole horizon. The vanishing (perpendicular) electric field (see equation 2.40) reveals the location of the null surface in the poloidal plane.

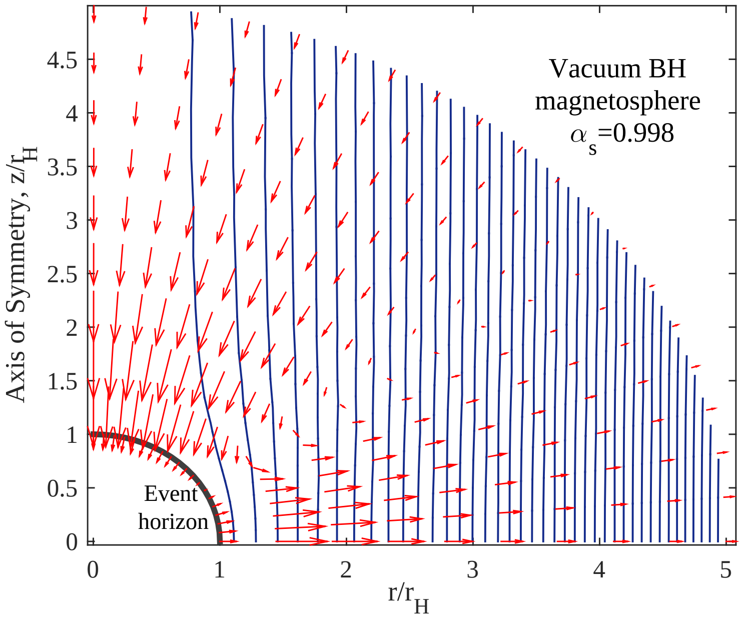

Figure 2.5: Poloidal illustration of a charge-vacuum black hole magnetosphere (Wald, 1974). The direction of the electric field is indicated by the red arrows. Evidently, parallel electric field components are well-established for middle polar angles.

indicate the direction of the electric field induced by the rotation of of the black hole. The lack of a sufficient amount of charges in the region (i.e., $\rho_e \ll \rho_{GJ}$) results in the emergence of extended parallel electric field components.

2.1.4 Current-driven jets

Let us assume an annular tube of magnetic flux $\Delta\Psi$ intersecting the hole. The horizon exerts a net torque on the flux tube (Thorne et al., 1986):

$$-\frac{d\Delta L^H}{dt} = -\frac{1}{c}\left(\mathbf{j}^H \times \mathbf{n}\Delta\Psi\right) = \frac{\left(\Omega^H - \Omega^F\right)}{4\pi c}\widetilde{\omega}^2 B_\perp \Delta\Psi. \qquad (2.60)$$

A *redshifted* power is transmitted outwards by means of this torque. Hence, we can write:

$$\Delta P = -\Omega^F \frac{d\Delta L^H}{dt} = \frac{\Omega^F\left(\Omega^H - \Omega^F\right)}{4\pi c}\widetilde{\omega}^2 B_\perp \Delta\Psi, \qquad (2.61)$$

that is the total power output from the flux tube as derived in Blandford and Znajek (1977). Evidently, it depends critically on the angular velocity Ω^F. A typical value of $\Omega^F = \Omega^H/2$ is required, for efficient energy transmission. This power is usually thought to be responsible for the formation of large-scale outflows/jets observed in radio galaxies.

2.2 Accretion flows

Besides the large scale electromagnetic fields and the presence of charged particles, a black hole magnetosphere may contain neutral gas resulting from the accretion process. As already mentioned, the accreting material, usually concentrated on a disk-like structure, spirals inwards and falls onto the central supermassive black hole due to the outward transportation of angular momentum.

Four solutions are known describing the physical properties and geometry of accretion flows under a variety of astrophysical circumstances. More precisely, the first accretion solution is the *thin disk* model. In this model, the accreting gas forms a geometrically *thin*, optically *thick* disk, which emits a *quasi–blackbody* spectrum. The effective temperature of the radiation ranges

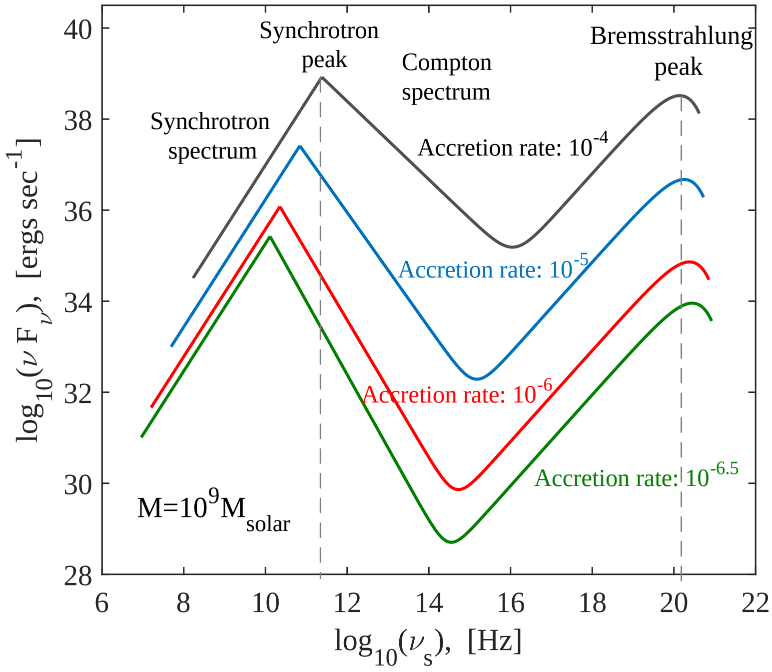

Figure 2.6: ADAF spectra shown for accretion rate $\dot{m} = 10^{-4}$ (black line), $\dot{m} = 10^{-5}$ (blue line), $\dot{m} = 10^{-6}$ (red line) and $\dot{m} = 10^{-6.5}$ (green line), respectively. A supermassive black hole of mass $M = 10^9 M_\odot$ has been considered for the calculation of the spectra.

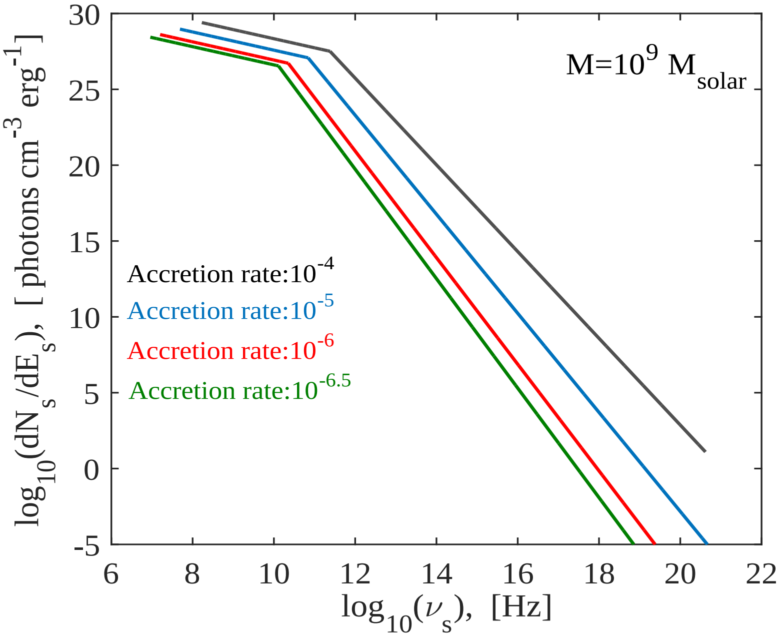

Figure 2.7: Photon number density per unit energy resulting from the ADAF spectrum, i.e., the synchrotron and Compton branches in figure 2.6, and illustrated for accretion rate $\dot{m} = 10^{-4}$ (black line), $\dot{m} = 10^{-5}$ (blue line), $\dot{m} = 10^{-6}$ (red line) and $\dot{m} = 10^{-6.5}$ (green line), respectively. The number density of the ADAF photons is an input (see equations 4.26 and 4.35) in the (1D) steady gap accelerator described in chapter (4).

from $\sim 10^5$ K up to $\sim 10^7$ K, depending on the mass of the black hole and the accretion rate (Shakura and Sunyaev, 1973; Novikov and Thorne, 1973; Lynden-Bell and Pringle, 1974). In the second much hotter solution (Shapiro et al., 1976), the accreting gas consists of a two temperature plasma with the temperature of ions to be greater than the temperature of electrons (i.e., $T_i \sim 10^{11}$ K, while $T_e \sim 10^8 - 10^9$ K). In this approach, the disk is optically *thin* and produces a power law spectrum from X-ray band up to soft γ–ray energies. As it turns out, however, this model is thermally unstable. The other two accretion solutions correspond to the so-called optically *thick* and optically *thin advection dominated accretion flow* (ADAF), respectively. In both models, the viscous energy, produced due to magnetic turbulence, is stored in the gas as thermal energy and, subsequently, is advected onto the central black hole. In such a way, the accretion flow produces radiation in an inefficient mode. The optically *thick* ADAF appears at super–*Eddington* accretion rates (Katz, 1977; Begelman, 1979; Abramowitz et al., 1988), while the optically *thin* one in the opposite limit, namely, at low, sub–*Eddington*, accretion rates (Ichimaru, 1977; Rees et al., 1982; Narayan and Yi, 1994, 1995b,c).

In this doctoral study, we adopt the optically *thin* ADAF spectrum and use it as an input in the "gap accelerator" model described in chapter (4). The ADAF description matches nicely to extragalactic sources (e.g., the radio galaxy M87), whose power is thought to be much lower than the *Eddington* luminosity. As we will show later on (see section 3.1.5), the spectrum of the ADAF constitutes a prerequisite for allowing magnetospheric VHE radiation to escape the source.

Typically, the ADAF spectrum ranges from radio band up to γ–ray energies (i.e., from frequency $\sim 10^9$ Hz to $> 10^{23}$ Hz). The radio to hard X–ray radiation, especially, is considered to be produced by semi–*relativistic*, thermal electrons which belong to the accretion flow (i.e., via the *synchrotron*, inverse *Compton* (IC) and *Bremsstrahlung* processes). More specifically, the spectrum in low energies results from the *synchrotron* cooling of the electron population (see figure 2.6). The *synchrotron* branch (in units of $erg\, s^{-1}\, Hz^{-1}$) is thus proportional to (Mahadevan, 1997):

$$F_\nu^{syn} \propto \left(\frac{M}{M_\odot}\right)^{\frac{6}{5}} \left(\frac{\dot{M}}{\dot{M}_{Edd}}\right)^{\frac{4}{5}} T_e^{\frac{21}{5}} \nu^{\frac{2}{5}}, \tag{2.62}$$

where M and $\dot{M}$ is is the black hole mass and the accretion rate normalized in solar masses and *Eddington* units, respectively, T_e is the temperature of the thermal electrons and ν is the frequency of the emission. Given that the frequency depends on the distance from the center, the peak frequency originates from the vicinity of the black hole. Evidently from figure (2.6), the emission and the peak frequency vary with the accretion rate. In addition, the hot electrons in the ADAF IC upscatter the *synchrotron* soft photons (mostly the photons emitted at the peak frequency), producing harder radiation which extends up to the electrons temperature (i.e., $h\nu_{max} \approx kT_e$; 100 keV). The luminosity of the hard photons at frequency ν_f has the power-law shape (Mahadevan, 1997):

$$F_\nu^{com} = F_p^{syn} \left(\frac{\nu_f}{\nu_p^{syn}} \right)^{-\Gamma} , \tag{2.63}$$

where F_p^{syn} is the emission at the peak frequency ν_p^{syn}. Finally, the significance of each process is associated with the accretion rate. For high accretion rates, the inverse *Compton* branch dominates the spectrum, while for lower ones the *synchrotron* cooling becomes of relevance.

In figure (2.6) above, four ADAF spectra are depicted for different values of the accretion rate, i.e., $\dot{m} = 10^{-4}$ (black line), $\dot{m} = 10^{-5}$ (blue line), $\dot{m} = 10^{-6}$ (red line) and $\dot{m} = 10^{-6.5}$ (green line), respectively. In all cases, a supermassive black hole of mass $M = 10^9 M_\odot$ has been assumed. We note that for the derivation of the spectra, we reproduced the analysis of scaling laws in the paper of Mahadevan (1997). In figure (2.7), we illustrate the photon number density per unit energy (i.e, dN_s/dE_s) as obtained by the predicted ADAF spectra. The break in the curves is due to the transition from the *synchrotron* to the *Compton* spectral branch. The ADAF photon number density is an input in the (1D) steady gap model (see equations 4.26 and 4.35).

2.3 Concluding remarks

In this chapter, the physics of the AGN (i.e., of the *disk-BH-jet* system) was summarized. Specifically, we described the global electrodynamic structure outside a *steady*, *axisymmetric*, *degenerate*, *force-free* and fast rotating black hole. Magnetospheres of this type are thought to extract efficiently the rotational energy of the black hole (due to the presence of a global magnetosperic current), leading to outflow/jet formation. Nevertheless, efficient particle acceleration may occur in magnetospheric regions where *degeneracy* breaks down (i.e., $\mathbf{E} \cdot \mathbf{B} \neq 0$). Such a region, for instance, is either the *null* surface where the charge density changes sign or the *stagnation* surface where the neutral matter separates due to its motion. Magnetospheric particles injected into these thin layers are accelerated in the emerging, unscreened electric field components. Finally, we provided an overview about the spectrum of the *advection dominated accretion flow* (ADAF), which we will use as an input in the (1D) steady gap model discussed in chapter (4).

Chapter 3

Magnetospheric γ-ray radiation in active galaxies

The introductory chapter summarized high and very high energy γ-ray observations (i.e., HE and VHE, respectively) as recorded from *active galactic nuclei* (AGN), whose relativistic outflows/jets are not aligned with the line of sight (i.e., *non-blazar* AGN). In particular, we focused on the TeV flaring activity of two prominent extragalactic sources, namely the radio galaxies M87 and IC310. As it has been already mentioned, the rapidly variable, VHE γ-ray emission from misaligned AGN has been frequently associated with non-thermal processes occurring in the magnetospheres of their supermassive black holes. Chapter two reviewed the basic properties of the near black hole vicinity, that is its magnetosphere and the (inner) accretion environment (e.g., the ADAF).

In the current chapter, we investigate the magnetospheric scenario and derive some first estimates regarding the particle acceleration and the radiative processes in the vicinity of a fast rotating (e.g., $\alpha_s^* \approx 1.0$) supermassive black hole. We specifically aim to explore the adequacy of different gap-type (i.e., unscreened electric field) models to account for the observed characteristics. Based on a phenomenological description of the gap potential, we compute the maximum extractable gap power for different magnetospheric setups and discuss the transparency of the black hole vicinity to VHE γ-ray photons (or otherwise, the possibility of the produced radiation to escape the source). Using the observed rapid variability in order to estimate an upper limit for the gap size (i.e, $h \sim c\Delta t_{obs}$), we discuss the potential that the VHE γ-ray emission detected from active galaxies can be attributed to a magnetospheric origin.

3.1 Magnetospheric emission

Magnetospheric emission models usually rely on efficient “gap-type” particle acceleration (but see, e.g., Rieger and Aharonian, 2008; Osmanov et al., 2017, for alternatives). According to Ohm’s law, $\mathbf{J} = \sigma(\mathbf{E} + \mathbf{V}/c \times \mathbf{B})$, the deficiency of electric charges (i.e., low conductivity σ) within the black hole magnetosphere can directly lead to the formation of (non-*degenerate*) regions with an unscreened parallel electric field component, $\mathbf{E}\cdot\mathbf{B} \neq 0$. Thus, magnetospheric particles moving along the magnetic fields into such charge-empty (“gap”) regions can be strongly accelerated to high energies by these parallel electric field components.

Gaps can in principle occur under several conditions. Extended gaps (with sizes $h \geq r_g$), for example, are known for the vacuum black hole magnetosphere (Wald, 1974). Thinner gaps (with sizes $h < r_g$) can however exist as well and might also be expected in the context of *degenerate*, *force-free* outflows (i.e., in ideal MHD). As an example, we mention the null surface (located close to r_g) formed due to the frame-dragging effect (Beskin et al., 1992; Hirotani and Okamoto, 1998) and the stagnation surface (typically located at a few r_g) which divides MHD inflow from outflow regions (e.g., Globus and Levinson, 2014; Broderick and Tchekhovskoy, 2015). In these places, continuous charge replenishment (e.g., by particle creation or diffusion) has to occur in order to sustain the required *Goldreich-Julian* charge density:

$$\rho_{GJ} = -e\, n_{GJ} \simeq -\frac{\Omega^F B_\perp}{2\pi c}. \tag{3.1}$$

Throughout this chapter, we do not consider a specific gap position, but adopt a more phenomenological description. We assume that primary particles can be injected into the magnetosphere by processes in the accretion environment (e.g., via annihilation of MeV photons emitted by a hot accretion flow). As has been shown elsewhere, the injected seed particle density is not sufficient for complete screening (i.e., $|\rho_\pm|/e < |\rho_{GJ}|/e$) below a certain accretion rate $\dot{M}$ (Levinson and Rieger, 2011). This implies that gaps can appear if the accretion flow is *advection-dominated* (ADAF).

3.1.1 The vicinity of the black hole

Let us consider a rotating black hole of spin parameter $a_s^* \simeq 1$ and mass $M = M_9 \times 10^9 M_\odot$ onto which gas accretion occurs. The central black hole is fed by the accretion flow at a rate $\dot{M} = \dot{m}\,\dot{M}_{Edd}$ expressed in *Eddington* units, where:

$$\dot{M}_{Edd} = \frac{l_{Edd}}{\eta_{cv}\,c^2} \approx 1.4 \times 10^{27} M_9 \qquad g\,s^{-1}, \tag{3.2}$$

$$l_{Edd} = 1.3 \times 10^{47} M_9 \qquad erg\,s^{-1}, \tag{3.3}$$

is the fiducial *Eddington* luminosity and $\eta_{cv} \sim 0.1$ the canonical conversion efficiency. This corresponds to a reference limit on the accretion luminosity:

$$l_{disk} = \eta_{cv}\,\dot{M}c^2 = \dot{m}\,l_{Edd}, \tag{3.4}$$

that is comparable to the one for a steady, standard (geometrically thin, optically thick) disk. As it is shown later on, however, a radiatively inefficient accretion flow is a prerequisite for the escape and thus observability of magnetospheric VHE γ-rays. For an optically-thin advection-dominated accretion flow (ADAF) in which most of the viscously dissipated energy is advected with the flow, cooling is almost inefficient, resulting in a much reduced luminosity:

$$\frac{l_{ADAF}}{l_{disk}} \propto \dot{m} \ll 1. \tag{3.5}$$

ADAFs can only exists below a critical accretion rate, usually requiring $\dot{m}_c \simeq 0.4\alpha_v^2 \lesssim 0.015$ (with $\alpha_v \lesssim 0.2$) (Mahadevan, 1997; Narayan et al., 1998), though more restrictive conditions ($\dot{m}_c \sim 0.003$) have been reported as well (e.g., Beckert and Duschl, 2002; Yuan and Narayan, 2014).

We can approximate the characteristic disk magnetic field strength by assuming that the equipartition magnetic pressure is half the gas pressure, namely:

$$\frac{B^2}{8\pi} = \frac{1}{2}\,\rho_i\,c_s^2, \tag{3.6}$$

where $c_s \simeq c\,(r_s/r)^{1/2}/\sqrt{3}$ is the sound speed. Though current simulations indicate some deviation from equipartition (i.e., $\beta_{ADAF} > 0.5$; see e.g, Yuan and Narayan, 2014), this will provide a useful upper limit. With $4\pi r^2 \rho_i v_r = \dot{M}$ and radial inflow speed:

$$v_r \simeq 0.5\,\alpha_v\,v_f = \frac{1}{\sqrt{8}}\,\alpha_v\,\left(\frac{r_s}{r}\right)^{1/2} c, \tag{3.7}$$

where α_v is the viscosity coefficient, the disk magnetic field becomes:

$$B_d \simeq 2.1 \times 10^4 \alpha_v^{-1/2} M_9^{-1/2} \dot{m}^{1/2} \left(\frac{r_s}{r}\right)^{5/4} \qquad G, \tag{3.8}$$

which agrees well with previously reported ADAF results (e.g., Mahadevan, 1997; Narayan et al., 1998; Yi, 1999). Evaluating at characteristic radius $r = 1.5\,r_g$ (Meier, 2001) and using $\alpha_v = 0.1$ as reference value (e.g., King et al., 2007; Yuan and Narayan, 2014), the inner disk field could thus reach strengths of:

$$B_d \approx 10^5 \dot{m}^{1/2} M_9^{-1/2} \quad \text{G}. \tag{3.9}$$

Given that for ADAFs the disk scale height is about $H \sim r$, the strength of the poloidal magnetic field threading the black hole $B \simeq B_d \times (H/r)^n$, $n \sim 1$ (Livio et al., 1999; Meier, 2001), is expected to be comparable in magnitude. In fact, taking the field-enhancing shear in the *Kerr* metric into account, the field threading the black hole may be a factor of about 2.3 larger (Meier, 2001), i.e., $B_{d,h} \simeq 2.3 B_d$, which would bring it close to the value inferred from GRMHD jet simulations in the context of magnetically arrested disks (e.g., Tchekhovskoy et al., 2011; Tchekhovskoy and McKinney, 2012; Yuan and Narayan, 2014).

The emission spectrum of an ADAF is produced by *synchrotron*, inverse *Compton* and *bremsstrahlung* radiation of relativistic thermal electrons, and typically extends from radio frequencies up to hard X-rays (Narayan and Yi, 1995a). Like any disk emission, this radiation constitutes a potential target for any magnetospheric VHE γ-rays. For sufficiently small accretion rate $\dot{m}$ the peak energy E_s and the luminosity l_s of the soft photon field become (see chapter 2 and Mahadevan, 1997):

$$E_s \approx 0.2\,\dot{m}^{3/4} M_9^{-1/2} T_{e,9}^2 \quad \mathrm{eV}, \tag{3.10}$$

$$l_s \approx 5 \times 10^{43}\,\dot{m}^{9/4} M_9^{1/2} T_{e,9}^7 \quad \mathrm{erg\,s^{-1}}, \tag{3.11}$$

where $T_{e,9} = T_e/10^9 \approx 5$ is the characteristic electron temperature which depends weakly on the accretion rate $\dot{m}$ (Mahadevan, 1997) and the radial distance r at the inner edge of the ADAF (Narayan and Yi, 1995a; Manmoto et al., 1997). For simplicity, we thus fix the temperature to $T_{e,9} = 5$ in all our following calculations in this chapter. Correspondingly, the soft photon number density can be expressed as:

$$n_s \simeq \frac{l_s}{2\pi\, r_s^2\, c\, E_s} \approx 4 \times 10^{19} \dot{m}^{3/2} M_9^{-1} \quad \mathrm{cm^{-3}}. \tag{3.12}$$

Accreting black hole systems are capable of ejecting powerful jets. On average the maximum power l_{jet} of these jets should be comparable to the available accretion power $\dot{M}c^2$ (e.g., Ghisellini et al., 2014). This should also hold for *Blandford-Znajek* jets (i.e., ergospheric-driven) as the magnetic flux carried onto the black hole is proportional to $\dot{M}$ (see equation 3.8). General relativistic MHD simulations in fact show that the jet power does not exceeds $\dot{M}c^2$ by more than a factor of ~ 3 (e.g., Tchekhovskoy et al., 2011). Hence, on phenomenological grounds one could write:

$$l_{jet} = \eta_j\, \dot{M}c^2 = \frac{\eta_j}{\eta_{cv}}\, l_{disk} = \left(\frac{\eta_j}{\eta_{cv}}\right) \dot{m}\, l_{Edd}, \tag{3.13}$$

with $\eta_j \lesssim 3$. This could be related to the electromagnetic extraction of rotational energy of the supermassive black hole (Thorne et al., 1986). In the case of a rotating, *force-free* black hole magnetosphere (i.e, efficient energy

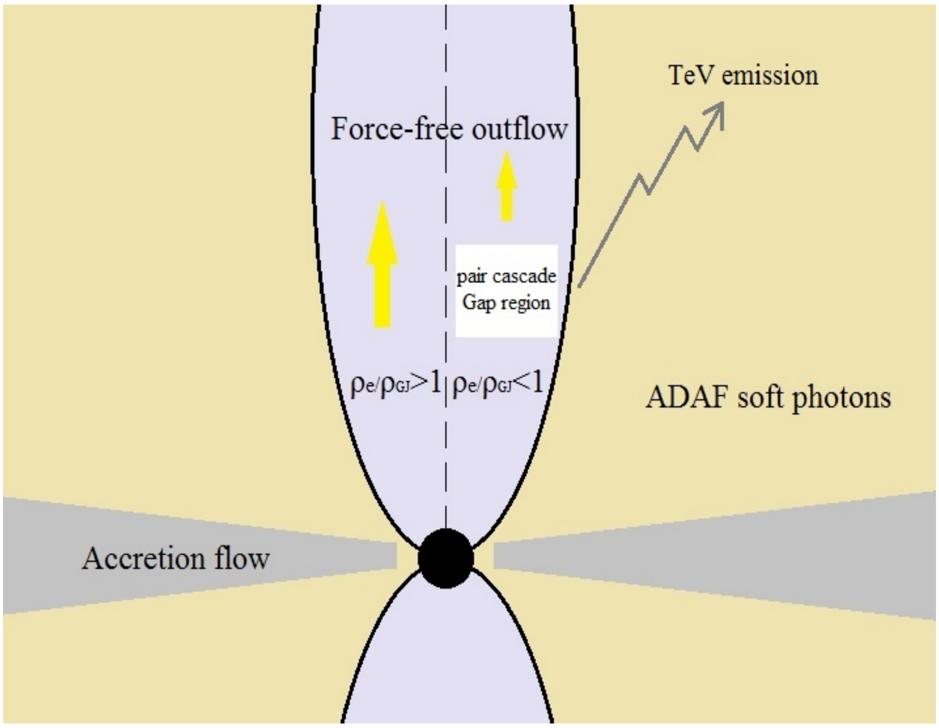

Figure 3.1: Schematic representation of the physical processes occurring in the vicinity of the central black hole. In the case of insufficient feeding of the magnetosphere with charges (i.e., $\rho_e/\rho_{GJ} < 1$) gap regions are formed. Seed particles are sufficiently accelerated in these gaps, producing γ-ray emission by e.g., IC-upscattering of ADAF soft photons. The photon-pair cascade, that is triggered in the gap zone, reinstates the charge density, leading to force-freeness and jet initiation. The TeV flaring activity then occurs as manifestation of a global operation.

extraction) the maximum *Blandford-Znajek* (BZ) jet power is given by:

$$\begin{aligned} l_{BZ} &= \Omega^F(\Omega^H - \Omega^F) B_\perp^2 \frac{r_H^4}{c} = (\Omega^F)^2 B_\perp^2 \frac{r_H^4}{c} = \\ &= \frac{1}{16} a_s^{*2} c\, r_H^2 B_\perp^2 \approx 2 \times 10^{48}\, \dot{m}\, M_9 \left(\frac{B_\perp}{B_{d,h}}\right)^2 \quad \mathrm{erg\,s^{-1}}, \end{aligned} \tag{3.14}$$

where $\Omega^H = a_s^* c/2r_H$ is the black hole angular velocity, $\Omega^F = \Omega^H/2$ is the angular velocity of the field lines in the case of efficient extraction, and $B_\perp \simeq B_{d,h} \simeq 2.3 B_d$ is the strength of the normal magnetic field component threading the event horizon $r_H = r_g(1 + \sqrt{1 - a_s^{*2}}) \sim r_g$ (for $a_s^* \sim 1$). This concurs with the considerations above, $l_{BZ} = \eta_j \dot{M} c^2 \lesssim 4 \times 10^{48} \dot{m} M_9 \; erg/s$, and suggests that the BZ jet power provides a useful measure for $\dot{M}$ and vice versa.

In general, magnetospheric VHE emission occurs as a sub-product of an universal operation (see the sketch in figure 3.1 for illustration). If complete screening in the magnetosphere is not achieved (i.e., $\mathbf{E}\cdot\mathbf{B} \neq 0$), then particles, accelerated within the gaps, are likely to emit multiple VHE radiation (e.g., Levinson, 2000; Rieger, 2011). Beyond an energy threshold, the VHE photons are absorbed by the ambient soft photon field producing secondary pairs. These will again be accelerated and their radiation will be accompanied by further absorption/pair creation. In such a way, a photon-electron cascade is triggered, that guarantees a charge multiplicity such that *force-freeness* (i.e., $\rho_e = \rho_{GJ}$) and MHD jet launching is ensured. Below the energy threshold, VHE photons can escape the black hole environment. Variable VHE emission observed from under-luminous AGN could thus signal the onset of relativistic jet formation (Levinson and Rieger, 2011).

3.1.2 The electric field and potential of gaps

As we have stated above, a quasi-steady magnetospheric gap can be formed in an under-dense environment (i.e., $|\rho_e|/e \leq |\rho_{GJ}|/e$). In the following, we consider that the gap region has quasi-spherical shape and it is located at radial distance R_{gap} close to r_g (e.g., see chapter 2). We assume, in addition, that it possesses a size or extent denoted by h. The voltage difference or gap potential then scales with the gap size depending on how the fields and boundaries are treated and different descriptions are thus encountered. Given that the gaps can be very thin ($h \ll r_g$), this could lead to substantial differences.

Heuristic constraint

A heuristic constraint might be obtained from the global electric field of a *force-free* magnetosphere, that is $\mathbf{E} = -\mathbf{V}/c \times \mathbf{B}$ under the assumption of high conductivity ($\sigma \to \infty$). Although the electric vector changes in the gap and only some part becomes parallel to the magnetic field lines, one may assume that its strength remains roughly comparable with the *force-free* field. Hence, in order of magnitude, one could write for the electric field of the gap that:

$$E_{gap} \approx \frac{V}{c} B_{gap} \approx \left(\frac{\Omega^F R_{gap}}{c} \right) B_{gap}, \tag{3.15}$$

approximating $\sin \theta_b$ by unity[1]. We note that this expression in principle assumes that charge sheets or charge injection occurs just outside the gap boundaries (see equation 3.18 below). As this seems rather unexpected, the inferred E_{gap} should be considered as providing a clear upper limit for possible realisations.

Noting that $E_{gap} \sim \Delta\mathcal{V}_{gap}/h$, where $\Delta\mathcal{V}_{gap}$ denotes the voltage drop, and using that $\Omega^F \approx \Omega^H/2$ and $\Omega^H = c/2r_g$, one would obtain:

$$\Delta\mathcal{V}_{gap} \approx \frac{1}{4} B_{gap} R_{gap} \left(\frac{h}{r_g} \right), \tag{3.16}$$

namely that, the voltage drop scales linearly with h (e.g., $\Delta\mathcal{V}_{gap} \propto h$; in this context see also Aharonian et al., 2017). Equation (3.16) then represents a fiducial upper limit for the voltage drop of the magnetospheric gap that can be tapped for the acceleration of particles. For $B_{gap} \simeq B_{d,h} \simeq 2.3 B_d$ (see equation 3.9) and $R_{gap} \sim r_g$ this would give:

$$\Delta\mathcal{V}_{gap} \approx 2.5 \times 10^{21} \dot{m}^{1/2} M_9^{1/2} \left(\frac{h}{r_g} \right) \quad \text{Volts}, \tag{3.17}$$

noting that 1 Statvolt=300 Volts.

Physical estimates

Different scaling laws of the voltage difference with the gap size h are in fact present in the literature. The apparent discrepancy can be related to different assumptions regarding the expected gap boundary conditions (Beskin, 2009). In its simplest (one-dimensional, non-relativistic) form the electric field of the gap along the radial dimension s in the presence of a non-zero charge density ρ_e may be determined from *Gauss's* law:

---

[1] The angle θ_b represents the angle between rotational axis and magnetic field direction.

$$\frac{dE_{||}}{ds} = 4\pi(\rho_e - \rho_{GJ}), \tag{3.18}$$

and the corresponding electrostatic potential from:

$$\frac{d\Phi_e}{ds} = -E_{||}\,, \tag{3.19}$$

so that the voltage drop becomes $\Delta\mathcal{V}_{gap} = \Phi_e(s = h) - \Phi_e(s = 0)$.

In order to specify the electric field and illustrate the gap physics, we need to choose appropriate conditions for its interior and boundaries. In the followings, we distinguish two limiting cases, namely a highly (case *i*) and a weakly (case *ii*) under-dense gap region:

(i) Accordingly, this regime can be characterized by $|\rho_e|/e \ll |\rho_{GJ}|/e$ and $E_{||}(s = 0) \neq 0$, with the developing pair cascade ensuring that the field gets screened at scale heigh h, i.e., $E_{||}(s = h) = 0$. Hence, equation (3.18) implies that:

$$\frac{dE_{||}}{ds} \approx -4\pi\rho_{GJ}, \tag{3.20}$$

and subsequently:

$$E_{||} \approx -4\pi\rho_{GJ}\, s + const., \tag{3.21}$$

neglecting possible variations in function ρ_{GJ}. Using that $E_{||}(s = h) = 0$ one can write:

$$E_{||}(s) = 4\pi\rho_{GJ}(h - s) = 4\pi\rho_{GJ} h\,\frac{(h - s)}{h} = E_0\frac{h - s}{h}\,, \tag{3.22}$$

with maximum electric field value $E_0 = E_{||}(s = 0) = 4\pi\rho_{GJ}\, h$. The voltage or potential drop then becomes:

$$\begin{aligned}\Delta\mathcal{V}_{gap} &= \int_0^h E_{||}(s)ds = -4\pi\rho_{GJ}\,\frac{h^2}{2} = \\ &= -2\pi\rho_{GJ}\,h^2 = -2\pi\rho_{GJ}\,r_H^2\left(\frac{h}{r_H}\right)^2 = \Phi_0\left(\frac{h}{r_H}\right)^2,\end{aligned} \tag{3.23}$$

where:

$$\Phi_0 \equiv -2\pi\rho_{GJ}r_H^2 \simeq \Omega^F r_H^2\frac{B_\perp}{c} = \Omega^H r_H^2\frac{B_\perp}{2c}, \tag{3.24}$$

with $\rho_{GJ} \simeq -\Omega^F B_\perp/(2\pi c)$, resulting in a scaling $\Delta\mathcal{V}_{gap} \propto h^2$ that is different to the one in formula (3.16). Such a scaling, $\propto h^2$, figures most promising in the gap context, (e.g., Blandford and Znajek, 1977; Levinson, 2000; Levinson and Rieger, 2011). We note that in this case some continuous charge injection would be needed to keep the gap quasi-steady lest it to become intermittent.

(ii) A different dependence is, however, obtained for the second case. In this case, we have that $\rho_e \sim \rho_{GJ}$ and hence, $E_{||}(s=0) \approx 0$, with the cascade again ensuring that $E_{||}(s=h) = 0$. Note that even if initially $\rho_e = \rho_{GJ}$ somewhere, deviations are expected as $\rho_{GJ} \propto \cos\theta_b$ varies along field lines. For non-trivial solutions of $E_{||}$ the chosen boundary condition can only be satisfied if $dE_{||}/ds$ is non-zero at the boundaries (i.e., if the charge density does not fully coincide with the *Goldreich-Julian* value there) and, furthermore, if the electric field takes on an extremal value at $s = h/2$ (i.e., $dE_{||}/ds = 0$ at $s = h/2$), which by *Gauss's* law implies $\rho(h/2) = \rho_{GJ}(h/2)$. We can thus *Taylor*-expand the charge-density term $(\rho_e - \rho_{GJ}) \equiv \rho_{eff}$ around $s = h/2$ to give:

$$\begin{aligned}\rho_{eff}(s) &= \rho_{eff}\left(\frac{h}{2}\right) + \left.\frac{d\rho_{eff}}{ds}\right|_{\left(\frac{h}{2}\right)}\left(s-\frac{h}{2}\right) \\ &= \left.\frac{d\rho_{eff}}{ds}\right|_{\left(\frac{h}{2}\right)}\left(s-\frac{h}{2}\right) \equiv \rho'_{eff}\left(\frac{h}{2}\right)\left(s-\frac{h}{2}\right),\end{aligned} \tag{3.25}$$

noting that $\rho_{eff}(h/2) = 0$. Therefore, the equation $dE_{||}/ds = 4\pi\rho'_{eff}\,(s-h/2)$ implies:

$$E_{||}(s) = 4\pi\rho'_{eff}\left(\frac{1}{2}s^2 - \frac{h\,s}{2}\right) = -2\pi\rho'_{eff}r_H^2\,\frac{s\,(h-s)}{r_H^2}\,. \tag{3.26}$$

In the case of the null surface we approximately have (Hirotani et al., 2016):

$$\rho'_{eff}(h/2) \simeq -\frac{\rho_{GJ}}{r_H} \simeq \frac{\Omega^F B_\perp}{(2\pi c r_H)}, \tag{3.27}$$

so that, the voltage drop becomes:

$$\begin{aligned}\Delta\mathcal{V}_{gap} &= \int_0^h E_{||}(s)ds = 4\pi\rho'_{eff}\left[\frac{1}{6}s^3 - \frac{1}{4}hs^2\right]_0^h = \\ &= -4\pi\rho'_{eff}\frac{h^3}{12} = -\frac{1}{3}\pi\rho'_{eff}r_H^3\left(\frac{h}{r_H}\right)^3\,,\end{aligned} \tag{3.28}$$

where a scaling $\propto h^3$, that is different from those previously discussed, is now obtained. An analogous expression has been recently employed for studying the luminosity output of gaps in the AGN context (Hirotani et al., 2016). We emphasize here that the strength of the second case lies in the fact that it seemingly provides a transparent self-consistent realisation of a quasi-steady gap.

To account for these differences and facilitate comparison, we employ a general parametric expression in the following:

$$\begin{aligned}\Delta\mathcal{V}_{gap} &= \frac{1}{c}\,\eta_c\,\Omega^F r_H^2 B_\perp\left(\frac{h}{r_H}\right)^\nu \\ &\approx 2.5\times10^{21}\eta_c\,\dot{m}^{1/2}M_9^{1/2}\left(\frac{h}{r_g}\right)^\nu\quad\text{Volts}\,,\end{aligned} \tag{3.29}$$

where the respective sets of numerical parameters η_c and ν are listed in Table (3.1). We also note that $B_{gap} \simeq B_{d,h}$ has been assumed for the second expression on the right hand side.

Table 3.1: Gap voltage and luminosity parameters. Parameters η_c and ν are for the voltage drop scaling $\Delta\mathcal{V}_{gap} \propto \eta_c\,(h/r_H)^\nu$ as defined in equation (3.29) and the corresponding maximum luminosity output $l_{gap} \propto l_{BZ}\,(h/r_H)^\beta$ following equation (3.35). The first column specifies the power dependence on h, the second and third the corresponding values for η and β respectively, and the fourth gives exemplary references, with (1) = current work (reference limit), (2) Blandford and Znajek (1977), (3) Levinson (2000), (4) Levinson and Rieger (2011), (5) Hirotani et al. (2016).

Exponent ν	*Coefficient* η_c	*Coefficient* β	*Reference*
1	1	1	(1)
2	1	2	(2) – (4)
3	1/6	4	(5)

3.1.3 Particle acceleration and VHE γ-ray emission

A charged particle, injected into the magnetospheric gap, will be strongly accelerated along the parallel electric field component. Let us consider an electron of energy $E_e = \gamma_e m_e c^2$, experiencing the potential drop of equation (3.29). Its rate of energy gain per unit time would be $d(\gamma_e m_e c^2)/dt = (c/r_g) e \Delta\mathcal{V}_{gap}\,(h/r_g)^{-1}$, where γ_e is the *Lorentz* factor of the electron, m_e is its rest mass and c is the speed of light. This estimate implies a characteristic acceleration time scale, $\tau_{acc} = E_e/(dE_e/dt)$, given by:

$$\tau_{acc}(\gamma_e) = 10^{-12}\,\frac{\dot{m}^{-1/2}}{\eta_c} M_9^{1/2} \gamma_e \left(\frac{h}{r_g}\right)^{1-\nu} \quad \mathrm{s}\,. \tag{3.30}$$

Beside acceleration and energy gain, the electron will also experience losses during its motion within the gap region due to the presence of large scale ordered magnetic field and inverse *Compton* scattering (Rieger, 2011). Assuming that the curvature radius is roughly equal to the gravitational one (i.e., $R_{cur} \approx r_g$), the cooling time scale due to *curvature* radiation becomes:

$$\tau_{cur}(\gamma_e) \approx 4 \times 10^{30}\, M_9^2\, \gamma_e^{-3} \quad \mathrm{s}. \tag{3.31}$$

The whole magnetosphere as well as the gap accelerator are embedded in the ambient soft photon field of the disk (see subsection 3.1.1). Electrons undergoing acceleration along the field will thus also *Compton* up-scatter these soft photons to multiple VHE energies where the occurrence of $\gamma\gamma$-absorption can lead to the formation of a pair cascade (Levinson and Rieger, 2011). To explore the characteristic inverse *Compton* (IC) cooling time scale we approximate the soft photon field as isotropic and quasi-monoenergetic with E_s and l_s given by relations (3.10) and (3.11). The IC electron cooling time scale then follows (Aharonian and Atoyan, 1981):

$$\tau_{ic}(\gamma_e) = \frac{b^2}{3\sigma_T c n_s}\left[\left(6+\frac{b}{2}+\frac{6}{b}\right)\ln(1+b) - \ln^2(1+b) - \right.$$
$$\left. -2\,\mathrm{Li}\left(\frac{1}{1+b}\right) - \frac{\frac{11}{12}b^3+8b^2+13b+6}{(1+b)^2}\right]^{-1} \mathrm{s}, \quad (3.32)$$

where $\mathrm{Li}(x) \equiv -\int_x^1 \ln y/(1-y)dy$ and $b \equiv b(\gamma_e) = 4\gamma_e E_s/(m_e c^2) \approx 3\times 10^{-5}\dot{m}^{3/4}\gamma_e M_9^{-1/2}$ is a non-dimensional quantity.

An electron will quickly reach its terminal *Lorentz* factor at which energy gain is balanced by radiative losses. Using appropriate values of $\dot{m}$, M_9, h, ν and equating the acceleration time with the cooling ones (i.e., $\tau_{acc} = \tau_{cur}$ or/and $\tau_{acc} = \tau_{ic}$), the maximum electron *Lorentz* factor γ_{max} can be explored. It is worth emphasising that both radiation processes will take place, though the shortest one will impose the relevant constraint. Hence we may write $\gamma_{max} = \min(\gamma_{cur}, \gamma_{ic})$, where the maximum particle *Lorentz* factor due to curvature is given by:

$$\gamma_{cur} \approx 4.5\times 10^{10}\eta_c^{1/4}\dot{m}^{1/8}M_9^{3/8}\left(\frac{h}{r_g}\right)^{\frac{\nu-1}{4}}. \quad (3.33)$$

In figures (3.2) and (3.3), the relevant time scales as a function of the electron *Lorentz* factor (e.g., see equations 3.30, 3.31 and 3.32) are shown for a characteristic set of AGN parameters (i.e., $M_9 = 5.0$ and $\dot{m} = 10^{-4}$). The establishment of a magnetospheric gap with size $h/r_g = 0.01$ and $h/r_g = 0.5$ has been assumed for figure (3.2) and (3.3), respectively. For the considered choices, IC losses are weakened by *Klein-Nishina* effects. For the gap size,

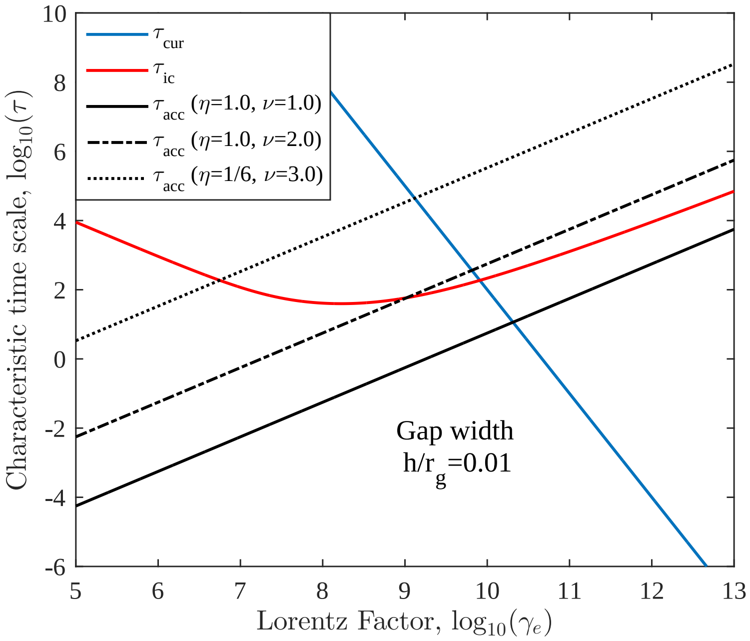

Figure 3.2: Characteristic time scales as a function of Lorentz factor γ_e for $M_9 = 5$, $\dot{m} = 10^{-4}$, $h/r_g = 0.01$. The solid blue line and red curve represent the time scales for curvature and inverse Compton losses, respectively. The (rising) black lines represent the acceleration time scales for the different gap potentials. The intersection points provide a measure of the achievable maximum energies.

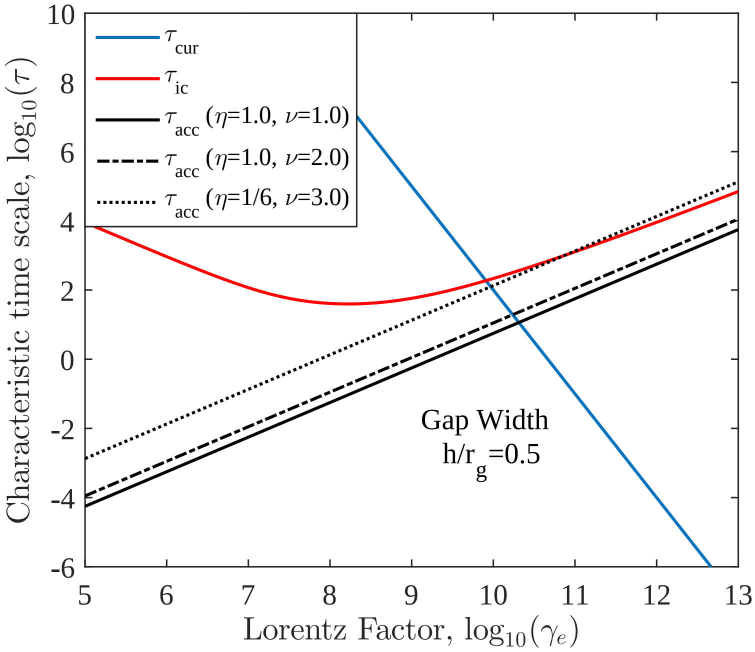

Figure 3.3: Characteristic time scales as a function of Lorentz factor γ_e for $M_9 = 5$, $\dot{m} = 10^{-4}$, $h/r_g = 0.5$. The solid blue line and red curve represent the time scales for curvature and inverse Compton losses, respectively. The (rising) black lines represent the acceleration time scales for the different gap potentials. The intersection points provide a measure of the achievable maximum energies.

$h/r_g = 0.5$, the maximum particle energies are essentially constrained by *curvature* losses. However, for smaller gap sizes, $h/r_g < 0.5$, (e.g., see figure 3.2), IC losses will start to become of relevance and reduce achievable electron energies, foremost for $\nu = 3$ (i.e., $\beta = 4$). Figure (3.3) suggests that for extended gaps (i.e., $h \sim r_g$) maximum Lorentz factors of $\gamma_{max} \sim 10^{10}$ could in principle be reached. This in turn implies that IC photons could reach multi-TeV energies, $E_{ic} = \gamma_e m_e c^2 \leq 10^4$ TeV, while curvature emission could extend into the TeV regime, $E_{cur} = 3c\hbar\,\gamma_{max}^3/(2R_{cur}) \sim 0.2\,(\gamma_{max}/10^{10})^3/M_9$ TeV. Magnetospheric gaps in AGN can thus be putative VHE emitting sites. If proton injection into the gap would occur (e.g., via diffusion), with *Lorentz* factors limited by curvature losses, it is in principle conceivable that photomeson (pγ) production in the soft photon field of disk might contribute to this.

3.1.4 The gap luminosity

The radiative output of the gap depends on the number density of particles, $n_\pm = |\rho_\pm|/e$, which undergo acceleration and radiation in it. Gap closure will occur once the effective charge density approaches the critical one, $|\rho_c| = e\,n_c$. This allows for an estimate of the maximum achievable VHE gap power, l_{gap}, given a voltage or potential drop $\Delta\mathcal{V}_{gap}$, namely:

$$l_{gap} \simeq n_c V_{gap} \frac{dE_e}{dt} \simeq -\frac{|\rho_c|}{e}(2\pi r_H^2 h)\frac{e\,\Delta\mathcal{V}_{gap}\,c}{h}\,, \tag{3.34}$$

where we approximate the relevant gap volume, V_{gap}, by a half-sphere of gap height h. The appropriate values of ρ_c or n_c to be employed in equation (3.34) are dependent on the assumed gap set-up. For the heuristic and under-dense cases (i.e., $\nu = 1$ and $\nu = 2$ as delineated above, see formula 3.18), the critical value is typically comparable to the *Goldreich-Julian* density, i.e., $\rho_c = \rho_{GJ} \simeq -\Omega^F B_\perp/(2\pi c) = -\Omega^H B_\perp/(4\pi c)$. In the weakly under-dense case (i.e., $\nu = 3$), however, the appropriate value based on equation (3.27) instead is $\rho_c \simeq \rho'_{eff}\,h \simeq \rho_{GJ}\,h/r_H$ (e.g., Hirotani et al., 2016). This results in a scaling for the gap power, $l_{gap} \propto h^4$, with power index increased by one compared to the respective potential drop (see equation 3.27), while the index remains the same for the former cases.

Since now $l_{gap} \propto (\Omega^F)^2 B_\perp^2$, we can also express the respective gap luminosity in terms of the *Blandford-Znajek* jet power (see formula 3.14). Therefore, we can write:

$$l_{gap} = \eta_c \, l_{BZ} \left(\frac{h}{r_H}\right)^{\beta} \lesssim l_{BZ} \,, \tag{3.35}$$

where the respective sets of parameters are listed in Table (3.1) above. For gap sizes $h \ll r_g$ then, the expected VHE output is much smaller than the jet power.

3.1.5 The accretion environment

Independent of the preferred scenario for gap formation, to avoid external $\gamma\gamma$-absorption of the VHE photons produced into the gap and facilitate their escape from the vicinity of a supermassive black hole, magnetospheric models generally require an under-luminous or radiatively inefficient (RIAF) inner disk environment. Let us suppose, nevertheless, that the disk would be of an (un-truncated) standard (geometrically thin, optically thick) type, for which the effective surface temperature obeys (Frank et al., 2002):

$$\begin{aligned} T_{\rm eff}(r) &= \left[\frac{3GM\dot{M}}{8\pi\sigma r^3}\left(1-\sqrt{\frac{r_{\rm in}}{r}}\right)\right]^{1/4} = \qquad (3.36)\\ &= 3.5\times 10^5 \, \dot{m}^{1/4} M_9^{-1/4} \left(\frac{r_s}{r}\right)^{3/4} \left(1-\sqrt{\frac{r_{\rm in}}{r}}\right)^{1/4} {\rm K}\,, \end{aligned}$$

with σ the *Stefan-Boltzmann* constant. This profile peaks at a temperature:

$$T_p \simeq \frac{1}{2}\left(\frac{3\,GM\dot{M}}{8\pi\sigma r^3}\right)^{1/4} , \tag{3.37}$$

close to the inner disk radius, $r \sim r_{in} \sim r_s$, and exhibits the canonical, $r^{-3/4}$, dependence. For characteristic AGN parameters, the peak of the thermal disk emission, carrying a power of order $l_{disk} = \dot{m} l_{Edd}$, would then be occurring at eV energies, i.e., $\epsilon_p \simeq 2.8kT_p \simeq 40\ \dot{m}^{1/4} M_9^{-1/4}$ eV. This thermal disk radiation field would then provide an ideal target for the absorption of VHE photons producing pairs via $\gamma_s\,\gamma_{TeV} \rightarrow e^+\,e^-$. VHE photons of energy E_γ, in fact, interact most efficiently with ambient soft photons of energy (Rieger, 2011):

$$E_d \simeq 1\,\left(\frac{1\ \mathrm{TeV}}{E_\gamma}\right)\ \mathrm{eV}\,. \tag{3.38}$$

The corresponding optical depth would be approximately $\tau_{\gamma\gamma} \sim \sigma_{\gamma\gamma} n_d\, r$, where we set that $\sigma_{\gamma\gamma} \simeq 0.2\sigma_\tau$ and $n_d \sim l_d/4\pi r^2 c E_d$. Note also that σ_τ denotes the *Thomson* cross section. Approximating $l_d \simeq l_{disk} \times (E_d/E_p)^3$ (*Rayleigh-Jeans* limit) and $r \sim r_s$, we obtain:

$$\tau_{\gamma\gamma} \sim 10^3\,\dot{m}^{1/4} M_9^{3/4} \gg 1\,, \tag{3.39}$$

for VHE photons, i.e., the optical depth greatly exceeds unity for conventional AGN parameters (cf. also Zhang and Cheng, 1997).

Hence, even if the black hole magnetosphere would produce VHE radiation, most of it is expected to become absorbed unless the disk would be of a radiatively inefficient (RIAF/ADAF) type where $l_d = l_{ADAF} \ll l_{disk}$ and the dominant part is emitted at energies much below 1 eV (see equation 3.10). Very low accretion rates, or conservatively, the presence of a RIAF or ADAF thus becomes a necessary (yet not in itself sufficient) condition for the detectability of magnetospheric VHE emission in AGN. An ADAF-type (optically-thin) accretion flow with $H \sim r$ could also ensure the necessary poloidal magnetic field strength for efficient BZ power extraction (e.g., Livio et al., 1999; Meier, 2001).

3.2 Astrophysical application

As already mentioned, gap-driven magnetospheric emission processes have been suggested as a potential generator of the highly variable VHE radiation seen from misaligned, non-*blazar* AGN (Neronov and Aharonian, 2007; Levinson and Rieger, 2011; Aleksic et al., 2014a; Vincent, 2015; Ptitsyna and Neronov, 2016; Hirotani et al., 2016). In the current section, we seek to assess the potential of such scenarios on quite general grounds, putting the relevant variability, transparency and power constraints in context.

Firstly, by means of causality, we expect that VHE flux variability on short time-scales, Δt_{obs}, will limit the size of the putative gap to $h \lesssim c\Delta t_{obs}$. In general, we can assume that the gap size h does not exceed r_g if efficient pair cascade formation occurs. The VHE flux variability thus imposes a limit on the extractable gap power as $l_{gap} \propto l_{BZ}(h/r_g)^{\beta}$, (see equation 3.35).

In order to ensure transparency, on the other hand, namely the magnetospheric VHE γ-rays to become observable, an advection dominated accretion flow (ADAF) is required (see subsection 3.1.5). This requires the accretion rate to satisfy $\dot{m} \lesssim \dot{m}_c$ and in turn leads to a constraint on the average jet power $l_{jet} \sim l_{BZ} \propto \dot{m}$, (see equation 3.14). Though a variety of values for $\dot{m}_c$ have been reported, $\dot{m}_c \sim 0.01$ appears to be a representative upper limit (Yuan and Narayan, 2014). Following this line of reasoning and assuming a rapidly spinning black hole, the constraints on the gap size and accretion rate thus translate into a characteristic upper-limit on the extractable VHE gap power, which is:

$$l_{gap}^{VHE} \lesssim 2 \times 10^{46} \eta_c \left(\frac{\dot{m}_c}{0.01}\right) \left(\frac{M}{10^9 M_{\odot}}\right) \left(\frac{c\Delta t_{obs}}{r_g}\right)^{\beta} \ \mathrm{erg\,s^{-1}}\,. \qquad (3.40)$$

We note that this expression provides a quite general constraint and does not as yet presuppose a specific mechanism for pair injection.

Under quasi-steady circumstances and provided that the flow is hot enough ($kT_e/m_ec^2 \sim 1$), annihilation of MeV *bremsstrahlung* photons could well lead to a charge density in excess of ρ_{GJ} before $\dot{m}$ approaches the critical value $\dot{m}_c$ (Levinson and Rieger, 2011). This would then introduce a further constraint on $\dot{m}$ as to the possible existence of a gap. For typical two-temperature models $T_e \gtrsim 100$ keV is expected (Yuan and Narayan, 2014). However, uncertainties in the electron temperature T_e caused by uncertainties in the electron heating parameters (in particular concerning the viscous dissipation that heats the electrons) along with flow intermittencies can introduce significant uncertainties in the pair production rate. At low accretion rates, early results, for example, suggested that $T_e \propto \dot{m}^{-q}$ with $0 \lesssim q \lesssim 0.2$ (e.g., Mahadevan, 1997; Esin et al., 1997), leading to some further ambiguity concerning pair processes. Note that the scaling in equation (3.40) formally applies to small h/r_g and that we have used $h \sim r_g$ for a representative

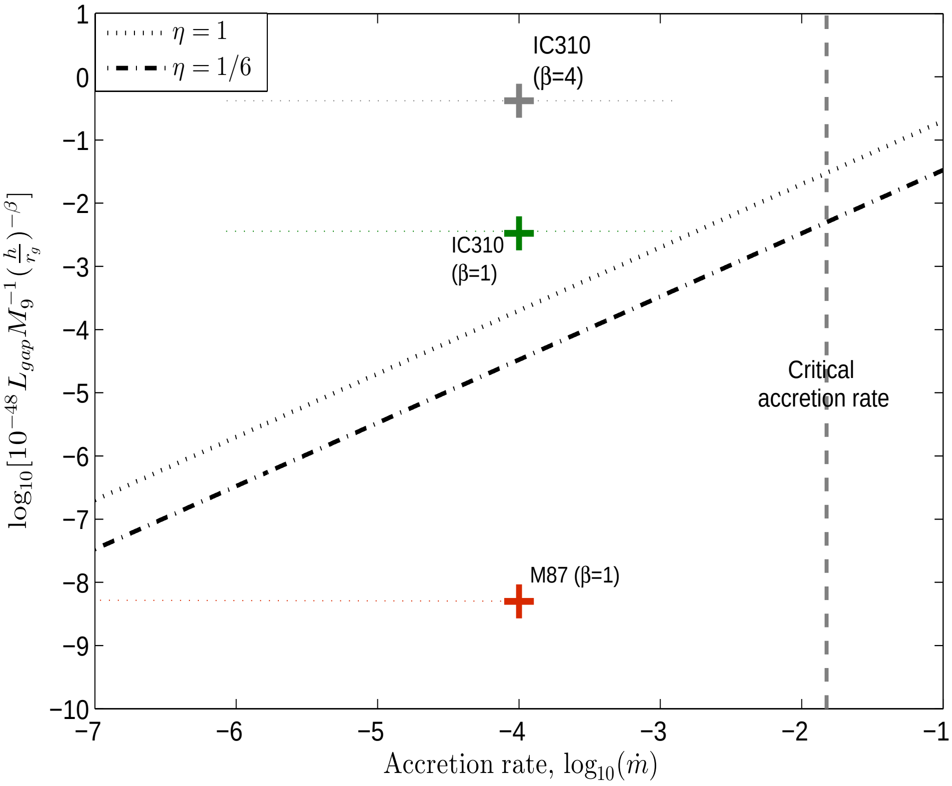

Figure 3.4: Characteristic maximum power of a magnetospheric gap as a function of accretion rate $\dot{m}$. The dotted and dash-dotted lines represent the maximum for $\eta = 1$ and $\eta = 1/6$, respectively. Observed gamma-ray powers below these limiting lines could in principle be produced by magnetospheric gaps.

upper limit. In principle a full general relativity model (e.g., Levinson and Segev, 2017) would be needed to self-consistently evaluate possible gap widths (see chapter 4).

In figure (3.4), the product $P = 10^{-48} L_{gap} M_9^{-1} (h/r_g)^{-\beta}$ with $h \leq r_g$, which provides a normalized measure of the maximum gap power for a given black hole mass and gap size, is shown as function of accretion rate (or correspondingly, of magnetic field strength threading the horizon, $B \propto \dot{m}^{1/2}$; see formula 3.9). The case of a highly ($\eta = 1$) and weakly ($\eta = 1/6$) under-dense gap are given by the dotted and dash-dotted line, respectively. Observed VHE gamma-ray powers that are above these lines are unlikely to originate in (quasi steady) magnetospheric gaps. Both lines preserve their meaning for accretion rate lower than the critical one. In the following, these considerations are applied to the most prominent candidate sources, namely the radio galaxies M87 and IC310 (see chapter 1).

3.2.1 The radio galaxy M87

The *Virgo* Cluster radio galaxy M87 (NGC 4486), located at a distance of $d \simeq 16.7$ Mpc (Mei et al., 2007), has been the first extragalactic source detected at VHE γ-rays (Aharonian et al., 2003). Given its proximity to *Earth*, M87 has been a prime target to probe scenarios for the formation of relativistic jets with high-resolution radio observations exploring scales down to a few r_g (Acciari et al., 2009; Doeleman et al., 2012; Hada et al., 2014, 2016; Kino et al., 2015; Akiyama et al., 2015, 2017, 2019a). In its central region M87 harbours a supermassive black hole of mass, $M = (6.5 \pm 0.7) \times 10^9 M_\odot$, whose shadow/ring has been recently spatially resolved and imaged at radio wavelength of 1.2mm (Akiyama et al., 2019a). This has been the first time that a black hole event horizon shadow has been observed providing strong evidence for the presence of supermassive black holes in the centers of galaxies.

At VHE energies, M87 has revealed at least three active γ-ray episodes during which day-scale flux variability (i.e., $h = c\Delta\tau_{obs} \sim r_g$) has been observed (Aharonian et al., 2006; Albert et al., 2008; Acciari et al., 2009; Abramowski et al., 2012; Aliu et al., 2012). The VHE spectrum is compatible with a relatively hard power-law (photon index ~ 2.2) extending from 300 GeV to beyond 10 TeV, while the corresponding TeV output is relatively moderate, with an isotropic equivalent luminosity of $l_{VHE} \simeq (3 - 10) \times 10^{40}$ $\mathrm{erg\,s^{-1}}$. The inner, pc-scale jet in M87 is considered to be misaligned by $i \sim (15 - 25)^\circ$, resulting in modest *Doppler* boosting of its jet emission and creating challenges for conventional jet models to account for the observed VHE characteristics (see e.g., Rieger and Aharonian, 2012, for review and references).

As already mentioned gap-type emission models offer a promising alternative and thus different realisations have been proposed in the literature (e.g., Neronov and Aharonian, 2007; Levinson and Rieger, 2011; Vincent, 2015; Broderick and Tchekhovskoy, 2015; Ptitsyna and Neronov, 2016). The radio galaxy M87 is overall highly under-luminous with characteristic estimates for its total nuclear (disk and jet) bolometric luminosity not exceeding $l_{\mathrm{bol}} \simeq 10^{42}$ $\mathrm{erg\,s^{-1}}$ by much (e.g., Owen et al., 2000; Whysong and Antonucci, 2004; Prieto et al., 2016). This fact suggests that accretion onto its black hole indeed occurs in a non-standard, advective-dominated (ADAF) mode characterized by an intrinsically low radiative efficiency (e.g., Di Matteo et al., 2003; Nemmen et al., 2014), with inferred accretion rates possibly ranging up to $\dot{m} \sim 10^{-4.0} \ll \dot{m}_c$ (e.g., Levinson and Rieger, 2011) and black hole spin parameter close to its maximum one (e.g., Feng and Wu, 2017). Accretion rates of the order of, $\dot{m} \sim 10^{-5.0}$, have also been recently discussed within

Event Horizon Telescope (EHT) results (Akiyama et al., 2019b).

For such values of the accretion rate, the soft photon field (e.g., see equations 3.10 and 3.11), is sufficiently sparse, so that the maximum *Lorentz* factor $\gamma_e \sim 10^{10}$ of the magnetospheric particles is essentially determined by the *curvature* mechanism. The observed VHE variability is in principle compatible with $h \sim r_g$, so that the different dependence of the gap power on β (see formula 3.35), does not necessarily (in the absence of other, intrinsic gap closure considerations) imply a strong difference in the extractable gap powers. Figure (3.4) illustrates a representative point for M87 (taking $\beta = 1$). The observed VHE luminosity of M87 is some orders of magnitudes lower than the maximum possible gap power (given by the dotted line) and within the bound imposed by ADAF considerations (vertical line). The observed VHE flaring events thus appear compatible with a magnetospheric origin. VLBI observations of (delayed) radio core flux enhancements indeed provide support for the proposal that the variable HE emission in M87 originates at the jet base very near to the black hole (e.g., Acciari et al., 2009; Beilicke and Collaboration, 2012; Hada et al., 2012, 2014).

3.2.2 The radio galaxy IC310

The *Perseus* Cluster galaxy IC310 (J0316+4119) has revealed remarkable VHE variability during a strong flare in November 2012, exhibiting VHE flux variations on timescales as short as $\Delta t_{obs} \simeq 5$ min (Aleksic et al., 2014a). IC310 is located at a distance of $d \sim 80$ Mpc (z=0.019) and widely believed to harbour a black hole of mass $M \simeq 3 \times 10^8 M_\odot$ (Aleksic et al., 2014a, but see also Berton et al. (2015) for a ten times smaller estimate). The flare spectrum in the energy range 70 GeV to 8.3 TeV appears compatible with a hard power law of photon index $\Gamma \simeq 2$ and does not show indications for internal absorption. The observed VHE fluxes can reach levels corresponding to an isotropic-equivalent luminosity of $l_{VHE} \simeq 2 \times 10^{44}$ erg s^{-1}. A variety of considerations based on the orientation of the jet in IC310 (probably $\theta_{los} \sim 10^\circ - 20^\circ$), on kinetic jet power and timing constraints has led Aleksic et al. (2014a) to disfavour alternative proposals for fast VHE variability, such as jet-star interaction (e.g., Barkov et al., 2012) or magnetic reconnection (e.g., Giannios, 2013). Detailed investigation, however, suggests that this does not have to be the case (Aharonian et al., 2017, for details see).

Nevertheless, the fact that the VHE flux varies on timescales Δt_{obs} much shorter than the light travel time across black hole horizon scales, $r_g(3 \times 10^8 M_\odot)/c = 25$ min, has been interpreted as evidence for the occurrence of gap-type particle acceleration on sub-horizon scales, namely of gap height $h \simeq 0.2\ r_g$ (e.g., Aleksic et al., 2014a; Hirotani et al., 2016). To sustain a steady, isotropic equivalent luminosity of $l_{bol} \sim 10^{44}$ erg s^{-1}, the average jet power should satisfy $l_j \gtrsim 10^{42}$ $(\theta_j/0.3 \text{ rad})^2$ erg s^{-1} (see also, Sijbring and de Bruyn, 1998; Ahnen et al., 2017), where θ_j denotes the jet opening angle, suggesting that typical accretion rates should exceed $\dot{m} \gtrsim 10^{-5} M_8^{-1}$ (where $M_8 = M/10^8 M_\odot$). Taking such a jet power as a reference, the expected gap emission would strongly under-predict the required VHE luminosity (equation 3.35). As $l_{gap}^{VHE} \propto B^2$ the gap would need to be temporarily threaded by much higher magnetic fields, and accordingly require much higher accretion rates (see relation 3.9). If $h \sim r_g$ accretion rates of the order of $\dot{m} \sim 10^{-3}$ might seemingly be sufficient. The variability constraint $h \sim 0.2\, r_g$, however, implies that:

$$l_{gap}^{VHE} \lesssim 6 \times 10^{45} \eta_c \left(\frac{\dot{m}_c}{0.01}\right) (0.2)^\beta \qquad erg\, s^{-1}, \tag{3.41}$$

(see formula 3.40). This results in $l_{gap}^{VHE} \lesssim 2 \times 10^{44}$ erg s^{-1} for the $\beta = 2$ with $\eta = 1$, and $l_{gap}^{VHE} \lesssim 10^{42}$ erg s^{-1} assuming $\beta = 4$ with $\eta = 1/6$, see table (3.1).

In figure (3.4), two representative points (i.e., for $\beta = 1$ and $\beta = 4$) illustrating the range for IC310 are depicted. While the case with $\beta = 2$ may appear marginally possible, we note that for accretion rates approaching $\dot{m}_c$ the existence of a gap is not guaranteed. In fact, annihilation of ADAF *bremsstrahlung* photons is likely to lead to an injection of pairs in excess of the *Goldreich-Julian* density, $|\rho_\pm|/|\rho_{GJ}| \sim 3 \times 10^{12} \dot{m}^{7/2}$ (Levinson and Rieger, 2011), suggesting that rates $\dot{m} \lesssim 3 \times 10^{-4}$ are needed to avoid gap closure. Even for the most optimistic case ($\beta = 1$), the maximum gap power (equation 3.40), is then not expected to exceed $l_{gap}^{VHE} \sim 4 \times 10^{43}$ erg s^{-1}. We note that this concurs with a similar estimate in Aharonian et al. (2017). This would imply that the noted VHE flaring event cannot be of a gap-type magnetospheric origin independent of the assumed power index β.

A putative way out could be to assume an inner electron temperature $kT_e/(m_e c^2) < 1$ such that *bremsstrahlung* emission would be suppressed at MeV energies thereby possibly relaxing the pair-injection constraint on $\dot{m}$. Whether this is feasible in the case of IC310 would need detailed disk modelling. But beside of this, the apparently huge magnetic fields required to thread the gap ($B_{d,h} \sim 2 \times 10^5$ G in the case of $\beta = 4$) would suggest a temporary increase in accretion rate in excess of $\dot{m}_c$ required for the existence of an ADAF. This, then, would make it again unlikely that magnetospheric VHE emission from IC310 should become observable (e.g., see Section 3.1.5). The situation might, however, be more complex as unsteady accretion and strong intermittency could be occurring. In the case of IC310 the $\sim$ 5 min flare event detected during 3.7 hrs of MAGIC observations in the night November 12-13, 2012, however, seems part of a higher source state, probably (considering earlier 2009/10 results) of day-scale duration t_d (Aleksic et al., 2014a,b; Ahnen et al., 2017). If one takes the timescale t_{th} for re-adjustment of thermal equilibrium as characteristic measure, $t_{th} \sim t_{dyn}/\alpha_v \sim 1/(\alpha_v\ \Omega_k) \sim \alpha_v^{-1}(r/r_g)^{3/2}\ r_g/c \sim 4\ (r/r_g)^{3/2}$ hr $\lesssim t_d$, then this could be occurring sufficiently fast to ensure re-adjustment of the innermost disk parts. Another situation would be arising if the black hole mass in IC310 would indeed be smaller by an order of magnitude, that is $M \sim 3 \times 10^7 M_\odot$, as suggested by Berton et al. (2015). The observed rapid VHE variability of $\Delta t_{obs} \sim 5$ min would then only imply $h \sim r_g$, such that the different dependence on β (e.g., relation 3.40), would not make a significant difference. The limit introduced by equation (3.40) would then suggest that the observed VHE output might be formally achieved (assuming $\dot{m} \sim 0.01$). However, for such a rate and given the small black hole mass equation 3.10) would imply a synchrotron peak around $E \sim 1$ eV with associated power l_s such, that the VHE photons are unlikely to escape absorption.

In summary, though one could speculate that on r_g-scales the accretion flow evolves in a highly turbulent way, thereby changing its radiative characteristics, a gap-driven magnetospheric origin for the recent VHE flaring event in IC310 appears to be disfavoured unless its black hole mass and accretion state would be highly different.

3.3 Concluding remarks

Gap-driven magnetospheric γ-ray emission from rotating supermassive black holes is a potential candidate for the origin of the highly variable VHE emission seen in some AGN (e.g., Rieger and Katsoulakos, 2017, for review). The presence of strong, unscreened parallel electric field components on black hole horizon scales $\sim r_g$ could easily facilitate efficient particle acceleration, with the accompanying *curvature* and inverse *Compton* processes resulting in appreciable emission at γ-ray energies (Rieger and Levinson, 2018). The efficiency and extractable power, however, depend on details of the gap setup and different realizations are in principle conceivable and encountered in the literature.

In this chapter, we examined possible implications of this by means of a simple phenomenological description that, though heuristic, recovers the relevant dependencies. Accordingly, the maximum extractable gap luminosity is in general proportional to the classical *Blandford-Znajek* jet power, $l_{BZ} \propto \dot{m}\, M$, and a function of the gap height h, $l_{gap} \sim l_{BZ}\, (h/r_g)^{\beta}$, where the power index β is dependent on the respective gap-setup (e.g., see table 3.1). In order for this emission to become observable, VHE photons need to be able to escape the accretion environment of the black hole. Transparency to $\gamma\gamma$-pair production in fact requires an under-luminous or radiatively inefficient environment (RIAF/ADAF), and this introduces a relevant constraint on possible accretion rates of $\dot{m} \lesssim 0.01$. While for a fixed background a larger black hole mass (size) could be conducive to dilution of the soft photon field (facilitating VHE transparency) and increase l_{BZ}, the detection of rapid gamma-ray variability with $c\Delta t_{obs} \sim h < r_g$ reduces the maximum gap power $l_{gap}^{VHE} \propto M^{1-\beta}$ (for $\beta > 1$) and diminishes the VHE prospects for source detection. When put in the context of current observations, these considerations suggest that the variable (day-scale) VHE activity seen in the radio galaxy M87 ($M \simeq 6.5 \times 10^9 M_\odot$) may be compatible with a magnetospheric origin, while such an origin seems less likely for the (minute-scale) VHE activity in IC310 (assuming $M \simeq 3 \times 10^8 M_\odot$).

Our analysis implies that variability information will be crucial to get deeper insights into the physics of the putative gaps, to probe different potential scalings and to generally assess the plausibility of a magnetospheric origin. On average, however, (quasi steady) magnetospheric VHE gamma-ray emission in AGN is expected to be of rather moderate luminosity when compared to the strongly *Doppler*-boosted jet emission from *blazars*. The jet usually needs to be sufficiently misaligned for the gap emission not to be masked by *Doppler*-boosted jet emission, making nearby misaligned AGN the most promising source targets. The possible impact of intermittencies in the gap formation process (e.g., Levinson and Segev, 2017) on the VHE characteristics could be of particular interest in this regard. The increase in sensitivity with the upcoming CTA instrument will allow to probe variability timescales $< r_g/c$ for a number of these sources, and thereby allow a better census of magnetospheric γ-ray emitter.

Chapter 4

Gap accelerator in Kerr black hole magnetospheres

In the third chapter we rather adopted a phenomenological approach, in order to draw useful conclusions relative to the emission produced in a black hole magnetosphere. Without considering the exact location of the emitting region, we calculated the terminal *Lorentz* factor of the accelerated leptons $e^{\pm}$ (e.g., up to $\Gamma_e \approx 10^{10}$) and the peak energies of the γ-ray emission due to inverse *Compton* scattering and *curvature* radiation (e.g., $E_{IC} \approx 10^4$ TeV and $E_{cur} \approx few$ TeV). In addition, we estimated the maximum power that a charge-empty magnetospheric cavity permits. As it has been already mentioned, the latter constitutes a useful tool of judging, if an observed extragalactic flaring event is of possible magnetospheric nature.

In this chapter we unfold a detailed analysis of an one-dimensional (1D) steady gap accelerator formed across the null surface (e.g., see section 2.1.3) of a rapidly rotating (i.e., $\alpha_s^* \approx 1$) black hole magnetosphere. In specific, we present the steady gap model as first introduced in the frame of filling the magnetosphere with pair plasma (Beskin et al., 1992; Hirotani and Okamoto, 1998). For the current study, two major changes have been implemented to the model. Firstly, we explore solutions of the gap structure taking into account the general relativistic expression of *Gauss's* law and applying the relativistic formula of the *Goldreich-Julian* charge density, ρ_{GJ}. Secondly, we assume that the magnetospheric configuration and especially the gap accelerator is embedded within the radiation field emitted by an optically thin *Advection Dominated Accretion Flow* (ADAF).

We consider that the gap model, adjusted to the above additions, is a useful tool to get insight into the possible magnetospheric emission from *Active Galactic Nuclei* (AGNs). For a full relativistic treatment of gap accelerators we refer the interested reader to recently published studies (Hirotani et al., 2016, 2017; Levinson and Segev, 2017). As we show below, however, the implementation of the relativistic *Goldreich-Julian* charge density ρ_{GJ} captures all the relevant information.

In the following, we present the equations that govern the structure of the gap accelerator. Subsequently, we introduce appropriate boundary conditions and describe the numerical process that we followed, in order to solve the system of equations. We finally illustrate the resulting gap structure and comment on charge acceleration and radiative output. We then compare observations and analytical estimates.

4.1 The governing equations

Let us consider that a fast rotating supermassive black hole (e.g., $M > 10^6 M_\odot$) is surrounded by a radiatively inefficient accretion flow (i.e., an ADAF). The accretion disk is supposed to be in (quasi) steady state and, in particular, the material of it is accreted onto the hole with constant rate, $\dot{M}$. The ADAF spectrum typically ranges from radio frequencies up to γ-rays (i.e., from $\sim 10^{-6}$ eV to $\sim$ MeV) (Mahadevan, 1997), (see also section 2.2). Provided that astrophysical disks support a large-scale[1] magnetic field (Hawley et al., 2015, for a review), we normally expect that this follows the inward motion of gas and accumulates in the immediate vicinity of the black hole. We further consider the existence of a plasma source (e.g., $\gamma\gamma$ annihilation of disk photons or electromagnetic cascades) capable of filling the black hole magnetosphere with a sufficient amount of charged particles.

In addition, we assume that the black hole rotation Ω^H, the magnetic field threading the event horizon $\mathbf{B}_H$ and the amount of charges ρ_e are such that they can ensure *degeneracy* (i.e., $\mathbf{E} \cdot \mathbf{B} = 0$) and *force-freeness* (i.e., $\rho_e \mathbf{E} + (\mathbf{j}/c) \times \mathbf{B} = 0$) almost everywhere in the magnetosphere. It is known, that a *force-free* magnetosphere leads to efficient extraction of the rotational energy of the black hole, a process which is strongly associated with jet/outflow formation (Blandford and Znajek, 1977). Even under these circumstances, however, the emergence of electric field components across the null surface parallel to the magnetic field (i.e., gap accelerators) is possible, since continuous charge replenishment is required. Given these considerations, the gap accelerator is confined to a region which contains large-scale electromagnetic fields[2], charged particles (i.e., either in surplus in the *force-*

---

[1] The term “large-scale” magnetic field is attributed to the inner parts of the accretion flow.

[2] In what follows, we adopt the split monopole: $\Psi = 4\pi r_H^2 B_H (1 - \cos\theta)$, where θ gives the angle with respect to the polar axis. This choice of magnetic configuration facilitates

free domain $\rho_e \geq \rho_{GJ}$, or in deficit within the accelerating zone $\rho_e < \rho_{GJ}$) and photons due to the ADAF emission.

It is worth recapturing, at this point, the physics of the gap mechanism, since we have already described its ingredients. Seed leptons $e^{\pm}$ injected somehow into the gap are instantaneously accelerated along the parallel electric field component (e.g., see section 3.1.3). Their resulting energy saturates, given that they either up-scatter disk photons to γ-ray energies or emit *curvature*[3] photons themselves[4]. Subsequently, pair production due to $\gamma\gamma$-annihilation with the soft photons of the accretion disk provides extra leptons to the gap. These secondary leptons are also subjected to acceleration and γ-ray emission. Correspondingly, the secondary γ-ray photons produce the next generation of pairs which, in turn, radiate the next generation of photons and so on. In such a way, an electromagnetic cascade is triggered and ends only when the charge density ρ_e reaches the *Goldreich-Julian* one, ρ_{GJ}.

In the section below, we present the system of equations which determines the structure of the (1D) gap accelerator found in steady state. In particular, we derive the expressions for the radial distribution of the parallel electric field component, the *Lorentz* factor of the particles, the charge density for both species (i.e., electrons and positrons) and finally, the number density of the γ-ray photons.

4.1.1 The parallel electric field

The black hole rotation as well as the nearby presence of a magnetic field result in the appearance of a large scale electric field. More specifically, the electric field is induced outside the event horizon due to the change of magnetic flux (e.g., see *Faraday's* law) or due to the presence of charges (e.g., see *Gauss's* law). Here we seek to determine the component of the electric field which is responsible for particle acceleration. Given that charged particles move along magnetic field lines (e.g., see chapter 3), the electric field component that indeed accelerates them is the parallel one. Below, we give the equation that describes the parallel electric field along the gap extension. Aiming to capture the critical relativistic information, we develop the concept in the framework of the "3 + 1" formalism (Thorne and Macdonald, 1982).

---

the numerical integration of the equations along the radial dimension.

[3] Despite the choice of the split monopole as field geometry, we include *curvature* radiation in the model. We use $R_c \approx r_g$ as a typical value for the curvature radius (see also, Levinson and Segev, 2017).

[4] Energy loss of particles due to *synchrotron* emission is not significant in gap physics (Beskin et al., 1992).

Our reference point is *Gauss's* law which relates the electric field to the charge density. In the "3 + 1" formalism *Gauss's* law has a similar form with the classical one:

$$\nabla \cdot \mathbf{E} = 4\pi\rho_e, \tag{4.1}$$

where $\mathbf{E}$ and ρ_e are the electric field and the charge density, respectively, as measured (in units of proper time τ) by a *Zero Angular Momentum Observer* (ZAMO)[5].

Assume now that we want to transform the electric field from the coordinate system of ZAMO to a frame comoving with the field lines[6]. The usefulness of such a movement will be elucidated below. For the time being, it is very instructive to think that ZAMO observers play an equivalent role as those of laboratory frames in special *Relativity.* Hence, it is sufficient to apply a *Lorentz* transformation, in order to write the comoving electric field (in units of global time t):

$$\mathcal{E}_{||} = \gamma^F \left(\alpha_l \, \mathbf{E} + \frac{\mathbf{v}^F}{c} \times \alpha_l \, \mathbf{B} \right) \approx \alpha_l \, \mathbf{E} + \frac{(\Omega^F - \omega)}{2\pi c} \nabla\Psi, \tag{4.2}$$

where $\alpha_l \, \mathbf{E}$ and $\alpha_l \, \mathbf{B}$ are the electric and magnetic field as measured (now in units of global time t) by a ZAMO frame, $\gamma^F = 1/\sqrt{1 - (\mathbf{v}^F/c)^2}$ is the *Lorentz* factor (here $\gamma^F \approx 1$) and $\mathbf{v}^F = (1/\alpha_l)(\Omega^F - \omega) \, \widetilde{\omega} \, \mathbf{e}_{\hat{\phi}}$ is the field line velocity (measured by ZAMO in units of proper time τ)[7]. We remind (e.g., see chapter 2.1.1) that α_l is the *lapse* function, Ω^F is the angular velocity of the field line, ω is the *Lense-Thirring* angular velocity and $\widetilde{\omega}$ is the cylindrical radius. The velocity has been decomposed into the physical components $(\mathbf{e}_{\hat{r}}, \mathbf{e}_{\hat{\theta}}, \mathbf{e}_{\hat{\phi}})$.

---

[5] ZAMOs are the fiducial observers located at each point of the absolute space around a rotating gravitational center. The fiducial observers, which are responsible for making physical measurements in their neighborhood, constitute the proper frames of general *Relativity* in the concept of "3 + 1" formalism. A more precise definition can be found in (Thorne et al., 1986).

[6] Magnetic field lines which thread the horizon are forced to rotate due to the rotation of the black hole.

[7] The product $\mathbf{v}^F \times \mathbf{B}$ is a vector measured by ZAMO in units of proper time τ. We can find how this vector evolves in units of global time t, by simply multiplying it with the *lapse* function α_l.

Obviously, the second term in equation (4.2) describes the electric field of a *degenerate*, *force-free* and stationary black hole magnetosphere (Thorne et al., 1986):

$$\mathbf{E}^{ff} = -\frac{(\Omega^F - \omega)}{2\pi\,\alpha_l\,c}\,\nabla\Psi. \tag{4.3}$$

If $\mathcal{E}_{||} = 0$ everywhere in space, then the electric field is given by equation (4.3). In this case, the electric field is purely perpendicular to the field lines and particle acceleration does not occur. On the contrary, if $\mathcal{E}_{||} \neq 0$ somewhere in space, equation (4.2) reveals components of the electric field parallel to magnetic lines. As a result, charged particles injected into such regions are subjected to "one-shot" acceleration.

Substituting equation (4.2) into *Gauss's* law (4.1) one obtains:

$$\nabla \cdot \left(\frac{\mathcal{E}_{||}}{\alpha_l}\right) + \nabla \cdot \left[-\frac{(\Omega^F - \omega)}{2\pi\,\alpha_l\,c}\,\nabla\Psi\right] = 4\pi\rho_e. \tag{4.4}$$

We can now define the general relativistic version of the *Goldreich-Julian* charge density and formulate its physical meaning (Goldreich and Julian, 1969). Accordingly, we have that the critical density ρ_{GJ} is given by the following relation (see section 2.1.2):

$$\rho_{GJ} = \frac{1}{4\pi}\nabla \cdot \mathbf{E}^{ff} = \frac{1}{4\pi}\nabla \cdot \left[-\frac{(\Omega^F - \omega)}{2\pi\,\alpha_l\,c}\,\nabla\Psi\right]. \tag{4.5}$$

In this situation, we could say that the amount of charges and their distribution within the magnetosphere are such that it can support a perpendicular electric field with respect to the field lines. In an environment rich of plasma (i.e., $\rho_e > \rho_{GJ}$), the ability of charges to move freely along magnetic lines will also ensure *degeneracy* (i.e., $\mathbf{E} \cdot \mathbf{B} = 0$). In an environment poor of plasma (i.e., $\rho_e < \rho_{GJ}$), on the other hand, the amount of charges is not sufficient to fully screen the field. Therefore, a parallel electric field component can emerge in charge-sparse regions or else gaps.

Using the definition of the critical density (4.5), and substituting into equation (4.4) we find:

$$\nabla \cdot \left(\frac{\mathcal{E}_{||}}{\alpha_l} \right) = 4\pi(\rho_e - \rho_{GJ}), \tag{4.6}$$

where below we calculate the divergence of the vector $\mathcal{E}_{||}/\alpha_l$. Assuming that the black hole magnetosphere is axisymmetric (i.e., $\partial/\partial\phi = 0$) and ignoring polar variations (i.e., $\partial/\partial\theta = 0$) in *Gauss's* law, equation (4.6) becomes:

$$\frac{1}{\sqrt{|\gamma|}} \frac{\partial}{\partial r} \left(\sqrt{|\gamma|} \frac{\mathcal{E}^r_{||}}{\alpha_l} \right) = 4\pi(\rho_e - \rho_{GJ}), \tag{4.7}$$

where $|\gamma| = s^4 \widetilde{\omega}^2/\Delta$ is the determinant of the metric γ_{ij} in absolute (3-dimensional) space. We remind the reader (e.g., see section 2.1.1) that $s^2 = r^2 + \alpha_s^2 \cos^2\theta$, $\widetilde{\omega} = (\Sigma/s)\sin\theta$, $\Delta = r^2 - 2r_g\, r + \alpha_s^2$ and $\Sigma^2 = (r^2 + \alpha_s^2)^2 - \alpha_s^2\, \Delta \sin^2\theta$. The spin of the black hole is $\alpha_s = J/Mc$ and $J = GM^2/c$ is the angular momentum. It is worth emphasizing that $\mathcal{E}^r_{||}$ is the contravariant component of the corotating electric field and not the physical one, that is $\mathcal{E}^{\hat{r}}_{||}$. If one wishes to express the physical component in terms of the contravariant one, then one should write that:

$$\mathcal{E}^{\hat{r}}_{||} = \sqrt{\gamma_{rr}}\, \mathcal{E}^r_{||}, \tag{4.8}$$

where γ_{rr} is the metric element of *absolute* space.

Equation (4.7) can be rearranged as:

$$\frac{d}{dr} \left(\frac{\mathcal{E}^r_{||}}{\alpha_l} \right) = 4\pi(\rho_e - \rho_{GJ}) - \frac{1}{\sqrt{|\gamma|}} \frac{d\sqrt{|\gamma|}}{dr} \left(\frac{\mathcal{E}^r_{||}}{\alpha_l} \right), \tag{4.9}$$

where the term $\mathcal{A} := (1/\sqrt{|\gamma|})(d\sqrt{|\gamma|}/dr)$ can be evaluated by applying the derivative over r:

$$\mathcal{A} = \frac{r}{s^2} + \frac{1}{\Sigma^2}\left[2r\left(r^2 + a_s^2\right) - a_s^2 \sin^2\theta\,(r - r_g)\right] - \frac{(r - r_g)}{\Delta}. \qquad (4.10)$$

The remaining element of expression (4.9), that has to be calculated, is the *Goldreich-Julian* charge density ρ_{GJ}. Using equation (4.5) we have:

$$\rho_{GJ} = -\frac{1}{8\pi^2 c}\nabla_i\left[\frac{\left(\Omega^F - \omega\right)}{\alpha_l}\nabla^i\Psi\right], \qquad (4.11)$$

meaning that in order to determine the critical density, we need to compute the 3-dimensional *Laplacian*, that is the product $\nabla_i\nabla^i$.

In general, operations in general *Relativity* concern vectors expressed either in contravariant (i.e., upper index) or covariant (i.e., lower index) components. A contravariant vector is analysed in components by means of the coordinate base $(\mathbf{e}_r, \mathbf{e}_\theta, \mathbf{e}_\phi)$, while a covariant one is analysed by means of the *1-form* basis $(\mathbf{e}^r, \mathbf{e}^\theta, \mathbf{e}^\phi)$. Adopting this convention, we can use the *Einstein* summation rule in equation (4.11). The gradient of magnetic flux decomposed into covariant components is:

$$\nabla_i\Psi = \sum_{i=1}^{3}\frac{\partial\Psi}{\partial x^i}\,\mathbf{e}^i = \frac{\partial\Psi}{\partial r}\,\mathbf{e}^r + \frac{\partial\Psi}{\partial\theta}\,\mathbf{e}^\theta, \qquad (4.12)$$

where $\partial\Psi/\partial r$ and $\partial\Psi/\partial\theta$ are the covariant components of $\nabla\Psi$. Exploiting the properties of the metric tensor, we write the magnetic flux gradient in terms of contravariant components as well:

$$\nabla^k = \gamma^{ki}\nabla_i = \gamma^{kr}\nabla_r + \gamma^{k\theta}\nabla_\theta = \gamma^{kr}\frac{\partial}{\partial r} + \gamma^{k\theta}\frac{\partial}{\partial\theta}, \qquad (4.13)$$

where this gives, finally, the components $\nabla^r = \gamma^{rr}\frac{\partial}{\partial r}$ and $\nabla^\theta = \gamma^{\theta\theta}\frac{\partial}{\partial\theta}$. Furthermore, we note that γ^{rr} and $\gamma^{\theta\theta}$ are elements of the inverse matrix of metric (see section 2.1.1). Therefore, one finds:

$$\nabla^k \Psi = \gamma^{rr}\frac{\partial \Psi}{\partial r}\,\mathbf{e}_r + \gamma^{\theta\theta}\frac{\partial \Psi}{\partial \theta}\,\mathbf{e}_\theta = \frac{\Delta}{s^2}\frac{\partial \Psi}{\partial r}\,\mathbf{e}_r + \frac{1}{s^2}\frac{\partial \Psi}{\partial \theta}\,\mathbf{e}_\theta. \tag{4.14}$$

Of course, we can always transform any vector from some coordinate base to the orthonormal one ($\mathbf{e}_{\hat{r}}$,$\mathbf{e}_{\hat{\theta}}$,$\mathbf{e}_{\hat{\phi}}$), taking the physical components, $\nabla_{\hat{k}}\Psi = \nabla^{\hat{k}}\Psi$.

From the discussion above, we are able now to give the gradient of magnetic flux in terms of contravariant components. Accordingly, we write:

$$\nabla^k \Psi = \nabla^\theta \Psi = 4\pi r_H^2 B_H \frac{\sin\theta}{s^2}\,\mathbf{e}_\theta, \tag{4.15}$$

where the resultant vector has no radial dependence, since we assume a split monopole. Substituting equation (4.15) in equation (4.11), the critical charge density becomes:

$$\rho_{GJ} = -\frac{B_H\, r_H^2}{2\pi c}\nabla_\theta \left[\frac{(\Omega^F - \omega)}{\alpha_l}\,\frac{\sin\theta}{s^2}\,\mathbf{e}_\theta\right], \tag{4.16}$$

where $\nabla_\theta = (1/\sqrt{|\gamma|})(\partial/\partial\theta)(\sqrt{|\gamma|}\,)$. Finally, after some manipulation we obtain the following relation:

$$\begin{aligned}\rho_{GJ} = -\frac{(\Omega^F - \omega)\, B_H\, \cos\theta}{2\pi\, c\, \alpha_l} & \left[\frac{2\, r_H^2}{s^2} - 2\,\alpha_s^2\,\frac{\Delta\, r_H^2}{s^2\,\Sigma^2}\,\sin^2\theta + \right. \\ & \left. + 2\alpha_s^2\,\frac{r_H^2}{s^4}\,\sin^2\theta - \frac{4c\,\alpha_s^3\, r_g\, r_H^2}{(\Omega^F - \omega)}\,\frac{r\,\Delta}{s^2\,\Sigma^4}\,\sin^2\theta\right].\end{aligned} \tag{4.17}$$

The dominant term, which mainly determines the distribution of the density along the r-direction, is the first one inside the brackets. Note that for $\alpha_s \approx 0$, equation (4.17) reduces to the expression calculated by *Beskin* in the limit of slow hole rotation (Beskin, 2010).

We conclude this subsection, highlighting that equation (4.9), with the addition of expressions (4.10) and (4.17), constitutes the first equation of the system that describes the structure of the gap accelerator. We continue our analysis below with the equation of motion.

4.1.2 The equation of motion

Electrons and positrons moving into the gap will experience an efficient "one-shot" acceleration. As discussed in chapter (3), the *Lorentz* factor of particles reaches almost instantaneously its maximum value, where acceleration is balanced by energy losses. Without loss of generality we can assume that $\mathcal{E}^r_{||} < 0$, namely, the electric field points towards the black hole. This configuration is normally realised, if the axis of black hole rotation is aligned with the magnetic one (e.g., see equation 4.3). As a consequence of the field direction, electrons move outwards while positrons inwards, creating a charge species asymmetry across the gap boundaries. Moreover, the change of charge sign compensates the change of velocity sign, resulting in a common equation of motion for both species. Hence, the equation that describes the motion of leptons within the gap is given:

$$m_e c^2 \frac{d\Gamma_e}{dr} = -e\mathcal{E}^r_{||} - \frac{P_{IC}}{c} - \frac{P_{cur}}{c}, \tag{4.18}$$

where Γ_e is the *Lorentz* factor of the particle and P_{IC}/c, P_{cur}/c are the drag forces caused by inverse *Compton* scattering and *curvature* radiation, respectively.

Leptons, moving along field lines within the gap, upscatter the soft photons radiated from the inner sector of the ADAF. The drag force due to inverse *Compton* emission (i.e., in units of *erg* cm^{-1}) can be defined as:

$$\frac{P_{IC}}{c} = \int\limits_{E_s^{min}}^{m_e c^2/\Gamma_e} E_\gamma \, \sigma_{KN} \, \frac{dN_s}{dE_s} \, dE_s + \int\limits_{m_e c^2/\Gamma_e}^{E_s^{max}} E_\gamma \, \sigma_{KN} \, \frac{dN_s}{dE_s} \, dE_s, \tag{4.19}$$

where the ratio dN_s/dE_s corresponds to the number density of the ADAF soft photons per unit energy (e.g., see figure 2.7)[8] and σ_{KN} is the total *Klein-Nishina* cross section (Rybicki and Lightmann, 1979):

$$\sigma_{KN}(x) = \frac{3}{4}\sigma_{\mathcal{T}} \left\{ \frac{1+x}{x^3} \left[\frac{2x(1+x)}{1+2x} - \ln(1+2x) \right] + \right. \\ \left. + \frac{1}{2x}\ln(1+2x) - \frac{1+3x}{(1+2x)^2} \right\}, \quad (4.20)$$

where $x = E_s\Gamma_e/m_ec^2$ and $\sigma_{\mathcal{T}}$ is the *Thomson* cross section. The transition from *Thomson* to *Klein-Nishina* limit roughly occurs at energy $E_s^t = m_ec^2/\Gamma_e$. If the initial soft photon has an energy smaller than this (i.e., $E_s < E_s^t$), then its post-collision γ-ray energy is on average $E_\gamma \approx \Gamma_e^2 E_s$. On the other hand, for $E_s > E_s^t$ the upscattered photon energy is limited by the energy of the electron, $E_\gamma = \Gamma_e m_e c^2$, in the *Klein-Nishina* limit.

We also assume that leptons emit γ-ray *curvature* photons. The drag force due to *curvature* emission (i.e., in units *erg* cm^{-1}) is (Rieger, 2011):

$$\frac{P_{cur}}{c} = \frac{2e^2}{3R_c^2}\Gamma_e^4. \quad (4.21)$$

For the results below, a typical value for the curvature radius of the order of the gravitational one has been assumed, i.e., $R_C \approx r_g$.

In figure (4.1) we illustrate the drag forces, normalized in units of r_g/m_ec^2, as function of the particle *Lorentz* factor. It is obvious that inverse *Compton* losses dominate these of *curvature* for *Lorentz* factors lower than $\Gamma_e \sim 10^{9.5}$. The drag force due to *curvature* radiation, on the other hand, is the main channel of decelerating the particle above this value. Implementing accretion rates smaller than $\sim 10^{-4}$ for the ADAF spectrum, we find that *curvature* losses start dominating at even lower *Lorentz* factors.

To summarize this subsection, we note that relation (4.18), with the addition of expressions (4.19) and (4.21), provides the second equation of the system that describes the structure of the gap. It is worth commenting, at this point, on equation (4.19). As can be seen, the dependence of the *Lorentz*

---

[8] We estimate the photon number density per unit energy, using $dN_s/dE_s = F_\nu/4\pi d^2 chE_s$. F_ν is the ADAF spectrum in units of *erg* sec^{-1} Hz^{-1} and $E_s = h\nu$ is the soft photon energy. We compute in the following the number of photons for a sphere with radius $d \approx 5r_g$.

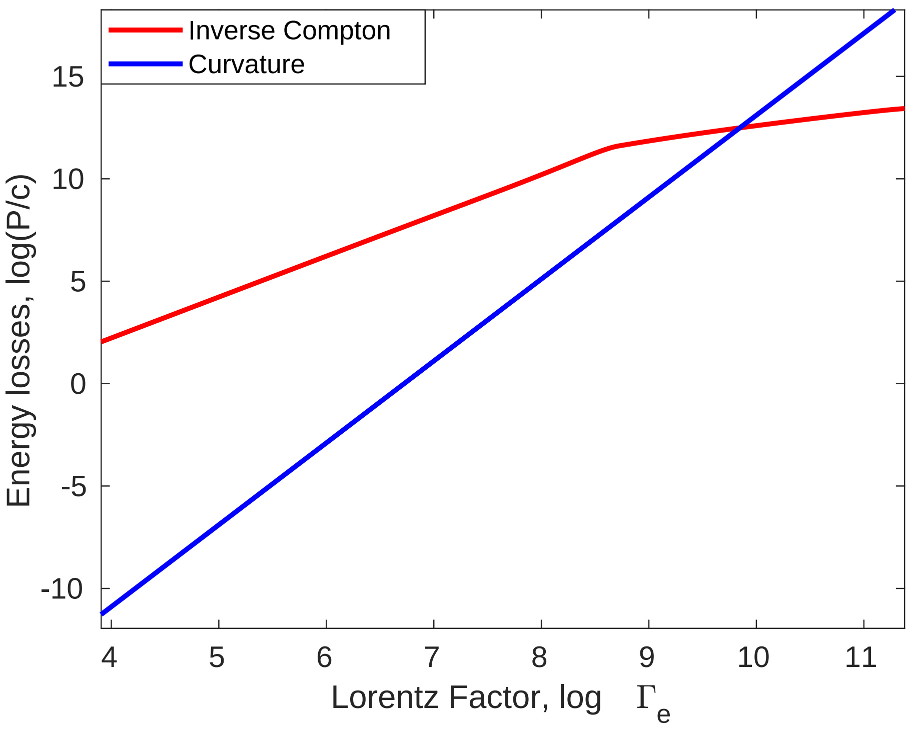

Figure 4.1: The drag forces for inverse Compton (red line) and curvature emission (blue line) as function of the particle *Lorentz* factor. Energy losses are given in units of $r_g/m_e c^2$, while the parameters we use are: $M_9 = 1.0$, $\alpha_s^* = 1.0$, $\dot{m} = 10^{-4.0}$ and $\theta = 15^o$.

factor is within the integrals as well, complicating the numerical manipulation. In order to reduce complexity, we instead use an extrapolation of the data points from *Compton* losses (e.g., see red curve in figure 4.1) with a fifth order polynomial function. Below, we continue the analysis with the continuity equations.

4.1.3 The lepton distribution

The existence of leptons in the gap accelerator might be the result of more than one physical process. The primary particles, for example, could be injected into the accelerating shell via annihilation of MeV photons of the ADAF emission or via diffusion (Levinson and Rieger, 2011). Nevertheless, we expect that the "photon-pair" cascade, which develops inside the accelerator, would be mainly responsible for the presence of charged particles ($e^{\pm}$) and the structure of the gap. By definition, of course, the total charge density within the gap must not be in excess (i.e., $\rho_e < \rho_{GJ}$). Hence, we plausibly consider that the pair cascade does not provide full screening everywhere, maintaining in such a way a stationary gap within the magnetosphere.

The distribution of electrons and positrons inside the gap can be found by means of the continuity equation. Assuming that the black hole magnetosphere is in steady state (i.e., $\partial/\partial t = 0$), the continuity equation for both species ($e^{\pm}$) is in general given by:

$$\nabla \cdot \mathbf{J}^{\pm} = \mathcal{S}^{\pm}, \tag{4.22}$$

where $\mathbf{J}^{\pm}$ is the vector of current and $\mathcal{S}^{\pm}$ is the source term explained below. The positive sign in formula (4.22) refers to positrons, while the negative one to electrons. Given that we investigate the radial distribution of charge densities, we can alternatively write equation (4.22) as follows:

$$\nabla \cdot (\rho^{\pm}\mathbf{v}_e^{\pm}) = \mathcal{S}^{\pm} \Rightarrow \frac{d(\rho^{\pm}v_e^{\pm})}{dr} = \mathcal{S}^{\pm}, \tag{4.23}$$

where $\rho^{\pm}$ and $v_e^{\pm}$ are the charge density and the velocity of positrons and electrons, respectively. We remind that positrons move in accordance with the electric field direction, while electrons to the opposite side. Eventually, the continuity equations of positrons and electrons are:

$$-\frac{d}{dr}\left[\rho^{+}c\left(1-\frac{1}{\Gamma_e^2}\right)^{\frac{1}{2}}\right] = \mathcal{S}^{+}, \tag{4.24}$$

$$\frac{d}{dr}\left[\rho^{-}c\left(1-\frac{1}{\Gamma_e^2}\right)^{\frac{1}{2}}\right] = \mathcal{S}^{-}. \tag{4.25}$$

As previously discussed, the accelerated particles emit γ-rays due to *Compton* upscattering of the disk soft photons. The resulting high-energy photons are able to annihilate with soft ones, producing more pairs within the gap accelerator. Consequently, leptons coming from all generations are included in equations (4.24) and (4.25) by means of the source function $\mathcal{S}^{\pm}$.

In order now to estimate the term $\mathcal{S}^{\pm}$, let us consider the distribution of γ-ray photons $P_{\gamma}^{\pm}(r, E_{\gamma})$ (i.e., number of photons per unit length per unit energy). We denote with “+” sign the photons which move outwards and with “−” the photons which move towards the black hole. For a given energy range (i.e., from E_γ to $E_\gamma + dE_\gamma$) the number of photons per unit length is simply $\left[P^+_\gamma(r,E_\gamma) + P^-_\gamma(r,E_\gamma)\right] dE_\gamma$. Since not all the photons will pair-produce efficiently, we need a corresponding coefficient to multiply the number of photons, so as to estimate the correct amount of the injected pairs[9]. Hence, this coefficient is given by (in units of cm^{-1}):

$$\alpha_p(E_\gamma) = \int\limits_{\frac{(m_e c^2)^2}{E_\gamma}}^{E_s^{max}} \sigma_p \, \frac{dN_s}{dE_s} \, dE_s, \tag{4.26}$$

where σ_p is the pair production cross section in a collision between two photons with energies E_s and E_γ. The cross section σ_p is given by the following formula (Berestetskii et al., 1989):

$$\sigma_p = \frac{3}{16}\sigma_\tau(1-\beta_*^2)\left[(3-\beta_*^4)\ln\left(\frac{1+\beta_*}{1-\beta_*}\right) - 2\beta_*(2-\beta_*^2)\right], \tag{4.27}$$

where $\beta_* = \sqrt{1 - m_e^2 c^4/E_s E_\gamma}$. We note that in the numerical integration of the system only head-on photon collisions have been taken into account. In addition, one can see that the coefficient α_p for a given E_γ is active only when the colliding soft photon has energy above the threshold, that is $E_s \geq (m_e c^2)^2/E_\gamma$. Eventually, the number of particles which is injected into the gap due to photon-photon annihilation is given by $a_p(E_\gamma)[P^+_\gamma(r,E_\gamma) + P^-_\gamma(r,E_\gamma)]dE_\gamma$. Therefore, the total pair production rate (i.e., incoming charge density per unit time) is simply written:

$$\mathcal{S}^\pm = \pm ec \int\limits_0^\infty a_p(E_\gamma)[P^+_\gamma(r,E_\gamma) + P^-_\gamma(r,E_\gamma)]dE_\gamma. \tag{4.28}$$

In the implementation of equation (4.28) the *curvature* photons are in principle also included in the pair production rate. We do know that only

---

[9] This is equivalent to the absorption coefficient in the radiation transfer equation (e.g., $a_p = n\sigma_\tau = 1/\bar{l}$, where n is the number density of the absorbers and $\bar{l}$ the mean free path).

soft photons with frequency above $\sim 10^{14}$ Hz interact with *curvature* ones, the typical energy of which is around $\sim 10^{12}$ eV. However, the number of photons above $\sim 10^{14}$ Hz is many orders of magnitude less than this below (e.g., see figure 2.7). As a consequence, we can reasonably assume that *curvature* photons have negligible contribution to the pair production rate.

We can further apply some manipulation to the continuity equations, so as to reveal some physical characteristics. Hence, adding equations (4.24) and (4.25), we obtain the formula:

$$\frac{d}{dr}\left[(\rho^- - \rho^+)c\left(1-\frac{1}{\Gamma_e^2}\right)^{\frac{1}{2}}\right] = 0. \tag{4.29}$$

Equation (4.29) implies that the total current along a magnetic field line is constant:

$$(\rho^- - \rho^+)c\left(1-\frac{1}{\Gamma_e^2}\right)^{\frac{1}{2}} = J_o, \tag{4.30}$$

where J_o is the current. If we subtract, on the other hand, equations (4.24) and (4.25) we find:

$$\frac{d}{dr}\left[(\rho^+ + \rho^-)c\left(1-\frac{1}{\Gamma_e^2}\right)^{\frac{1}{2}}\right] = -2ec\int\limits_0^\infty a_p(P_\gamma^+ + P_\gamma^-)dE_\gamma. \tag{4.31}$$

To sum up, relations (4.29) and (4.31) are added to the system that describes the structure of the gap. Below, we close the set of equations, giving the expressions for the distributions of γ-ray photons.

4.1.4 The γ-ray photon distributions

We have discussed so far about the corotating electric field and the charged particles located in the gap. We are now turning towards the last ingredient for the gap structure, namely the resulting γ-ray photons. The distribution of high energy photons for the (1D) gap accelerator in steady state is described by the *Boltzmann* equation and given by:

$$\pm c\frac{d}{dr}P_\gamma^\pm(r, E_\gamma) = \mathcal{N}^\pm, \tag{4.32}$$

where $\mathcal{N}^\pm$ represents the rate of change of the spatial number density of photons per unit energy. Roughly speaking, the function $\mathcal{N}^\pm$ can be also written as $\mathcal{N}^\pm = (\mathcal{N}_{gain} - \mathcal{N}_{losses})^\pm$, where the term $\mathcal{N}_{gain}$ represents γ-ray photons added to equation (4.32), while the term $\mathcal{N}_{losses}$ represents photons that leave the system. In the followings, we seek to express the terms $\mathcal{N}_{gain}$ and $\mathcal{N}_{losses}$.

The γ-ray photons can get absorbed by annihilation with ADAF soft photons, leading to a reduction of the photon population in formula (4.32). We can easily express the term $\mathcal{N}_{losses}$, since we have already defined the distribution of γ-ray photons $P_\gamma^\pm$ and the possibility for $\gamma\gamma$ annihilation. Therefore, the reduction rate of the spatial number density of photons per unit energy is simply given:

$$\mathcal{N}_{losses} = c\,\alpha_p\,P_\gamma^\pm(r, E_\gamma). \tag{4.33}$$

We remind that the photon distributions $P_\gamma^\pm$ include not only the upscattered photons, but the *curvature* ones as well.

On the other hand, the photon population in equation (4.32) also increases due to the γ-ray production taking place within the accelerating area. In specific, we can consider that $\mathcal{N}_{gain} = \mathcal{N}_{gain}^{IC} + \mathcal{N}_{gain}^{cur}$, since photons emitted by both radiative processes contribute to the term $\mathcal{N}_{gain}$ (i.e., inverse *Compton* scattering and *curvature* emission).

In order to estimate $\mathcal{N}_{gain}^{IC}$, we need first to write the number of particles per unit length:

$$\frac{dN^\pm}{dr} \approx \pm\frac{\rho^\pm}{e}. \tag{4.34}$$

Not all the particles, however, will upscatter soft photons with the same efficiency. We already know that an incident depends on the particle and soft photon energies as well as on the angle of collision. Consequently, we need to construct a relevant coefficient which then will give us the rate of scattered photons. This coefficient can be written as (Hirotani and Shibata, 1999):

$$\alpha_{IC}(E_\gamma, \Gamma_e) = \frac{1}{m_e c^2} \int\limits_{E_s^{min}}^{E_s^{max}} \sigma_{KN}\, \delta\left(\epsilon_\gamma - min[\Gamma_e^2 \epsilon_s, \Gamma_e]\right) \frac{dN_s}{dE_s}\, dE_s, \tag{4.35}$$

where $\epsilon_s = E_s/m_e c^2$, $\epsilon_\gamma = E_\gamma/m_e c^2$ are the normalized (i.e., in units of the electron rest mass) energies of soft and γ-ray photon, respectively, while σ_{KN}, dN_s/dE_s have been defined above. Finally, the term $\mathcal{N}_{gain}^{IC}$ is given by:

$$\mathcal{N}_{gain}^{IC} = \pm \alpha_{IC} \frac{\rho^\pm}{e m_e c^2}\, c \sqrt{1 - \frac{1}{\Gamma_e^2}}, \tag{4.36}$$

where we multiplied equation (4.34) with the particle velocity as well, so as to conform with the units of formula (4.32).

The term $\mathcal{N}_{gain}^{cur}$ can be expressed by considering the *curvature* power emitted from a single electron. We can approximate this using the *synchrotron* formula and assuming that the relativistic electron moves along a field line with curvature radius of the order of $R_c = \Gamma_e m_e c^2/(eB \sin\theta_c) \approx r_g$. Accordingly, the produced power (in units of $erg\ sec^{-1}\ Hz^{-1}$) can be written as (Rybicki and Lightmann, 1979):

$$p_{cur} = \frac{\sqrt{3}\, e^2}{r_g} \Gamma_e\, F\left(\frac{E_\gamma}{E_c}\right). \tag{4.37}$$

The function $F(x)$ in equation (4.37) is the *synchrotron* function:

$$F(x) = x \int\limits_x^\infty K_{\frac{5}{3}}(z) dz \approx x^{0.3} e^{-x}, \tag{4.38}$$

where $K_{5/3}$ is the modified *Bessel* function of the order of 5/3, and $x = E_\gamma/E_c$. The critical value E_c corresponds to the energy at which most of the emission takes place. It can be calculated using the following relation:

$$E_c = \frac{3}{4\pi}\,\frac{hc}{r_g}\,\Gamma_e^3. \tag{4.39}$$

Dividing now equation (4.37) by $h\epsilon_\gamma m_e c^2$ and multiplying simultaneously with the spatial number density of particles (i.e., $\pm\rho^\pm/e$), we obtain the total contribution of the *curvature* process in equation (4.32). Therefore, the increase rate of the spatial number density of photons per unit energy due to *curvature* radiation is:

$$\mathcal{N}_{gain}^{cur} = \pm\alpha_{cur}\, c\, \frac{\rho^\pm}{e\, m_e c^2}, \tag{4.40}$$

where the coefficient α_{cur} is given:

$$\alpha_{cur}(E_\gamma, \Gamma_e) = \frac{\sqrt{3}\, e^2}{h\, r_g \epsilon_\gamma c}\,\Gamma_e\, F\left(\frac{E_\gamma}{E_c}\right). \tag{4.41}$$

It is worth emphasizing at this point that the terms $\mathcal{N}_{gain}$ and $\mathcal{N}_{losses}$ should be always taken into account in respect with the particle motion.

Exploiting the above results, we can formulate the expressions that describe the distribution of γ-ray photons within the gap accelerator. For this purpose, if we substitute equations (4.33), (4.36) and (4.40) into formula (4.32), we find:

$$c\frac{dP_\gamma^+}{dr} = -a_{IC}\,\frac{\rho^-}{em_e c^2}\, c\sqrt{1-\frac{1}{\Gamma_e^2}} - \alpha_{cur}\, c\, \frac{\rho^-}{em_e\, c^2} - c\, a_p\, P_\gamma^+, \tag{4.42}$$

$$c\frac{dP_\gamma^-}{dr} = -a_{IC}\,\frac{\rho^+}{em_e c^2}\, c\sqrt{1-\frac{1}{\Gamma_e^2}} - \alpha_{cur}\, c\, \frac{\rho^+}{em_e\, c^2} + c\, a_p\, P_\gamma^-. \tag{4.43}$$

For the sake of clarity we mention again that the electrons moving away from the black hole due to the field direction are responsible for the photon distribution P_γ^+ (i.e., see equation 4.42). Correspondingly, the positrons which move towards the black hole produce the photon distribution P_γ^- (i.e., see equation 4.43).

Formulas (4.42) and (4.43) fully close the set of equations that determine the structure of the gap accelerator. To sum up, relations (4.9), (4.18), (4.29), (4.31), (4.42) and (4.43) form a well defined system of six equations with six unknown physical quantities (i.e., $\mathcal{E}_{||}^r$, Γ_e, ρ^+, ρ^-, P_γ^+ and P_γ^-). In the followings sections, we normalize the system and implement relevant boundary conditions.

4.2 Normalization of the system

Aiming to facilitate the numerical manipulation of the system, we normalize and write the equations of the gap without physical units. Accordingly, we rearrange the lengths by setting a new variable $\xi = r/r_g$ and define the charge densities by means of a characteristic value, that is $\rho_*^\pm = \rho^\pm/\rho_c$. The typical expression of the charge density that makes a *pulsar* magnetosphere *force-free* has been selected here to normalize the charge density. Therefore, we can write:

$$\rho_c = \frac{\Omega^F B_H}{2\pi c} \approx 2.69 \times 10^{-11} M_9^{-3/2} \dot{m}^{1/2}, \tag{4.44}$$

using that $\Omega^F = \Omega^H/2$, $\Omega^H = \alpha_s c^3/2GMr_H$ is the angular velocity of the black hole and $B_H = 10^5\, \dot{m}^{1/2} M_9^{-1/2}$ G is the magnetic field near the event horizon (Katsoulakos and Rieger, 2018). We also define the mass of the black hole $M_9 = M/10^9 M_\odot$ and the accretion rate $\dot{m} = \dot{M}/M_{Edd}$ given in billions of solar masses and *Eddington* units, respectively.

Implementing the above normalizations in *Gauss's* law, we rewrite equation (4.9) as follows:

$$\frac{d}{d\xi}\left(\frac{\mathcal{E}_{||}^{*r}}{\alpha_l}\right) = \rho_*^+ + \rho_*^- - \rho_{GJ}^* - A^* \left(\frac{\mathcal{E}_{||}^{*r}}{\alpha_l}\right), \tag{4.45}$$

where $\rho_{GJ}^* = \rho_{GJ}/\rho_c$, $A^* = r_g(1/\sqrt{|\gamma|})(d\sqrt{|\gamma|}/dr)$ and $\mathcal{E}_{||}^{*r} = \mathcal{E}_{||}^r/4\pi r_g \rho_c$ is the normalized parallel electric field component (i.e., the contravariant one).

More specifically, the expression of the *Goldreich-Julian* charge density ρ^*_{GJ} will be given by (i.e., equation 4.17):

$$\begin{aligned} \rho^*_{GJ} = -\frac{(1-\omega/\Omega^F)\,\cos\theta}{\alpha_l} \Bigg[& \frac{2}{\rho_*^2} - 2\,\alpha_s^{*2}\,\frac{\Delta_*}{\rho_*^2\,\Sigma_*^2}\,\sin^2\theta + \\ & +2\,\alpha_s^{*2}\,\frac{1}{\rho_*^4}\,\sin^2\theta - \frac{4\,\alpha_s^{*3}}{(\Omega^F-\omega)_*}\,\frac{\xi\,\Delta_*}{\rho_*^2\,\Sigma_*^4}\,\sin^2\theta \Bigg], \end{aligned} \tag{4.46}$$

and the term A^* also by (i.e., equation 4.10):

$$A^* = \frac{\xi}{\rho_*^2} + \frac{1}{\Sigma_*^2}\left[2\,\xi\,(\xi^2 + a_s^{*2}) - a_s^{*2}\,\sin^2\theta\,(\xi-1)\right] - \frac{(\xi-1)}{\Delta_*}, \tag{4.47}$$

where we define the quantities $\rho_*^2 = \rho^2/r_g^2$, $\Sigma_*^2 = \Sigma^2/r_g^4$, $\alpha_s^* = \alpha_s/r_g$, $\Delta_* = \Delta/r_g^2$ and finally $(\Omega^F-\omega)_* = (\Omega^F-\omega)(r_g/c)$. Alternatively, one can note that the set of the equations is written in units of $r_g = c = 1$.

Normalizing formula (4.18) one finds that the equation of motion is:

$$\frac{d\Gamma_e}{d\xi} = -\mathcal{C}_1\mathcal{E}_{||}^{*r} - \mathcal{C}_2\mathcal{F}(\Gamma_e) - \mathcal{C}_3\Gamma_e^4, \tag{4.48}$$

where, we estimate the non-dimensional quantities $\mathcal{C}_1$ and $\mathcal{C}_3$ as:

$$\mathcal{C}_1 = \frac{4\pi\,e\,r_g^2\,\rho_c}{m_e\,c^2} \approx 4.32\times10^{15}M_9^{1/2}\dot{m}^{1/2}, \tag{4.49}$$

and:

$$\mathcal{C}_3 = \frac{2\,e^2}{3\,r_g\,m_e\,c^2} \approx 0.13\times10^{-26}M_9^{-1}. \tag{4.50}$$

The *Compton* term in expression (4.48) is $\mathcal{C}_2\mathcal{F}(\Gamma_e) = (r_g/m_ec^2)(P_{IC}/c)$. It has been already mentioned above that this term is approximated by a fifth order polynomial equation to simplify the numerical treatment. Hence, we multiply the data points of the polynomial with the factor r_g/m_ec^2, in order to normalize the *Compton* term.

We continue now the procedure of normalization, adjusting the electron and positron distributions. Accordingly, equation (4.29) gives:

$$\frac{d}{d\xi}\left[(\rho_*^- - \rho_*^+)\left(1-\frac{1}{\Gamma_e^2}\right)^{\frac{1}{2}}\right] = 0, \tag{4.51}$$

where it is evident that:

$$(\rho_*^- - \rho_*^+)\left(1-\frac{1}{\Gamma_e^2}\right)^{\frac{1}{2}} = \frac{J_o}{c\,\rho_c} = J_o^*. \tag{4.52}$$

The constant parameter J_o^* is the dimensionless current density which corresponds to the global magnetospheric current. We do emphasize here that J_o^* is normalized via the fixed value ρ_c of equation (4.44) and not via the relativistic *Goldreich-Julian* charge density which varies with ξ.

Moreover, equation (4.31), which also describes the lepton population within the gap accelerator, becomes:

$$\frac{d}{d\xi}\left[(\rho_*^+ + \rho_*^-)\left(1-\frac{1}{\Gamma_e^2}\right)^{\frac{1}{2}}\right] = -2\int_0^\infty a_p^*(P_{\gamma^*}^+ + P_{\gamma^*}^-)d\epsilon_\gamma, \tag{4.53}$$

where we set $a_p^* = r_g\,a_p$ and $P_{\gamma^*}^{\pm} = (e\,m_ec^2/\rho_c)\,P_\gamma^{\pm}$ represent the outcoming/incoming normalized γ-ray photons.

Formula (4.53) captures the information for the lepton distribution which is injected into the gap due to γ-ray photon annihilation. We see that both the high-energy photons $P_{\gamma^*}^{\pm}$ and the coefficient a_p^*, which also depends on the energy ϵ_γ (i.e., see for equation 4.26), are found in the integral causing additional numerical difficulties. In order to overcome these challenges we approximate the integral of equation (4.53) with a sum dividing the γ-ray energy band into many finite energy bins[10]. Hence, the right-hand side of

---

[10] In the next sections, we present solutions of the gap structure applying 80 energy bins in equation (4.53).

equation (4.53) becomes (Hirotani and Okamoto, 1998):

$$
\begin{aligned}
-2\int_{0}^{\infty} a_p^*(P_{\gamma^*}^+ + P_{\gamma^*}^-)d\epsilon_\gamma = -2\Bigg[\int_{\epsilon_\gamma^{(1)}}^{\epsilon_\gamma^{(2)}} a_p^*(P_{\gamma^*}^+ + P_{\gamma^*}^-)d\epsilon_\gamma + \\
+\int_{\epsilon_\gamma^{(2)}}^{\epsilon_\gamma^{(3)}} a_p^*(P_{\gamma^*}^+ + P_{\gamma^*}^-)d\epsilon_\gamma + ... + \int_{\epsilon_\gamma^{(i-1)}}^{\epsilon_\gamma^{(i)}} a_p^*(P_{\gamma^*}^+ + P_{\gamma^*}^-)d\epsilon_\gamma + ... \\
... + \int_{\epsilon_\gamma^{(m-1)}}^{\epsilon_\gamma^{(m)}} a_p^*(P_{\gamma^*}^+ + P_{\gamma^*}^-)d\epsilon_\gamma\Bigg] = -2\sum_{i=2}^{m}\int_{\epsilon_\gamma^{(i-1)}}^{\epsilon_\gamma^{(i)}} a_p^*(P_{\gamma^*}^+ + P_{\gamma^*}^-)d\epsilon_\gamma = \\
= -2\sum_{i=2}^{m}\left[\int_{\epsilon_\gamma^{(i-1)}}^{\epsilon_\gamma^{(i)}} a_p^* P_{\gamma^*}^+ d\epsilon_\gamma + \int_{\epsilon_\gamma^{(i-1)}}^{\epsilon_\gamma^{(i)}} a_p^* P_{\gamma^*}^- d\epsilon_\gamma\right].
\end{aligned}
\tag{4.54}
$$

We further approximate the integrals in equation (4.54) setting:

$$
\int_{\epsilon_\gamma^{(i-1)}}^{\epsilon_\gamma^{(i)}} a_p^*\, P_{\gamma^*}^\pm\, d\epsilon_\gamma \approx a_{p,i}^*\, \mathcal{P}_{*,i}^\pm, \tag{4.55}
$$

where we interpret the above approximation as:

$$
a_{p,i}^* \approx a_p^*\left(\frac{\epsilon_\gamma^{(i-1)} + \epsilon_\gamma^{(i)}}{2}\right), \qquad \mathcal{P}_{*,i}^\pm = \int_{\epsilon_\gamma^{(i-1)}}^{\epsilon_\gamma^{(i)}} P_{\gamma *}^\pm\, d\epsilon_\gamma, \tag{4.56}
$$

namely, we use the mean value $a_{p,i}^*$ of the coefficient and the γ-ray photon distributions $\mathcal{P}_{*,i}^\pm$ (integrated over energy) for each energy bin. The higher the number of energy bins, the more accurate the estimate of the integral becomes (see equation 4.53). After these rearrangements we are able to re-express formula (4.53) as:

$$\frac{d}{d\xi}\left[(\rho_*^+ + \rho_*^-)\left(1-\frac{1}{\Gamma_e^2}\right)^{\frac{1}{2}}\right] = -2\sum_{i=1}^{m} a_{p,i}^*(\mathcal{P}_{*,i}^+ + \mathcal{P}_{*,i}^-). \tag{4.57}$$

The remaining equations that must be normalized are the *Boltzmann* ones of the outcoming/incoming γ-ray photons. Including the characteristic length ξ and the fiducial charge density ρ_c in equations (4.42) and (4.43) one obtains:

$$\pm\frac{dP_{\gamma^*}^{\pm}}{d\xi} = \mp\alpha_{IC}^*\,\rho_*^{\mp}\sqrt{1-\frac{1}{\Gamma_e^2}} \mp \alpha_{cur}^*\,\rho_*^{\mp} - a_p^*\,P_{\gamma^*}^{\pm}, \tag{4.58}$$

where we set $\alpha_{IC}^* = r_g\,\alpha_{IC}$ and $\alpha_{cur}^* = r_g\,\alpha_{cur}$. In order now to adjust the magnitudes of equation (4.58) with the ones of (4.57) we integrate the above relation over energy and find:

$$\pm\frac{d}{d\xi}\int\limits_{\epsilon_\gamma^{(i-1)}}^{\epsilon_\gamma^{(i)}} P_{\gamma^*}^{\pm}d\epsilon_\gamma = \mp\int\limits_{\epsilon_\gamma^{(i-1)}}^{\epsilon_\gamma^{(i)}}\left(\alpha_{IC}^*\sqrt{1-\frac{1}{\Gamma_e^2}}+\alpha_{cur}^*\right)\rho_*^{\mp}d\epsilon_\gamma - \int\limits_{\epsilon_\gamma^{(i-1)}}^{\epsilon_\gamma^{(i)}} a_p^*P_{\gamma^*}^{\pm}d\epsilon_\gamma. \tag{4.59}$$

Using the approximations of (4.55) and (4.56) we can write:

$$\frac{d\mathcal{P}_{*,i}^+}{d\xi} = -\alpha_{IC,i}^*\,\rho_*^-\sqrt{1-\frac{1}{\Gamma_e^2}} - \alpha_{cur,i}^*\,\rho_*^- - a_{p,i}^*\,\mathcal{P}_{*,i}^+, \tag{4.60}$$

$$\frac{d\mathcal{P}_{*,i}^-}{d\xi} = -\alpha_{IC,i}^*\,\rho_*^+\sqrt{1-\frac{1}{\Gamma_e^2}} - \alpha_{cur,i}^*\,\rho_*^+ + a_{p,i}^*\,\mathcal{P}_{*,i}^-, \tag{4.61}$$

where the coefficient $a^*_{IC,i}$ and $a^*_{cur,i}$ are given by:

$$a^*_{IC,i} = \int_{\epsilon_\gamma^{(i-1)}}^{\epsilon_\gamma^{(i)}} a^*_{IC}\, d\epsilon_\gamma, \qquad a^*_{cur,i} = \int_{\epsilon_\gamma^{(i-1)}}^{\epsilon_\gamma^{(i)}} a^*_{cur}\, d\epsilon_\gamma. \tag{4.62}$$

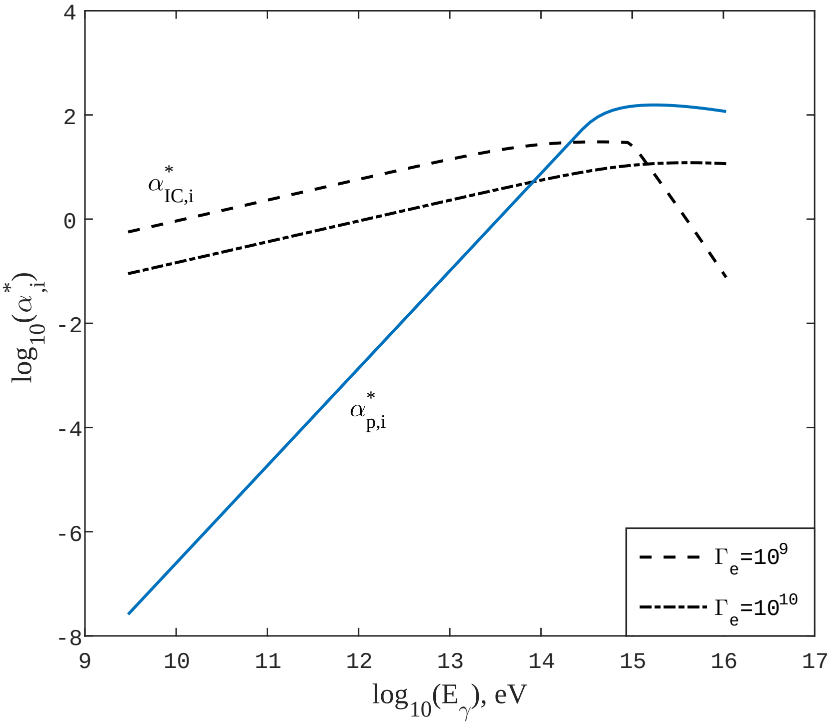

Figure 4.2: Graphical illustration of the normalized coefficients $a^*_{p,i}$ (blue line) and $a^*_{IC,i}$ (black lines). The dashed and dashed-dot lines correspond to particle Lorentz factors of $\Gamma_e = 10^9$ and $\Gamma_e = 10^{10}$, respectively. The parameters used are: $M_9 = 1.0$, $\alpha^*_s = 1.0$, $\dot{m} = 10^{-4.0}$ and $\theta = 30^o$.

In figure (4.2), the non-dimensional coefficients $a^*_{p,i}$ (blue line) and $a^*_{IC,i}$ (black lines) are depicted[11]. The γ-rays are assumed to range from energy $E_\gamma \sim 10^9$ eV to energy $E_\gamma \sim 10^{16}$ eV. Consequently, γ-rays can annihilate with soft photons over the whole spectral range of the ADAF emission. Given that the coefficient $a^*_{IC,i}$ also depends on the particle's *Lorentz* factor, we

---

[11] In fact, the figure illustrates both coefficients for each energy bin. The optical impression of continuous lines is related to the high number of energy cells used. The coefficient $a^*_{cur,i}$ is not depicted in figure (4.2) since it is small and does not contribute much to the pair cascade.

present two characteristic cases for $\Gamma_e = 10^9$ and $\Gamma_e = 10^{10}$ with the dashed and dashed-dot line, respectively[12]. For the accretion rate that we use in this example ($\dot{m} = 10^{-4}$) the coefficients become comparable approximately at energies $E_\gamma \sim 100$ TeV. In addition, both coefficients show a break roughly beyond these energies. This happens due to the transition from the *Compton* to the steep *synchrotron* part in the spectrum of the ADAF. We note that the coefficient $a^*_{IC,i}$ is approximated with a polynomial equation in the numerical code owing to the simultaneous dependence on the energy and the *Lorentz* factor (i.e., equations 4.60 and 4.61).

We summarize here, that relations (4.45), (4.48), (4.51), (4.57), (4.60) and (4.61) form a system of "$4 + 2m$" equations that govern the physics of the gap accelerator. Imposing plausible boundary conditions we then integrate the system numerically and determine the structure of the gap, that is the radial distributions of $\mathcal{E}^{*r}_{||}$, Γ_e, ρ^+_*, ρ^-_*, $\mathcal{P}^+_{*,i}$ and $\mathcal{P}^-_{*,i}$.

4.3 The boundary conditions

The aforementioned system of equations constitutes a *Boundary Value Problem* (BVP), since conditions which reflect the gap physics have to be satisfied at the inner and the outermost gap positions[13].

Typical boundary conditions are discussed in Hirotani and Okamoto (1998); Levinson and Segev (2017). Accordingly, we impose that the parallel component of the electric field vanishes at both boundaries. Hence, we have:

$$\mathcal{E}^{*r}_{||}\Big|_{\xi_1} = 0, \qquad \mathcal{E}^{*r}_{||}\Big|_{\xi_2} = 0. \tag{4.63}$$

The emergence of a parallel electric field, which is the result of a charge deficit in the region, is terminated at $\xi_{1,2}$ ensuring *force-freeness* beyond the gap boundaries. Therefore, particle acceleration is no longer possible at the gap boundaries[14]:

$$\Gamma_e\big|_{\xi_1} = 1, \qquad \Gamma_e\big|_{\xi_2} = 1. \tag{4.64}$$

---

[12] We remind of expectations for terminal *Lorentz* factors up to $\Gamma_e \approx 10^{10}$ in the accelerating zone (e.g., see chapter 3.1.3).

[13] We refer to ξ_1 for the inner boundary of the gap and ξ_2 for the outer one.

[14] The numerical solutions are not very sensitives to this condition.

Exploiting now equation (4.52) and provided that the electric field guides positrons towards the event horizon and electrons outwards, some authors have assumed (Hirotani and Okamoto, 1998):

$$\rho_*^-\big|_{\xi_1} = 0, \qquad \rho_*^+\big|_{\xi_1} = -\frac{J_o^*}{\sqrt{1-\frac{1}{\Gamma_e^2}}}, \tag{4.65}$$

at ξ_1 boundary and:

$$\rho_*^+\big|_{\xi_2} = 0, \qquad \rho_*^-\big|_{\xi_2} = \frac{J_o^*}{\sqrt{1-\frac{1}{\Gamma_e^2}}}, \tag{4.66}$$

at ξ_2[15]. For such a choice, only positrons are present and travel through the inner boundary, and only electrons at the outer one. Since this is somewhat artificial, we relax conditions (4.65) and (4.66) in our study giving the possibility for some charge injection of both species at the gap boundaries. Finally, *Hirotani* and collaborators have also considered in a series of papers that high energy γ-ray photons are not injected through both gap boundaries (Hirotani and Okamoto, 1998; Hirotani and Shibata, 1999; Hirotani et al., 2017). Consequently, we can write:

$$\mathcal{P}_{*,i}^+\Big|_{\xi_1} = 0, \qquad \mathcal{P}_{*,i}^-\Big|_{\xi_2} = 0, \tag{4.67}$$

namely, the gap accelerator is isolated by any other source of high energy photons in the close vicinity of the black hole. Even if the particle acceleration terminates beyond the boundaries, the electromagnetic cascade remains active for many gravitational radii. According to this line of reasoning, we may expect some part of the high energy photons produced outside the gap to get injected into it at least through the outer boundary ξ_2. Therefore,

---

[15] We note that the global magnetospheric current J_0^* takes negative value in our convention (where the electric field points towards the black hole), resulting in positive $\rho_*^+|_{\xi_1}$ and negative $\rho_*^-|_{\xi_2}$ charge densities in equations (4.65) and (4.66), respectively.

we also relax the condition of formula (4.67) and accept any choice of photon values $\mathcal{P}^{\pm}_{*,i}\big|_{\xi_1,\xi_2}$ that ultimately produce charge density lower than the *Goldreich-Julian* one along the whole extension of the gap.

For clarity, we note that we integrate the set of equations imposing conditions (4.63), (4.64) and demanding the resulting amount of charges to be less than the *Goldreich-Julian* charge density (i.e., $|\rho_e| = |\rho_*^+ + \rho_*^-| \leq |\rho^*_{GJ}|$), irrespectively whether conditions (4.65), (4.66) and (4.67) are fully satisfied.

Existence of steady gap solution

It has been already commented above (chapter 2) that the *Goldreich-Julian* charge density changes sign across the null surface (from positive to negative moving outwards), where $\Omega^F = \omega$ and $\rho_{GJ} = 0$. The real charge distribution resulting from the integration of the system would be around the *Goldreich-Julian* one and its divergence from it would give the parallel electric field (see equation 4.6). Provided now that the strength of the electric field is negative in our convention (i.e., it points towards the black hole), we qualitatively expect that it starts to decrease from zero at boundary ξ_1, then reaches a minimum at a certain distance, in which $\rho_e \approx \rho_{GJ}$, before increase again up to zero at boundary ξ_2. Therefore, the *Gauss's* law at the inner boundary has to be:

$$\frac{d}{d\xi}\left(\frac{\mathcal{E}^{*r}_{||}}{\alpha_l}\right)\bigg|_{\xi_1} = \rho_*^+ + \rho_*^- - \rho^*_{GJ}\,\big|_{\xi_1} \leq 0, \tag{4.68}$$

while at the outer boundary:

$$\frac{d}{d\xi}\left(\frac{\mathcal{E}^{*r}_{||}}{\alpha_l}\right)\bigg|_{\xi_2} = \rho_*^+ + \rho_*^- - \rho^*_{GJ}\,\big|_{\xi_2} \geq 0, \tag{4.69}$$

where we set that $A^*(\mathcal{E}^{*r}_{||}/\alpha_l) = 0$ in equation (4.45) imposing the condition of (4.63). We emphasize here that both formulas (4.68) and (4.69) ensure that the charge density at the boundaries is not super-critical, that is $|\rho_e| \leq |\rho_{GJ}|$, since the *Goldreich-Julian* density is positive at ξ_1 and negative at ξ_2[16].

---

[16] The characteristic "brim" at the boundaries in the distribution of the electric field appears for the case where $|\rho_e| = |\rho_{GJ}|$ (Hirotani and Okamoto, 1998; Hirotani et al., 2017).

Assuming now that electron injection takes place across boundary ξ_1 we can write it as a fraction of the positron charge density:

$$\rho_*^-\big|_{\xi_1} = -n_e\ \rho_*^+\big|_{\xi_1}\,, \tag{4.70}$$

where we have that $0 \leq n_e < 1$. Finally, relation (4.68) via the definition of the global magnetospheric current (equation 4.52) and formula (4.70) gives:

$$\left(\frac{n_e - 1}{n_e + 1}\right) \left.\frac{Jo^*}{\sqrt{1 - \frac{1}{\Gamma_e^2}}}\right|_{\xi_1} \leq \rho_{GJ}^*|_{\xi_1}\,. \tag{4.71}$$

From equation (4.71) we have that the inner boundary ξ_1 is determined by the value of the current J_o^* and the amount of electrons n_e which depends on the accretion rate $\dot{m}$ (see chapter 3). Implementing the boundary condition (4.65) for convenience and keeping the equality in relation (4.71) we are able to estimate the innermost boundary[17] by solving the following algebraic equation:

$$-\left.\frac{Jo^*}{\sqrt{1 - \frac{1}{\Gamma_e^2}}}\right|_{\xi_1} = \rho_{GJ}^*|_{\xi_1}\,. \tag{4.72}$$

In a similar way, we manipulate relation (4.69) and find:

$$\left(\frac{1 - n_p}{n_p + 1}\right) \left.\frac{Jo^*}{\sqrt{1 - \frac{1}{\Gamma_e^2}}}\right|_{\xi_2} \geq \rho_{GJ}^*|_{\xi_2}\,, \tag{4.73}$$

where $0 \leq n_p < 1$ is the fraction of positrons at outer boundary ξ_2:

$$\rho_*^+\big|_{\xi_2} = -n_p\ \rho_*^-\big|_{\xi_2}\,. \tag{4.74}$$

---

[17] The innermost boundary ξ_1 relative to the radial distance where ρ_{GJ} becomes zero.

Imposing $n_p = 0$ for convenience and keeping the equality in formula (4.73) we estimate the radial range of the outer boundary ξ_2 from the following algebraic equation:

$$\left.\frac{Jo^*}{\sqrt{1-\frac{1}{\Gamma_e^2}}}\right|_{\xi_2} = \rho^*_{GJ}|_{\xi_2}\,. \tag{4.75}$$

In figure (4.3) below, we depict the radial distribution of the *Goldreich-Julian* charge density (black solid line), the left-hand side of equation (4.72) (dashed lines) and the left-hand side of equation (4.75) (dash-dotted lines) for three different values of the current. Specifically, we illustrate the cases of $J_o^* = -0.1, -0.2, -0.4$ with blue, red and green color respectively.

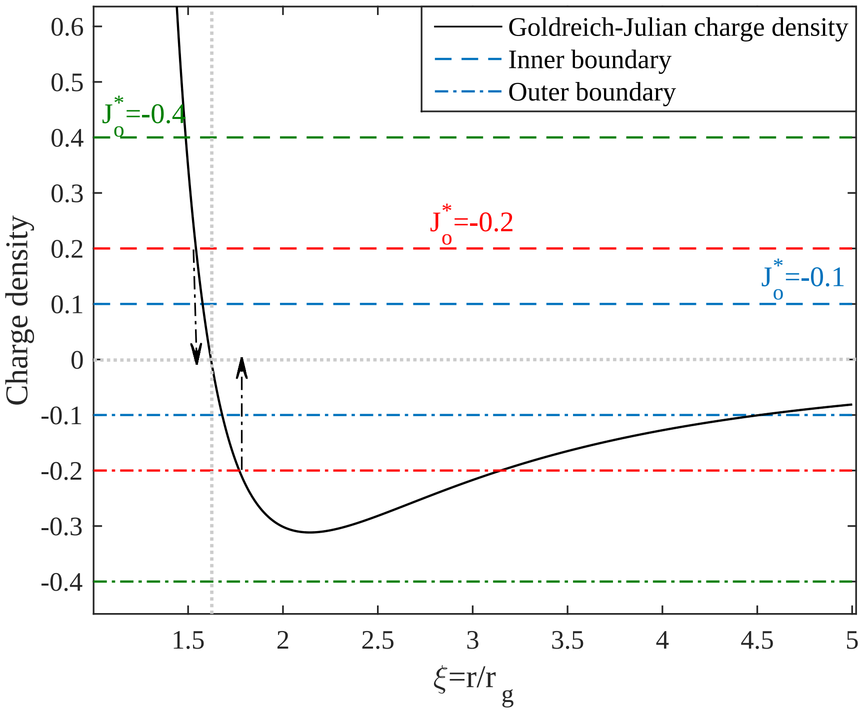

Figure 4.3: Graphical illustration of the *Goldreich-Julian* charge density (black solid line), the left-hand side of equation (4.72) (dash lines) and the left-hand side of equation (4.75) (dash-dot lines) for three different values of the current: $J_o^* = -0.1, -0.2, -0.4$ given in blue, red and green color, respectively.

The intersection points of the straight lines with the *Goldreich-Julian* charge density satisfy equations (4.72) and (4.75) and give the innermost boundary ξ_1 and the range of the outer boundary ξ_2. Since we investigate gaps across the null surface, we always require the boundary ξ_1 to be below the radius at which ρ_{GJ} becomes zero and the boundary ξ_2 to be beyond of it. Generally, inequalities (4.71) and (4.73) hold for each possible ξ_1 and ξ_2. Hence, any numerical method would constrain the search of the inner gap boundary in the radial interval from r_H up to ξ_1^{max} (i.e., see the arrow pointing downwards) and the search of the outer one in the space from ξ_2^{min} (i.e., see the arrow pointing upwards) up to ξ_2^{max} (i.e., see the second intersection point, for instance, of the red dash-dotted line).

Practically, we expect that boundary ξ_2 would be closer to ξ_2^{min} than to ξ_2^{max} [18]. If this is indeed the case, we conclude that the higher the current value is, the larger gap extension is for a given accretion rate (e.g., see how the arrows would vary from $J_o^* = -0.1$ to $J_o^* = -0.2$). No abrupt change in the gap width is, however, expected for variations of the current, due to the smooth decrease of the *Goldreich-Julian* charge density around the null surface.

Finally, for a current $J_o^* = -0.4$ we obtain the most interesting result of figure (4.3). Given that there is not any point which intersects with the *Goldreich-Julian* charge density (dash-dotted green line), the radial range of the gap boundary ξ_2 cannot be properly defined. Hence, no steady gap solution exists beyond a certain current value. This agrees with similar findings by Levinson and Segev (2017). In this paper, the authors find that steady gap solutions exist only under restrictive conditions (e.g., small magnetospheric current and extremely small soft photon luminosity) that may not apply to realistic astrophysical environments. We do emphasize, however, that our result depends on the applicability of conditions (4.65) and (4.66).

As we have shown above, the existence of the outer gap boundary ξ_2 and consequently the existence of a steady gap solution in (1D) depends on the global magnetospheric current J_o^* as well as on the positron fraction n_p at the boundary and not much on the geometry of the electric field (e.g., see relation 4.73). In figure (4.4), the radial range of the possible boundary ξ_2 is illustrated as function of the global magnetospheric current J_o^* and provided for four different fractions of positron injection (i.e., $n_p = 0.0, 0.2, 0.4$ and 0.6 given in black, blue, red and green colors, respectively). Dashed lines represent ξ_2^{min} while solid lines depict ξ_2^{max}. Evidently, we are able to define the radial range ξ_2 for a given value of the current only if the positron injection is sufficiently large (i.e., see for dotted grey line). For instance, a steady gap solution cannot be found when $n_p = \rho_*^+/\rho_*^- = 0$ and $J_o^* < -0.3$. On the con-

---

[18] The upper-limit ξ_2^{max} defines extended gap widths which are mostly related to low accretion rates inefficient to sustain a steady electromagnetic cascade.

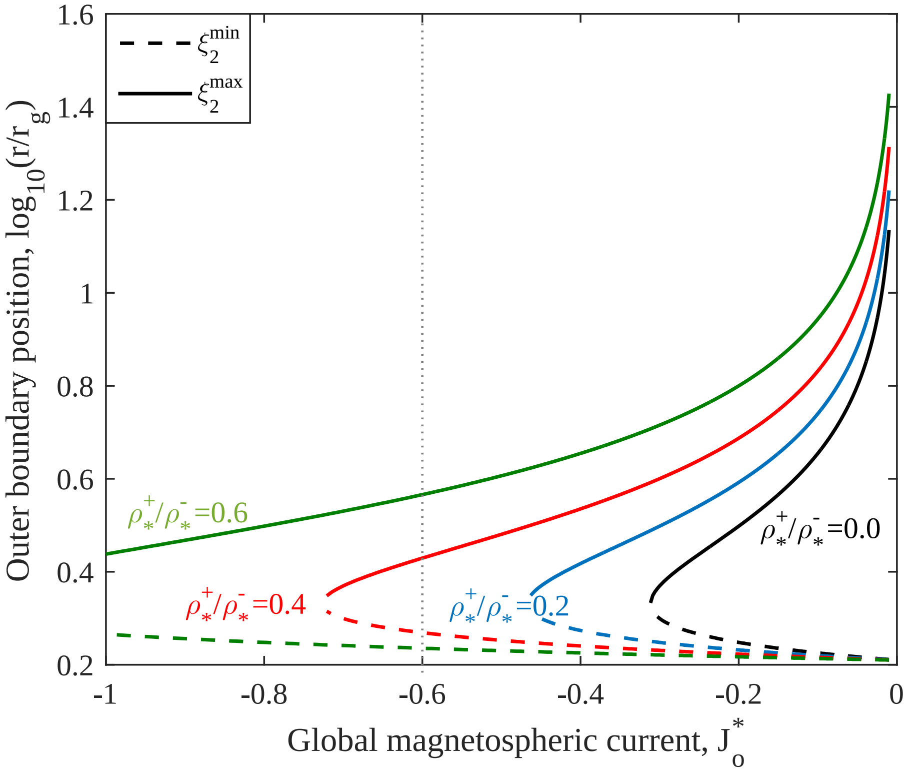

Figure 4.4: Graphical representation of the outer boundary ξ_2 as function of the global magnetospheric current J_o^* and provided for four different fractions of positron injection: $\rho_*^+/\rho_*^- = 0.0, 0.2, 0.4$ and 0.6 given in black, blue, red and green colors, respectively.

trary, steady gaps seem to be sustainable for $J_o^* < -0.5$ only if we relax condition (4.66) and permit the injection of positrons at the outer gap boundary. In a recent review paper *Hirotani* has argued that the weakness of the stationary gap model can be overcome if one incorporates the (2D) electrodynamic structure (Hirotani, 2018). Hence, further research in this regard will be required in the future.

4.4 Numerical integration of the system

In order to solve the system and obtain proper solutions of the gap structure we adopt the so-called *shooting* method for the numerical integration of the equations (Press et al., 2007). Specifically, we start integrating the equations from ξ_1^{max} up to a candidate ξ_2 (i.e., for a given accretion rate $\dot{m}$ and global current J_0^*), implementing the conditions at the inner boundary as initial ones. Then, we check if the boundary conditions at ξ_2 are satisfied. Since we have relaxed conditions (4.65), (4.66) and (4.67) in our approach, we iterate the integration changing the charge and photon injection. As it has been discussed above, we expect that a normal solution would satisfy relations (4.63) and (4.64) at both boundaries and that the condition, $|\rho_e| \leq |\rho^*_{GJ}|$, will be ensured along the gap dimension. If, nevertheless, a solution is not achieved for any choice of charge and photon injection, we change ξ_1 moving towards the horizon and integrate again the set of equations. Finally, if no solution is found through all possible ξ_1, we change the value of the current and subsequently the accretion rate until a gap solution can be found.

In figure (4.5) below, the *Goldreich-Julian* charge density (blue line), the total term, $\rho^*_{GJ} + A^*(\mathcal{E}^{*r}_{||}/\alpha_l)$, of equation (4.45) (dashed grey line)[19] and a proper solution (black line) resulting after consecutive numerical integrations (grey lines) are illustrated. In addition, the point where the *Goldreich-Julian* charge distribution becomes zero (i.e, hereafter *null point*) is indicated by the intersection of the dashed black lines.

Imposing the estimated charge density to be less than the *Goldreich-Julian* charge distribution, we require our solution to pass through the *null point*, that is $\rho_e|_{\xi_{null}} = \rho_{GJ}|_{\xi_{null}} = 0$. With such a choice, however, we reduce strongly the number of the acceptable gap solutions. If the charge density, on the other hand, is not fixed relative to the *null point*, the gaps would locally present higher charge density than the *Goldreich-Julian* one (Hirotani and Pu, 2016). Indeed, *Levinson* and *Segev* recently published (1D) steady gap solutions which show this property (Levinson and Segev, 2017).

According to their results (see, for example, their figure (2) for current value $N^r_o = 0.1$), the total charge density is positive in the same spatial range where the *Goldreich-Julian* one is negative (i.e., typically, from 2.0 r_g up to 2.5 r_g). Hence, the subtraction, $(\rho_e - \rho_{GJ})$, would give positive sign in their equation (6) (i.e., $\partial_\xi \Phi_E > 0$; see the upper-left plot of figure 2), which suggests a charge amount close to the *null* point in excess, that is $|\rho_e| > |\rho_{GJ}|$. From their figure (2), a shift in the minimum of the electric flux function is also evident due to changes in the global current. We interpret here this behaviour with the grey lines in figure (4.5) (i.e., unfixed *null point*). As it can be seen, the choice of such solution tends to under/over-estimate the gap width depending on the position of the electric field extremum. Notably, the gap size is underestimated when the minimum of the parallel electric field component occurs before the *null point* and is overestimated in the case where the minimum is beyond of it.

Aiming to overcome these difficulties, we consider that each gap realisation should maintain a charge density below or (at maximum) equal to

---

[19] As it can be seen in figure (4.5) the *general relativistic* term, $A^*(\mathcal{E}^{*r}_{||}/\alpha_l)$, does not contribute much to equation (4.45).

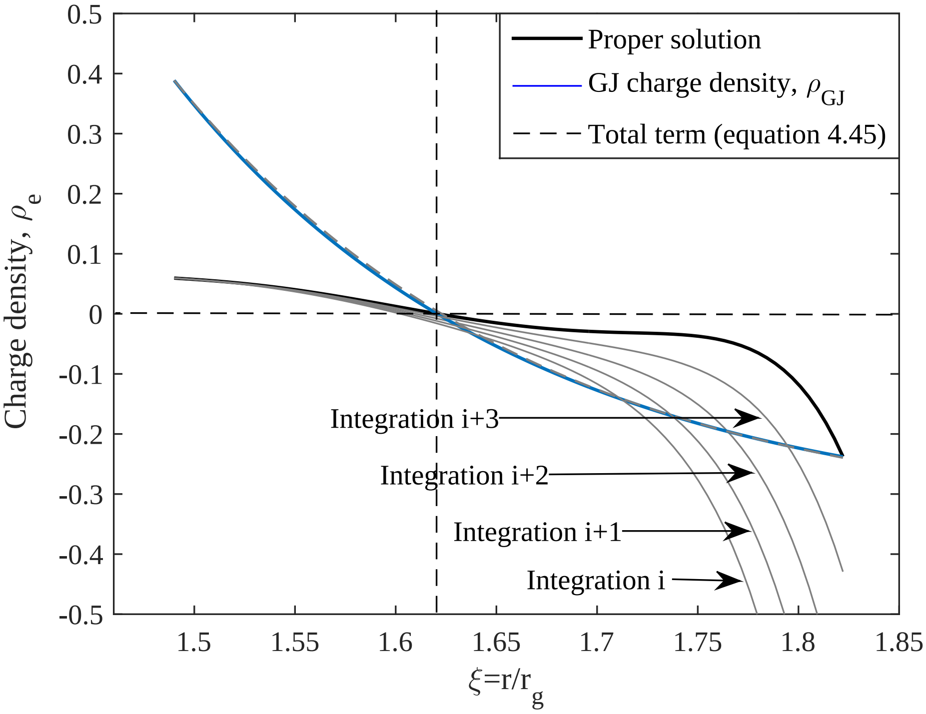

Figure 4.5: Graphical representation of the numerical method that we followed in order to find solutions of the gap structure. In the figure, we illustrate the *Goldreich-Julian* charge density (blue line), the total term, $\rho^*_{GJ} + A^*(\mathcal{E}^{*r}_{||}/\alpha_l)$, of equation (4.45) (dashed grey line) and a proper solution (black line) which results after consecutive numerical integrations (grey lines).

the *Goldreich-Julian* one (i.e., the black solid line in figure 4.5). This argument appears supported, if one thinks of the time-dependent problem. In the case in which the electromagnetic cascade cannot locally provide a sufficient amount of charges, steady gaps can be established in the magnetosphere. On the contrary, in the case of an efficient cascade which locally attributes more pairs than the critical value, the electric field will redistribute the charges adjusting their density and minimizing the gap size. The surplus of charges, on the one hand, and their inherent tendency of adjustment to the critical value, on the other, will cause dynamical oscillations to the gap making its stability rather unlikely (Levinson and Cerutti, 2018).

4.5 The structure of the gap accelerator

Having formulated the relevant equations that govern the magnetospheric gap accelerator and described the appropriate boundary conditions, we can now apply the numerical method explained above, so as to determine solutions of the (1D) steady gap. In the following subsections, we present the structure of the gap, namely, the radial distribution of the physical quantities as obtained by solving the system (i.e., the parallel electric field, the *Lorentz* of the particles, the charge density). In order to study the physics of the mechanism, explore its limits and compare with observations, we present below gap solutions for different values of the accretion rate and global magnetospheric current.

4.5.1 Gap solutions: Fixed accretion rate

In figure (4.6) below, we present the distribution of the parallel electric field component $\mathcal{E}_{||}^{*r}$ and, in figure (4.7), the *Lorentz* factor Γ_e of the injected pairs. More specifically, we provide gap solutions which correspond to three different values of the current parameter, namely $J_o^* = -0.005$, $J_o^* = -0.157$ and $J_o^* = -0.297$ shown with black, red and green color, respectively. In our setups, we have considered that the solutions address gap regions which are embedded into the magnetosphere of a fast rotating ($\alpha_s^* = 1.0$) supermassive ($M = 10^9 M_\odot$) black hole.

Table 4.1: Estimate of the gap extension, the voltage difference through the accelerator and the total gap power for the (1D) steady gap solutions described in the text. The parameters we use are: $M_9 = 1.0$, $\alpha_s^* = 1.0$, $\dot{m} = 10^{-5.0}$ and $\theta = 30^o$. The gap luminosity is calculated via equation (3.34). For the parameters used here, the *Blandford-Znajek* power is given by $l_{BZ} = 2 \times 10^{43}\ erg\,sec^{-1}$ (see equation 3.14).

Global Current $J_o^* = J_o/c\rho_c$	*Gap Size* (h/r_g)	*Voltage Drop* $\times 10^{16}$ Volts	*Gap Power* $\times 10^{40}\ erg\,sec^{-1}$
-0.005	0.2550	1.7	2.0
-0.157	0.2879	2.1	2.5
-0.29725	0.3321	2.5	2.9

It is obvious in figure (4.6) that the gap extension enlarges as the amount of the global magnetospheric current increases. Roughly speaking, we obtain gap sizes smaller than 1/3 of the gravitational radius for the parameters that we have chosen in this series of solutions (see table 4.1 for details). Furthermore, all electric field solutions reach their extremum at the *null point* as the dashed grey line indicates. From figure (4.7)[20], we find that the maximum *Lorentz* factors ($\Gamma_e \sim 10^9$) are achieved slightly beyond the mini-

---

[20] The inner boundaries of the solutions are the same with those of figure (4.6). Since the *Lorentz* factor approaches to unity at the boundaries, we only depict the distribution of the higher order of magnitude.

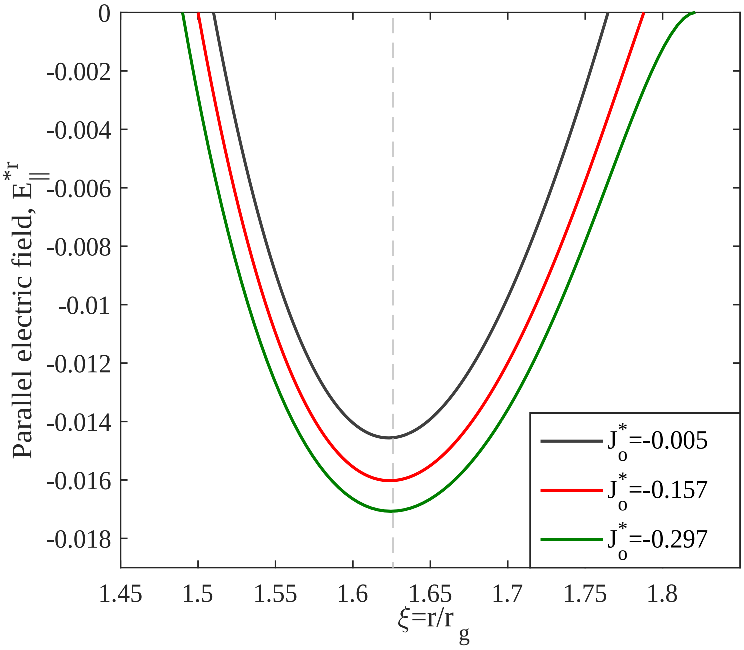

Figure 4.6: The normalized distribution of the parallel electric field component $\mathcal{E}_{||}^{*r}$ shown for current values $J_o^* = -0.005$ (black line), $J_o^* = -0.157$ (red line) and $J_o^* = -0.297$ (green line). The parameters used are: $M_9 = 1.0$, $\alpha_s^* = 1.0$, $\dot{m} = 10^{-5.0}$ and $\theta = 30^o$.

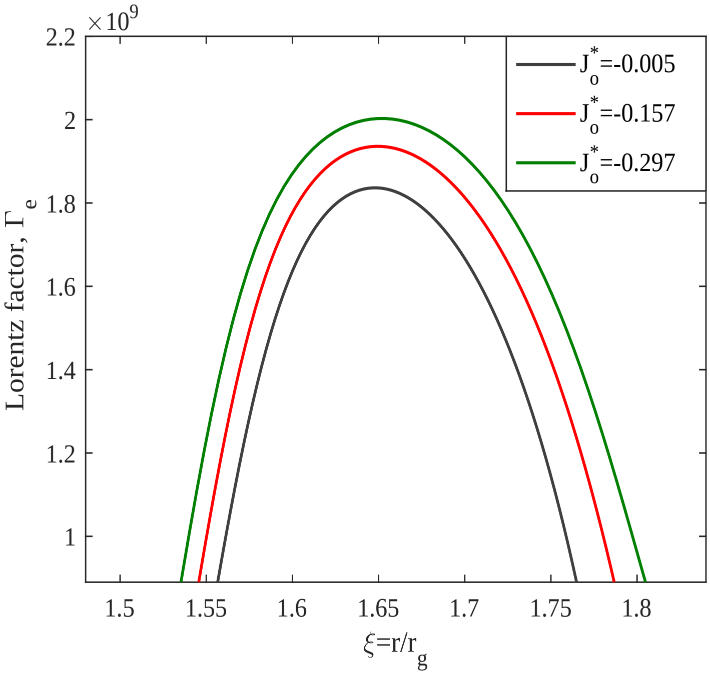

Figure 4.7: The Lorentz factor distribution Γ_e of the particles given for current values $J_o^* = -0.005$ (black line), $J_o^* = -0.157$ (red line) and $J_o^* = -0.297$ (green line). The parameters used are: $M_9 = 1.0$, $\alpha_s^* = 1.0$, $\dot{m} = 10^{-5.0}$ and $\theta = 30^o$.

mum of the electric field. Evidently, neither a dramatic change in the voltage drop[21] (e.g., see table 4.1) nor in the *Lorentz* factor is observed for those current variations. It is seen, finally, in table (4.1) that the gap luminosity (see equation 3.35) constitutes only a small fraction of the *Blandford-Znajek* power.

We were not able to find any steady solution for $\dot{m} > 10^{-4.5}$, and thus considered here the case where the black hole is fed by accretion at a rate, $\dot{m} = 10^{-5.0}$. That fact, which seems to match the case of the radio galaxy M87 (Akiyama et al., 2019b), might have a possible physical interpretation. A greater accretion rate would inevitably lead to gap breakdown due to the efficient pair cascade that would happen in the magnetosphere. Hence, one can say that steady gaps are not allowed for high enough accretion rates.

As we have already mentioned, the choice of a low accretion rate ($\dot{m} = 10^{-5}$) affects the spectrum of the ADAF. According to the analysis in chapter (2), we find that the *synchrotron* component peaks approximately at an energy $E_{syn}^{peak} \approx 3 \times 10^{-4}$ eV, the spectral index of the *Compton* part is $\alpha_c \approx 2.25$, the corresponding temperature of the electrons in the disk reaches $T_e \approx 8.6 \times 10^9$ K and, finally, the *synchrotron* peak luminosity becomes $l_{syn}^{peak} = 2.9 \times 10^{37}\ erg/sec^{-1}$ (see figure 2.6).

We can now compare VHE observations with the estimates of table (4.1). If we associate, for example, the gap power with the TeV luminosity of the flaring events from M87 (i.e., $l_{TeV}/l_{BZ} \sim 5 \times 10^{-3}$), the global current will take a value larger than $|J_o^*| > 0.3$. Therefore, the steady gap model can be related to the VHE activity of M87, providing also a plausible current value. As already discussed, the global magnetospheric current is a critical function which is associated with the demonstration of the black hole magnetosphere and the jet formation.

The total charge density with respect to the *Goldreich-Julian* one, as well as, the positron and electron charge densities as distributed within the gap region are illustrated in the left and right column of figure (4.8), respectively. Each row in that figure corresponds to different value of the global magnetospheric current. Given that we required our solutions to cross the *null* point, one can see in all the sub-plots (e.g., left column) that the resulting charge density remains always lower than the critical limit which is defined by the *Goldreich-Julian* charge distribution, that is $|\rho_e| \leq |\rho_{GJ}|$. Furthermore, the relaxation of conditions (4.65) and (4.66) in this project has led to gap solutions with injection of both species at the boundaries (with the exception of the outer boundary for current $J_o^* = -0.005$; see left column in figure 4.8).

---

[21] The voltage drop resulting from the gap accelerator is estimated by the following equation: $\Delta V_{gap} = -\int_{\xi_1}^{\xi_2} r_g\, \mathcal{E}_{||}^{\hat{r}}\, d\xi$.

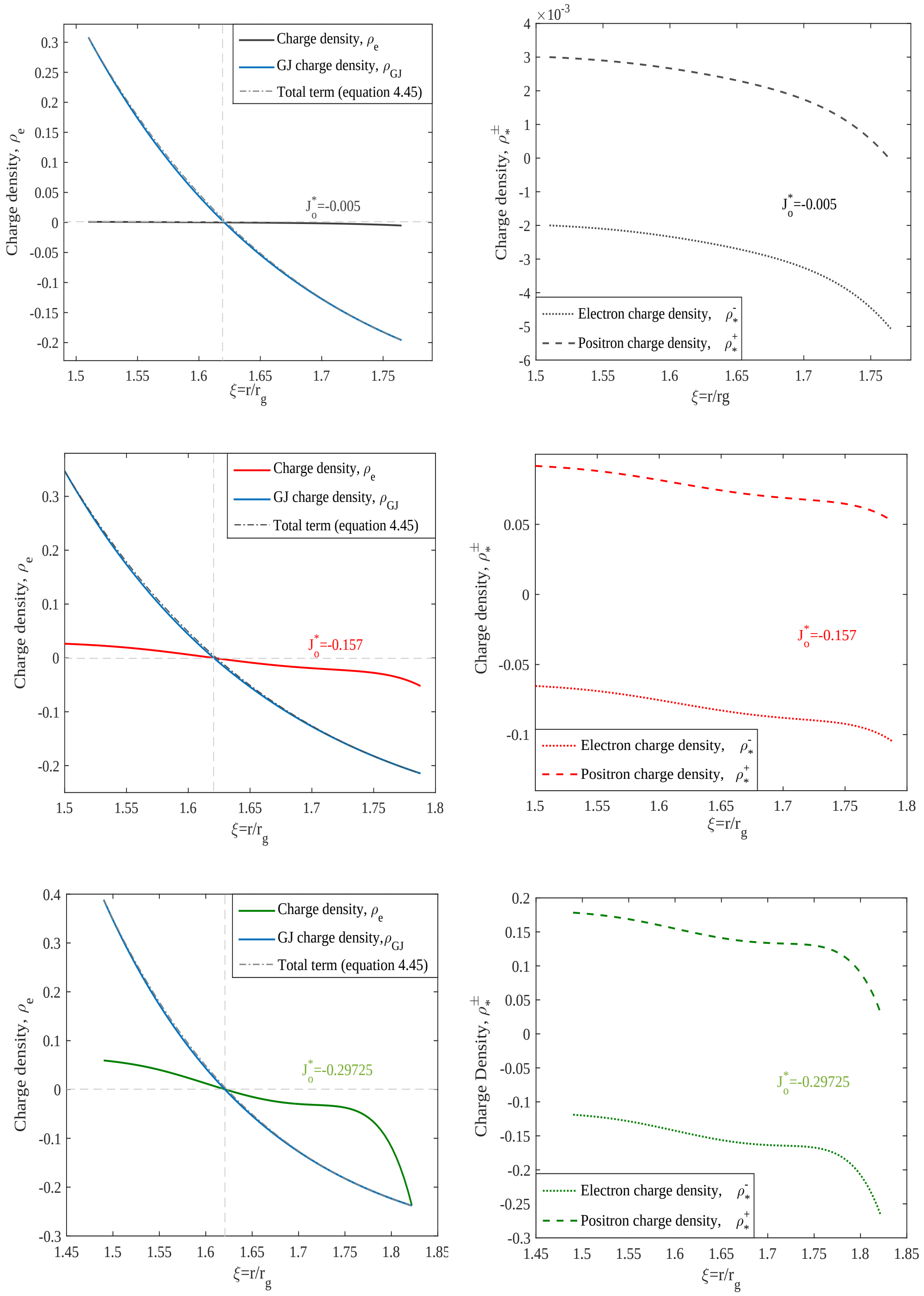

Figure 4.8: Graphical representation of the resulting charge densities with respect to the *Goldreich-Julian* one (left column) and the positron/electron charge densities as distributed within the gap region (right column) shown for current value $J_o^* = -0.005$ (black line), $J_o^* = -0.157$ (red line) and $J_o^* = -0.297$ (green line), respectively. The parameters used are: $M_9 = 1.0$, $\alpha_s^* = 1.0$, $\dot{m} = 10^{-5.0}$ and $\theta = 30^o$.

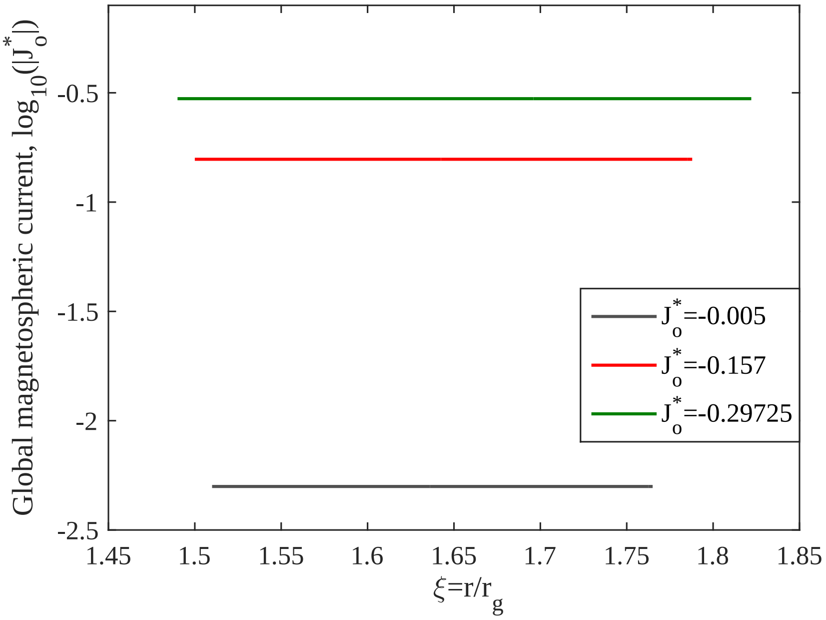

Figure 4.9: Graphical illustration of the global magnetospheric current shown for current value $J_o^* = -0.005$ (black line), $J_o^* = -0.157$ (red line) and $J_o^* = -0.297$ (green line), respectively. The parameters we use are: $M_9 = 1.0$, $\alpha_s^* = 1.0$, $\dot{m} = 10^{-5.0}$ and $\theta = 30^o$.

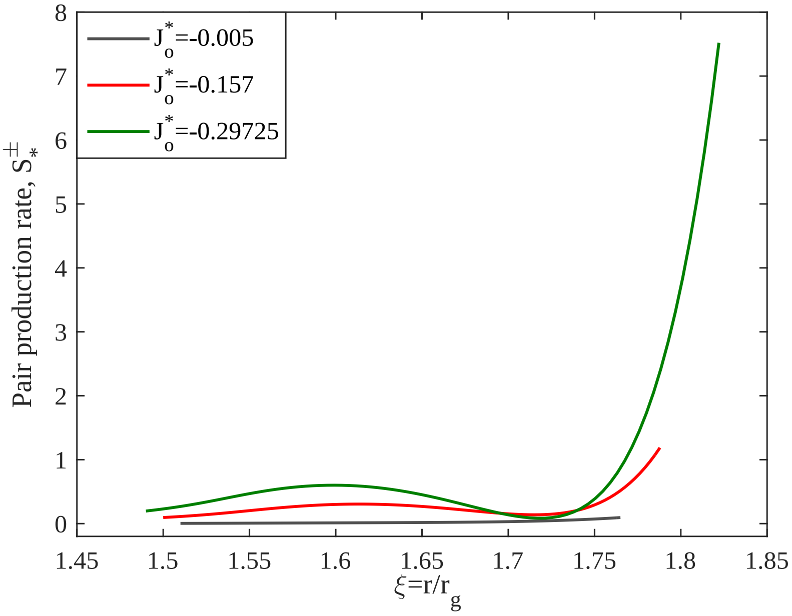

Figure 4.10: Graphical representation of the pair production rate (equation 4.57) given for current value $J_o^* = -0.005$ (black line), $J_o^* = -0.157$ (red line) and $J_o^* = -0.297$ (green line), respectively. The parameters we use are: $M_9 = 1.0$, $\alpha_s^* = 1.0$, $\dot{m} = 10^{-5.0}$ and $\theta = 30^o$.

It is also worth commenting that the choice of small current value[22] (i.e., $J_o^* = -0.005$) leads to a highly under-dense gap, while a higher current (i.e., $J_o^* = -0.29725$) provides a charge distribution that matches the *Goldreich-Julian* charge density at the outer boundary.

In figures (4.9) and (4.10), the radial distribution of the global magnetospheric current and the pair production rate (see equations 4.28 and 4.57) are depicted. According to our expectations (see equations 4.51 and 4.52), the current is indeed constant along the field lines. The high energy γ-ray photons, on the other hand, present a complex behaviour. As it is seen from equation (4.57), the source term is formed by the summation of outcoming and incoming photons in each energy bin. It turns out, however, that there are some bins which contribute decisively to the gap structure and many others which do not[23]. In the numerical procedure, it can happen that this last class of energy bins can even take negative values in some cases. As it turns out (private discussion with *A. Levinson*), this seems to be a generic (and possibly structural) problem of the steady gap model. We do emphasize, nevertheless, that we can safely trust our solutions, since lower value (or negative) energy bins only make a negligible contribution to the gap realization. From figure (4.10), we finally obtain that the pair production rate becomes higher under the enhancement of the global current.

4.5.2 Gap solutions: Fixed global current

In the previous subsection, we explored gap solutions for different choices of the global magnetospheric current. In this series of runs, we keep the global current constant seeking to investigate structural variations of the gap due to changes in the accretion rate.

In figure (4.11), we illustrate the distribution of the parallel electric field component (upper-left diagram), the *Lorentz* factor of the injected pairs (upper-right diagram), the total charge density in association with the *Goldreich-Julian* one (lower-left diagram), as well as, the positron and electron charge densities within the gap (lower-right diagram). In particular, we provide gap solutions which correspond to three different values of the accretion rate, namely $\dot{m} = 10^{-5.0}$, $\dot{m} = 10^{-6.0}$ and $\dot{m} = 10^{-6.5}$ depicted with black, red and green color, respectively. We note that the solutions below again represent gap regions embedded in the magnetosphere (with current value $J_o^* = -0.157$) of a fast rotating ($\alpha_s^* = 1.0$) supermassive ($M = 10^9 M_\odot$) black hole.

---

[22] In absolute values.

[23] This happens, of course, due to the energy and the number of the soft photons.

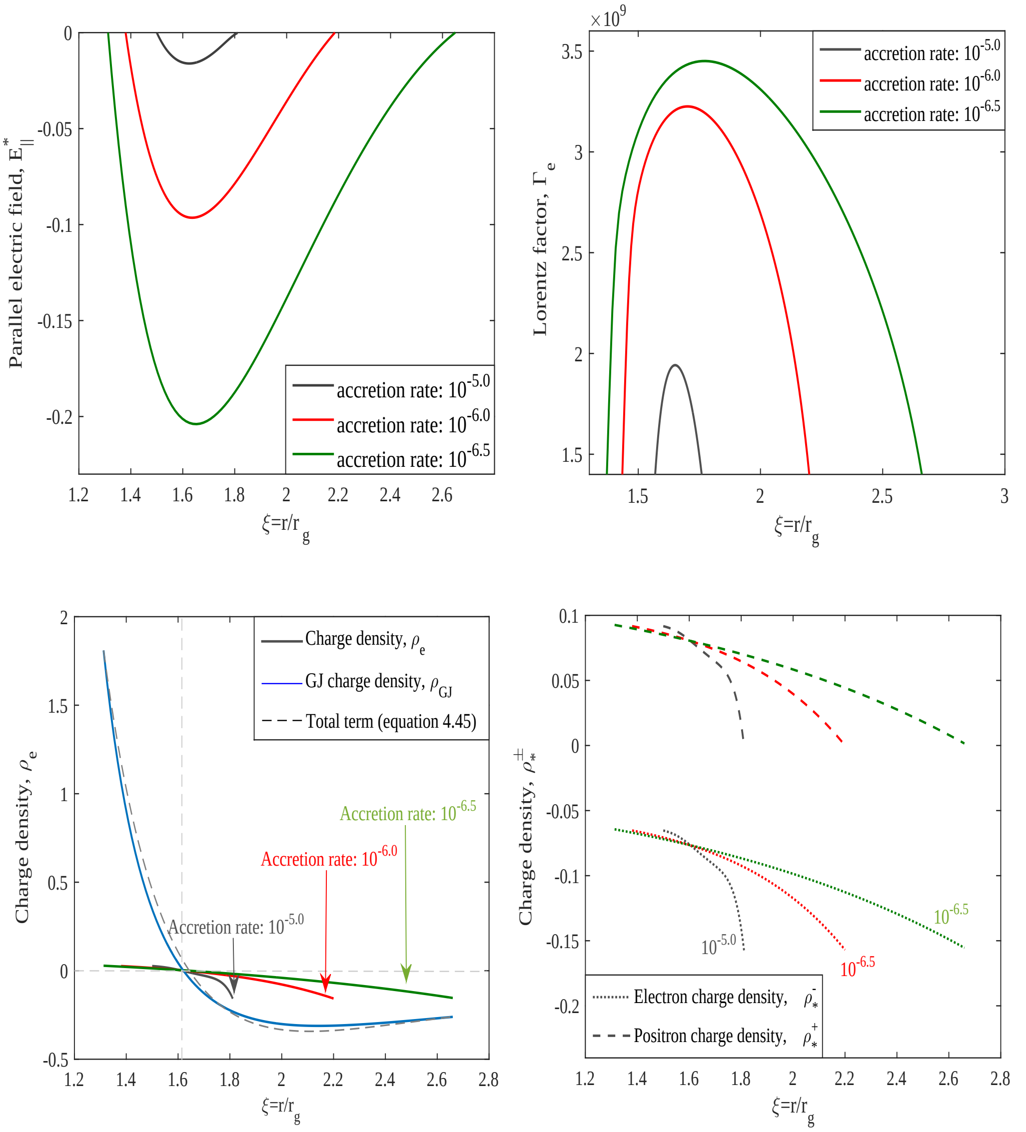

Figure 4.11: Graphical depiction of the parallel electric field component $\mathcal{E}^{*r}_{||}$ (upper-left diagram), the *Lorentz* factor of the injected pairs Γ_e (upper-right diagram), the total charge density ρ_e in association with the *Goldreich-Julian* one (lower-left diagram) and the positron/electron charge densities $\rho^{\pm}_{*}$ (lower-right diagram) for accretion rate $\dot{m} = 10^{-5.0}$ (black line), $\dot{m} = 10^{-6.0}$ (red line) and $\dot{m} = 10^{-6.5}$ (green line), respectively. The remaining parameters used are: $M_9 = 1.0$, $\alpha^*_s = 1.0$, $J^*_o = -0.157$ and $\theta = 30^o$.

As can be seen in figure (4.11), the gap range increases as the accretion accretion rate decreases (see the upper-left chart). This finding seems reasonable given that for lower soft photon field, the pair production efficiency is reduced such that larger gaps are expected. The gap size is roughly comparable to the gravitational radius for the lower accretion rates that have been implemented in these runs of the code (see table 4.2 for details). We

Table 4.2: Estimate of the gap extension, the voltage difference through the accelerator, the *Blandford-Znajek* power (see equation 3.14) and the gap luminosity (see equation 3.34) resulting from the (1D) steady gap solutions described in the text. The parameters used are: $M_9 = 1.0$, $\alpha_s^* = 1.0$, $J_o^* = -0.157$ and $\theta = 30^o$.

Accretion Rate	*Gap Size*	*Voltage Drop*	*BZ power*	*Gap Power*
$\dot{m} = \dot{M}/\dot{M}_{Edd}$	(h/r_g)	$\times 10^{16}$ Volts	$\times 10^{43}\ erg\,sec^{-1}$	$\times 10^{40}\ erg\,sec^{-1}$
$10^{-5.0}$	0.2879	2.1	2.0	2.50
$10^{-6.0}$	0.82	10.3	0.2	3.82
$10^{-6.5}$	1.3475	18.7	0.06	3.89

also note that the parallel electric field reaches its minimum value at the *null point*. In addition, we find in figure (4.11) that the maximum *Lorentz* factors ($\Gamma_e \sim 2.0 - 3.5 \times 10^9$) are achieved beyond the extremum of the electric field (see the upper-right chart). Evidently, the lower the accretion rate is, the higher the particle's acceleration is obtained. However, the *Lorentz* factor changes only slightly (always remaining of the order of, $\Gamma_e \sim 10^9$) provided that the voltage drop along the gap increases about 10 to 20 times under variations in the accretion rate (see table 4.2). The resulting total charge density for all the solutions satisfy the condition, $|\rho_e| \leq |\rho_{GJ}|$ everywhere (see the lower-left chart). It is, finally, seen in figure (4.11) that charge injection of both species (i.e, relaxation of condition 4.65 and 4.66) has taken place mostly at the inner boundary (see the lower-right chart).

Table 4.3: Estimate of the peak energy of the *synchrotron* component, the temperature of the electrons in the accretion disk, the spectral index of the *Compton* branch and the *synchrotron* peak luminosity normalized in *Eddington units* (see equation 3.3) for different values of accretion rate as described in the text. The parameters used are: $M_9 = 1.0$, $\alpha_s^* = 1.0$.

Accretion Rate	*Synchrotron Peak Energy*	*Disk Temperature*	*Compton Index*	*Synchrotron Peak Power*
$\dot{m} = \dot{M}/\dot{M}_{Edd}$	(10^{-4} eV)	(10^9 K)	α_c	l_{disk}/l_{Edd}
$10^{-5.0}$	2.93	8.6	2.25	2.23×10^{-10}
$10^{-6.0}$	0.95	11.6	2.50	1.01×10^{-11}
$10^{-6.5}$	0.53	13.4	2.61	2.1×10^{-12}

The attainable gap luminosities are calculated in table (4.2). Accordingly, only a fraction of the *Blandford-Znajek* power can be released by the gap accelerator. In the special case of M87, for example, accretion rate $\sim 10^{-5.0}$ seems to be required. It is worth noting that this value is compatible with recent observational estimates for M87 (Akiyama et al., 2019b).

In table (4.3) above, we summarize the physical characteristics of the soft photon emission (i.e., the ADAF spectrum) inferred for the three different values of the accretion rate. More specifically, we present the peak energy of the *synchrotron* component, $E_{syn}^{peak} \approx (0.53-2.93)\times 10^{-4}$ eV, the temperature of the electrons in the accretion disk, $T_e \approx (8.6 - 13.4) \times 10^9$ K, the spectral index of the *Compton* branch, $\alpha_c \approx 2.25 - 2.61$, and the *synchrotron* peak luminosity normalized in *Eddington units*, $l_{syn}^{peak}/l_{Edd} \sim (10^{-10} - 10^{-12})$.

4.5.3 Gap solution: Global current of higher value

Table 4.4: Estimate of the gap extension, the voltage difference through the accelerator and the total gap power for the (1D) steady gap solution described in the text. The parameters used are: $M_9 = 1.0$, $\alpha_s^* = 1.0$, $\dot{m} = 10^{-6.0}$, $\theta = 30^o$ and the *Blandford-Znajek* power is given by $l_{BZ} = 2 \times 10^{42}$ $erg\,sec^{-1}$ (see equation 3.14).

Global Current $J_o^* = J_o/c\rho_c$	*Gap Size* (h/r_g)	*Voltage Drop* $\times 10^{16}$ Volts	*Gap Power* $\times 10^{40}$ $erg\,sec^{-1}$
-0.95	0.7225	7.8	2.9

In section (4.3) above, we argued that the existence of steady gap solutions is possible even for high values of the global magnetospheric current if charge injection of both species is allowed at the gap boundaries (i.e., relaxation of conditions 4.65 and 4.66). Hence, it would be interesting to illustrate such a solution for a higher value of the current.

In figure (4.12) below, we depict such a solution, namely the distribution of the parallel electric field component (upper-left diagram), the *Lorentz* factor of the injected pairs (upper-right diagram), the total charge density in association with the *Goldreich-Julian* one (lower-left diagram), as well as, the positron and electron charge densities within the gap (lower-right diagram). In particular, we provide a gap solution where the accretion rate is $\dot{m} = 10^{-6.0}$, while the global magnetospheric current takes on the value of, $J_o^* = -0.95$. As before, we assume that the gap sinks into the magnetosphere of a fast rotating ($\alpha_s^* = 1.0$) supermassive ($M = 10^9 M_\odot$) black hole.

In table (4.4), we present the characteristic gap properties resulting from the actual choice of the current and the accretion rate. Finally, we note that no steady gap solution could be determined for accretion rates lower than $\sim 10^{-6.0}$.

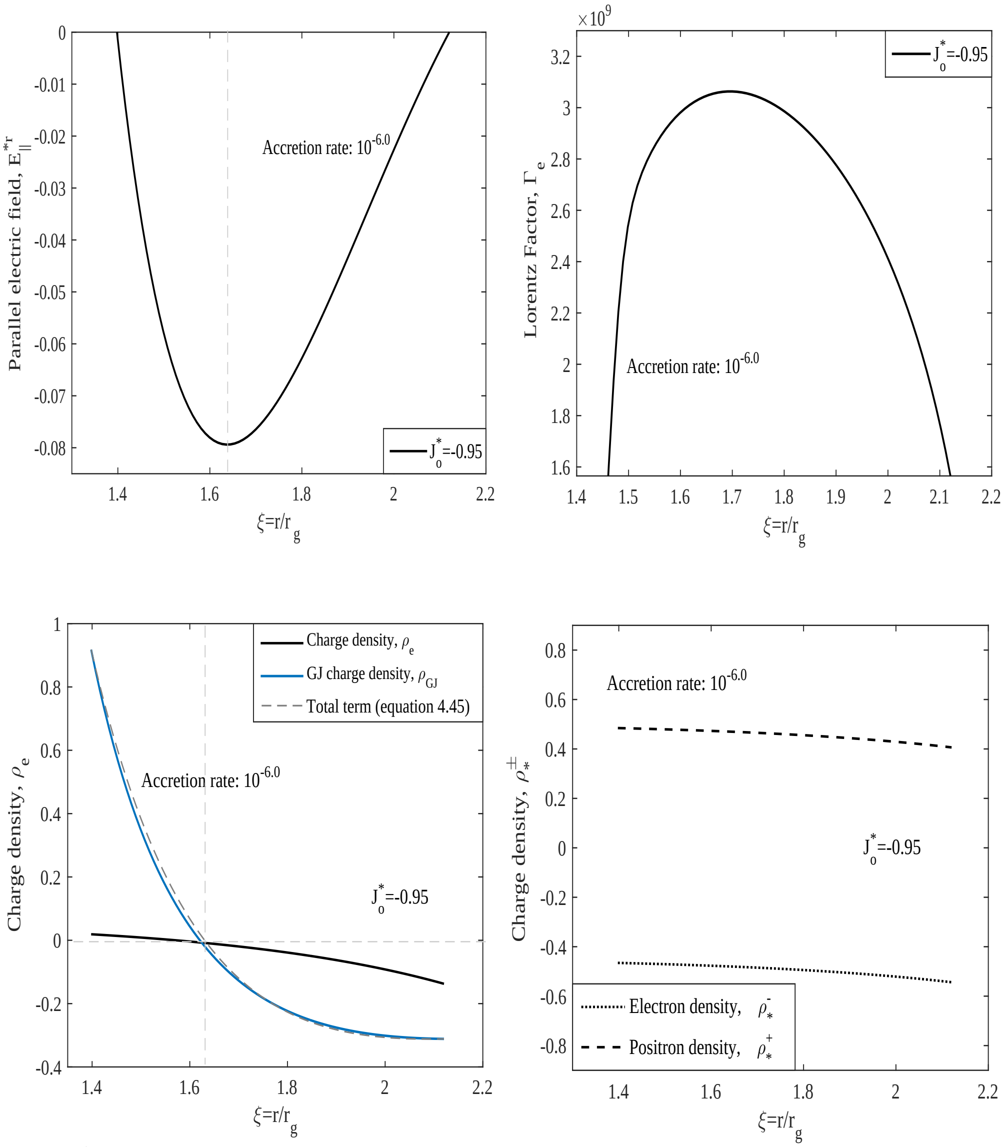

Figure 4.12: Graphical representation of the parallel electric field component $\mathcal{E}^{*r}_{||}$ (upper-left diagram), the *Lorentz* factor of the injected pairs Γ_e (upper-right diagram), the total charge density ρ_e in association with the *Goldreich-Julian* one (lower-left diagram) and the positron/electron charge densities $\rho^{\pm}_*$ (lower-right diagram) for a global magnetospheric current $J^*_o = -0.95$ and accretion rate $\dot{m} = 10^{-6.0}$. The parameters used are: $M_9 = 1.0$, $\alpha^*_s = 1.0$ and $\theta = 30^o$.

4.6 ***Particle-In-Cell*** simulations

In the previous sections, we described the physics of the (1D) steady gap model and presented proper solutions of its structure. Furthermore, we have

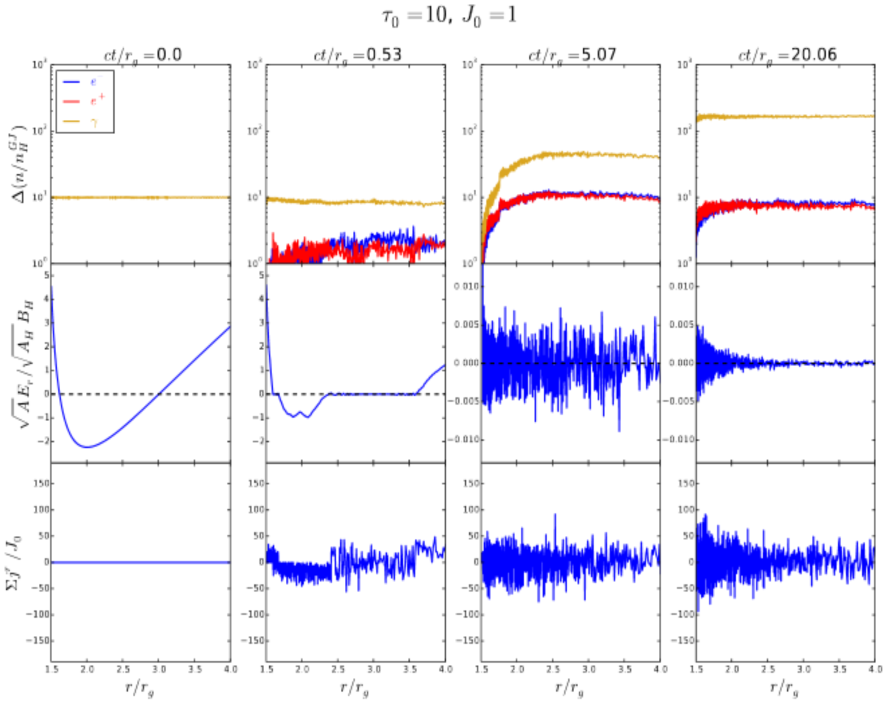

Figure 4.13: The time evolution of the gap region as found by A. Levinson and B. Cerutti. For more details of the simulation setup see (Levinson and Cerutti, 2018).

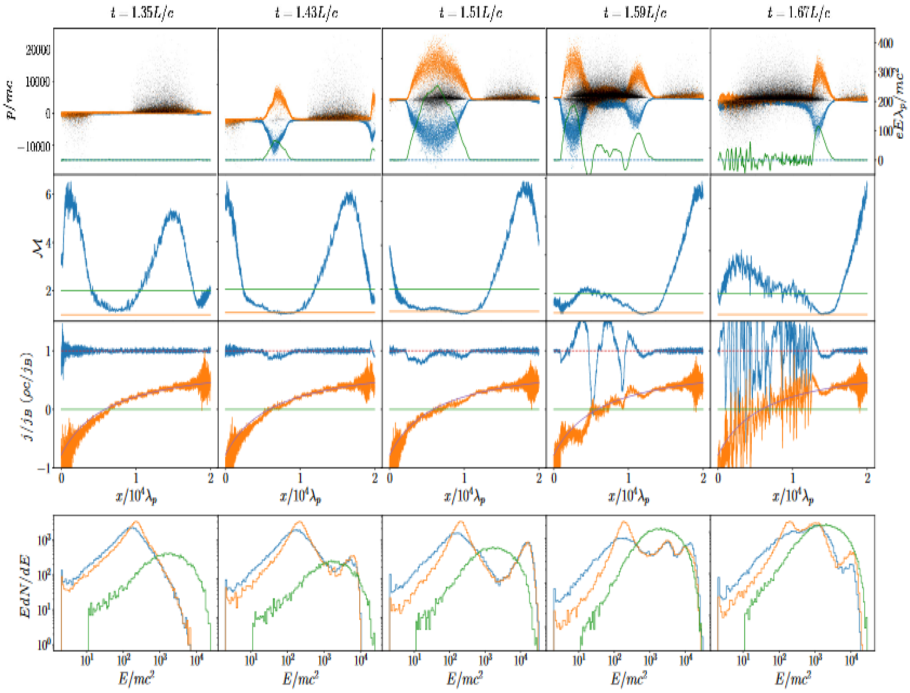

Figure 4.14: The time evolution of the gap region as found by A. Chen and his collaborators. For more details of the simulation setup see (Chen et al., 2018).

discussed its applicability to the understanding of the very high energy γ-ray observations. Basically, we estimated that the VHE observations from the radio galaxy M87 can match to the model predictions. Although, the stationary approach reveals in principle the physical content of the processes in the gap region, we can plausibly assume that the black hole magnetosphere is a rather dynamical and variable environment. Hence, the study of the time-dependent problem could allow for progress in understanding the magnetospheric processes. The oscillating gap model is, nevertheless, outside the scopes of the current project. In this section, we give a short overview of time-varying gaps just for sake of completeness and covering the relative literature.

The (1D) *Particle-in-cell* or shortly (PIC) simulations constitute the state of the art tool for the investigation of oscillating magnetospheric gap zones. In figures (4.13) and (4.14) above, we present results from two gap simulations with rather conflicting predictions (Levinson and Cerutti, 2018; Chen et al., 2018). More specifically, *Levinson* and *Cerutti* constructed a *general* relativistic PIC code that computes the γ-ray emission and the pair production, which result from the interaction of pairs and γ-rays with a fiducial soft photon field. According to figure (4.13), they found an initial discharge of the gap region that produces a high energy γ-ray flare with duration of about $\Delta t \sim r_g/c$. Subsequently, the initial situation is followed by rapid, small amplitude oscillations that last for the the entire simulation time during which the pair plasma is continuously replenished through self-sustained pair cascades, leading to quasi-stationary pair and γ-ray spectra. The γ-ray spectrum produced from the gap region peaks in the TeV band, while the total gap luminosity constitutes only a small fraction of the corresponding *Blandford-Znajek* power (i.e, $l_{gap}/l_{BZ} \sim 10^{-5.0}$). *Chen* and his collaborators, on the other hand, found a highly time-dependent solution in their (1D) special relativistic simulations, where a macroscopic gap (of the order of r_g) is triggered quasi-periodically producing leptons and high energy radiation (see figure 4.14).

It has to be mentioned, of course, that it is of relevance to examine in detail the used parameters among the different setups. Obviously, the soft photons in the first setup is somewhat artificial, while in the second setup a high minimum soft photon energy ($E_{min} \sim 0.5$ eV) is assumed resulting in moderate pair creation. From the discussion above, it is clear that the time-dependent magnetospheric gap is not yet fully understood.

4.7 Concluding remarks

In this chapter, a detailed analysis of the (1D) steady gap accelerator formed across the null surface of a rapidly rotating black hole magnetosphere has been presented. In our approach, we took into account the general relativistic expression of *Gauss's* law and assumed that the gap is embedded within the radiation field emitted by an ADAF. In particular, we derive expressions for the radial distribution of the parallel electric field component, the Lorentz factor of the created pairs, the charge density for both species (i.e., electrons and positrons) and the number density of the γ-ray photons. We integrated the set of equations numerically imposing relevant boundary conditions (e.g., $\mathcal{E}_{||}^{r} = 0$, $\Gamma_e = 1.0$ at the gap boundaries) and demanding the resulting amount of charges to be less than the *Goldreich-Julian* charge density along the gap extension (i.e., $|\rho_e| \leq |\rho_{GJ}|$). The existence of steady gap solution for high value of the global current is possible if charge injection of both species is allowed at the boundaries. Using the so-called shooting method for the numerical integration of the equations we obtained gap solutions for different choices of the global current and the accretion rate. Our solutions suggests that the variable VHE emission in M87 could be attributed to magnetospheric gaps.

Bibliography

F. M. Rieger and G. Katsoulakos, 7^{th} Fermi Symposium PoS, 2017
G. Katsoulakos anf F.M. Rieger, ApJ, 852:112, 2018

Bibliography

A. A. Abdo, M. Ackermann, M. Ajello, et al. *ApJ*, 707:55, 2009.

MA. Abramowitz, B. Czerny, JP. Lasota, and E. Szuszkiewicz. *ApJ*, 332:646, 1988.

A. Abramowski, F. Acero, F. Aharonian, et al. *ApJ*, 746:151, 2012.

V. A. Acciari, E. Aliu, T. Arlen, et al. *Science*, 325:444, 2009.

F. Acero, M. Ackermann, M. Ajello, et al. *ApJS*, 218:23, 2015.

F. A. Aharonian and A. M. Atoyan. *Ap&SS*, 79:321, 1981.

F. A. Aharonian, A. Akhperjanian, M. Beilicke, et al. *A&A*, L1:403, 2003.

F. A. Aharonian, A. Akhperjanian, A. R. Bazer-Bachi, et al. *Science*, 314: 1424, 2006.

F. A. Aharonian, M. V. Barkov, and D. Khangulyan. *ApJ*, 841:61, 2017.

M. L. Ahnen, S. Ansoldi, L. A. Antonelli, et al. *A&A*, A25:603, 2017.

K. Akiyama, R.-S. Lu, V.L. Fish, et al. *ApJ*, 807:150, 2015.

K. Akiyama, K. Kuramochi, S. Ikeda, et al. *ApJ*, 831:1, 2017.

K. Akiyama, A. Alberdi, W. Alef, et al. *ApJL*, L1:875, 2019a.

K. Akiyama, A. Alberdi, W. Alef, et al. *ApJL*, L5:875, 2019b.

I. Albert, E. Alin, H. Anderhub, et al. *ApJL*, L23:685, 2008.

J. Aleksić, L.A. Antonelli, P. Antoranz, et al. *ApJ*, L207:723, 2010.

J. Aleksic, S. Ansoldi, L. A. Antonelli, et al. *Science*, 346:1080, 2014a.

J. Aleksic, L. A. Antonelli, P. Antoranz, et al. *A&A*, A91:563, 2014b.

E. Aliu, T. Arlen, T. Aune, et al. *ApJ*, 746:141, 2012.

A. De. Angelis and M. Mallamaci. *Eur. Phys. J. Plus*, 133:324, 2018.

S. Ansoldi, L. A. Antonelli, C. Arcado, et al. *A&A*, A91:617, 2018.

M. V. Barkov, F. A. Aharonian, and V. Bosch-Ramon. *ApJ*, 724:1517, 2010.

M. V. Barkov, F. A. Aharonian, S. V. Bogovalov, S. R. Kelner, and Khangulyan. *ApJ*, 749:119, 2012.

T. Beckert and W. J. Duschl. *A&A*, 387:422, 2002.

M. C. Begelman. *MNRAS*, 187:237, 1979.

M. Beilicke and VERITAS Collaboration. *In AIP Conf. Ser. 1505, High-Energy Gamma-Ray Astronomy: 5th International Meeting on High Energy Gamma-Ray Astronomy.* ed. F.A. Aharonian, W. Hofmann & F.M. Rieger (Melville, NY:AIP),586, 2012.

F. Ait Benkhali, N. Chakraborty, and F.M. Rieger. *A&A*, A2:623, 2019.

V. B. Berestetskii, E. M. Lifshitz, and L. P. Pitaevskii. *Quantum Electrodynamics.* 3d ed., Japanese trans., Tokyo: Marruzen, 1989.

M. Berton, L. Foschim, S. Ciroi, et al. *A&A*, A28:578, 2015.

V. S. Beskin. *MHD Flows in Compact Astrophysical objects: Accretion, Winds, and Jets.* Berlin, Springer, 2009.

V. S. Beskin. *MHD Flows in Compact Astrophysical Objects.* Springer, 2010.

V. S. Beskin, Y. N. Istomin, and V. I. Parev. *SvA*, 36:642, 1992.

S. Bird, W.E. Harris, J.P. Blakeslee, and C. Flynn. *A&A*, A71:524, 2010.

R. G. Blandford and R. L. Znajek. *MNRAS*, 179:433, 1977.

V. Bosch-Ramon, M. Perucho, and M. V. Barkov. *A&A*, A69:539, 2012.

A. E. Broderick and A. Tchekhovskoy. *ApJ*, 809:97, 2015.

A. Y. Chen, Y. Yuan, and H. Yang. *ApJL*, L31:863, 2018.

I. Contopoulos, D. Kazanas, and C. Fendt. *ApJ*, 511:358, 1999.

S.S. Doeleman, Y. L. Fish, D.E. Schenck, et al. *Science*, 338:355, 2012.

A. A. Esin, J. E. McClintock, and R. Narayan. *ApJ*, 489:865, 1997.

C. Fendt. *A&A*, 319:1025, 1997.

C. Fendt and E. Memola. *A&A*, 365:631, 2001.

J. Feng and Q. Wu. *MNRAS*, 470:612, 2017.

J. Frank, A. King, and D. Raine. *Accretion Power in Astrophysics*. Cambridge: Cambridge University Press, 2002.

M. Georganopoulos, E.S. Perlman, and D. Kazanas. *ApJ*, L33:634, 2005.

G. Ghisellini, F. Tavecchio, and M. Chiaberge. *A&A*, 432:401, 2005.

G. Ghisellini, F. Tavecchio, L. Maraschi, A. Celotti, and T. Sbarrato. *Nature*, 515:376, 2014.

D. Giannios. *MNRAS*, 431:355, 2013.

D. Giannios, D.A. Uzdensky, and M.C. Begelman. *MNRAS*, L29:395, 2009.

D. Giannios, D.A. Uzdensky, and M.C. Begelman. *MNRAS*, 402:1649, 2010.

N. Globus and A. Levinson. *ApJ*, 796:26, 2014.

P. Goldreich and W. H. Julian. *ApJ.*, 157:869, 1969.

K. Hada, M. Kino, H. Nagai, et al. *ApJ*, 760:52, 2012.

K. Hada, M. Giroletti, M. Kino, et al. *ApJ*, 788:165, 2014.

K. Hada, M. Kino, A. Doi, et al. *ApJ*, 817:131, 2016.

J. F. Hawley, C. Fendt, M. Hardcastle, et al. *Space Sci Rev*, 191:441, 2015.

K. Hirotani. *MDPI*, 6:122, 2018.

K. Hirotani and I. Okamoto. *ApJ*, 497:563, 1998.

K. Hirotani and H.-Y. Pu. *ApJ*, 818:50, 2016.

K. Hirotani and S. Shibata. *MNRAS*, 308:67, 1999.

K. Hirotani, H.-Y. Pu, L. C.-C. Lin, et al. *ApJ*, 833:142, 2016.

K. Hirotani, H.-Y. Pu, L. C.-C. Lin, et al. *ApJ*, 845:77, 2017.

S. Ichimaru. *ApJ*, 214:840, 1977.

M. Kadler, E. Ros D. Eisenacher, et al. *A&A*, L1:538, 2012.

G. Katsoulakos and F. M. Rieger. *ApJ*, 852:112, 2018.

J. Katz. *ApJ*, 215:265, 1977.

A. R. King, J. E. Pringle, and M. Livio. *MNRAS*, 376:1740, 2007.

M. Kino, F. Takahara, K. Hada, et al. *ApJ*, 803:30, 2015.

S.S. Komissarov. *MNRAS*, 350:427, 2004.

A. Levinson. *PhRvL*, 85:912, 2000.

A. Levinson and B. Cerutti. *A&A*, A184:616, 2018.

A. Levinson and F. M. Rieger. *ApJ*, 730:123, 2011.

A. Levinson and N. Segev. *PhRvD*, 96:123006, 2017.

M. Livio, G. L. Ogilvie, and J. E. Pringle. *ApJ*, 512:100, 1999.

D. Lynden-Bell and JE. Pringle. *MNRAS*, 168:603, 1974.

D. Macdonald and K.S. Thorne. *MNRAS*, 198:345, 1982.

R. Mahadevan. *ApJ*, 477:585, 1997.

T. Manmoto, S. Mineshige, and M. Kusunose. *ApJ*, 489:791, 1997.

T. Di Matteo, S. W. Allen, A. C. Fabian, A.S. Wilson, and A.J. Young. *ApJ*, 582:133, 2003.

S. Mei, J.P. Blakeslee, P. Cote, et al. *ApJ*, 655:144, 2007.

D. L. Meier. *ApJL*, 548:L9, 2001.

F. Mertens, A. P. Lobanov, R. C. Walker, and P.E. Hardee. *A&A*, 54:595, 2016.

K. Nalewajko, D. Giannios, M.C. Begelman, et al. *MNRAS*, L33:754, 2011.

R. Narayan and I. Yi. *ApJL*, L13:428, 1994.

R. Narayan and I. Yi. *ApJ*, 452:710, 1995a.

R. Narayan and I. Yi. *ApJ*, 444:231, 1995b.

R. Narayan and I. Yi. *ApJ*, 452:710, 1995c.

R. Narayan, R. Mahadevan, and E. Quataert. *In The Theory of Black Hole Accretion Disks.* ed. M. A. Abramowicz et al., Cambridge University Press, 1998.

A. Nathanail and I. Contopoulos. *ApJ*, 788:186, 2014.

R. S. Nemmen, T. Storchi-Bergmann, and M. Eracleous. *MNRAS*, 438:2804, 2014.

A. Neronov and F. A. Aharonian. *ApJ*, 671:85, 2007.

I. D. Novikov and K. S. Thorne. *Black holes (Les astres occlus).* Edited by C. DeWitt and B. DeWitt, Gordon and Breach, N.Y., 1973.

Z. Osmanov, S. Mahajan, and G. Machabeli. *ApJ*, 835:164, 2017.

F. N. Owen, J. A. Eilek, and N. E. Kassim. *ApJ*, 543:611, 2000.

W. H. Press, S. A. Teukolsky, W. T. Vetterling, and B. P. Flannery. *Numerical recipes; The art of scientific computing.* Cambridge University Press, 2007.

M. A. Prieto, J. A. Fernandez-Ontiveros, S. Markoff, D. Espada, and O. Gonzalez-Martin. *MNRAS*, 457:3801, 2016.

K. Ptitsyna and A. Neronov. *A&A*, A8:593, 2016.

MJ. Rees, MC. Begelman, RD. Blandford, and ES. Phinney. *Nature*, 295:17, 1982.

C. S. Reynolds, T. Di Matteo, A. C. Fabian, U. Hwang, and C.R. Canizares. *MNRAS*, L111:283, 1996.

F. Rieger and F. A. Aharonian. *A&A*, L5:497, 2008.

F. M. Rieger. *IJMPD*, 20:1547, 2011.

F. M. Rieger and F. A. Aharonian. *Mod. Phys. L.*, A27:1230030, 2012.

F. M. Rieger and G. Katsoulakos. *PoS*, 7^{th} Fermi Symposium, 2017.

F. M. Rieger and A. Levinson. *Galaxies*, 6(4):116, 2018.

G. B. Rybicki and A.P. Lightmann. *Radiative Processes in Astrophysics.* Wiley, 1979.

G. Di Sciascio. *J. Phys. Conf. Ser.*, 1263:012003, 2019.

NI. Shakura and RA. Sunyaev. *A&A*, 24:337, 1973.

SL. Shapiro, AP. Lightman, and DM. Eardley. *ApJ*, 204:287, 1976.

D. Sijbring and A. G. de Bruyn. *A&A*, 331:901, 1998.

L. Sironi, M. Petropoulou, and D. Giannios. *MNRAS*, 450:183, 2015.

L. S. Sparke and J. S. Gallagher. *Galaxies in the Universe.* Second Edition, Cambridge University Press, 2007.

M. Takahashi, S. Nitta, Y. Tatematsu, and A. Tomimatsu. *ApJ*, 363:206, 1990.

F. Tavecchio and G. Ghisellini. *MNRAS*, L98:385, 2008.

F. Tavecchio and G. Ghisellini. *MNRAS*, 443:1224, 2014.

A. Tchekhovskoy and J. C. McKinney. *MNRAS*, L55:423, 2012.

A. Tchekhovskoy, R. Narayan, and J. C. McKinney. *MNRAS*, L79:418, 2011.

K. S. Thorne and D. A. Macdonald. *MNRAS*, 198:339, 1982.

K. S. Thorne, R. H. Price, and D. A. Macdonald. *Black holes, The membrane paradigm.* Yale University Press, 1986.

C. M. Urry and P. Padovani. *Publications of the Astronomical Society of the Pacific*, 107:803, 1995.

D. A. Uzdensky. *ApJ*, 603:652, 2004.

D. A. Uzdensky. *ApJ*, 620:889, 2005.

S. Vincent. *JCAP*, 05:042, 2015.

R. M. Wald. *PhRvD*, 10:1680, 1974.

D. Whysong and R. Antonucci. *ApJ*, 602:116, 2004.

I. Yi. *in ASP Conf. Ser. 160, Astrophysical Discs.* ed. J.A. Sellwood & J. Goodman (San Francisco, CA: ASP),279, 1999.

F. Yuan and R. Narayan. *Annu. Rev. Astron. Astrophys.*, 52:529, 2014.

L. Zhang and K. S. Cheng. *ApJ*, 475:534, 1997.